Technische Universtät München
Lehrstuhl für Leichtbau

Multidisciplinary design optimization of an ion source for fusion reactors

Riccardo Nocentini

Vollständiger Abdruck der von der Fakultät für Maschinenwesen der Technischen Universität München zur Erlangung des akademischen Grades eines

Doktor-Ingenieurs (Dr.-Ing.)

genehmigten Dissertation.

Vorsitzender:

     Univ.-Prof. Rafael Macian-Juan

Prüfer der Dissertation:

     1. Univ.-Prof. Dr.-Ing. Horst Baier

     2. Hon.-Prof. Dr.-Ing., Dr. Eng. (Univ. Nagoya/Japan) Hans-Harald Bolt

Die Dissertation wurde am 08.03.2011 bei der Technischen Universität München eingereicht und durch die Fakultät für Maschinenwesen am 16.09.2011 angenommen.

Abstract

English Multidisciplinary design optimization (MDO) is applied to specific topics of the design of the extraction system for ELISE, a new test facility for a large negative ion source. Numerical methods are used to achieve an optimized design of the grids and to assure a reliable operation of the ion source, taking into account several physical and technical aspects.

A magnetic filter field with a strength equivalent to the existing prototype sources must be realized for large sources via an electric current through the plasma grid. The filter field suppresses fast electrons in the areas of negative ion production and reduces co-extracted electrons. For a uniform beam production, a uniform filter field is desirable.

A precise control of cesium deposition and distribution on the plasma grid is essential for the production of negative ions. This is supported by controlling the temperature of the plasma grid in the range of 100 - 200°C. This temperature control is realized by a water circuit under high pressure. The plasma grid design must take into account the high pressure in the water manifold areas in order to reduce stress concentrations.

Co-extracted electrons are unavoidable and cause extremely high localized heat loads on the extraction grid surface, up to 40 MW/m² in local areas of several mm². A dedicated cooling circuit is used to remove the heat and to minimize thermo-mechanical stresses in the grid.

Several models for magnetic fields, electric fields, ion beams, electron trajectories, fluid dynamics, thermal and mechanical stress fields have been applied to achieve the best possible design. The design of the plasma grid is characterized by conflicting requirements. Using the multidisciplinary optimization approach, an automated optimization process has been implemented to further improve the plasma grid design. Limits and advantages of the automated optimization process are discussed with respect to the present case study.

Deutsch Multidisziplinäre Optimierungsmethoden (MDO) werden eingesetzt für die Auslegung des Extraktionssystems von ELISE, eines neuen Teststandes für eine große Negative-Ionen-Quelle. Unter Berücksichtigung verschiedener physi-

kalische und technische Aspekte werden numerische Methoden beispielhaft für das Design des Gittersatzes angewendet.

Ein magnetisches Filterfeld mit ähnlicher Intensität wie bei den aktuellen Prototyp-Quellen muss für eine große Quelle über einen Strom im Plasmagitter realisiert werden, um die Anzahl der schnellen Elektronen im Bereich der Produktion negative Ionen zu reduzieren und den ko-extrahierten Elektronenstrom zu mindern. Für die Erzeugung eines homogenen Ionenstrahls sollte auch das Filterfeld möglichst homogen sein.

Für die Erzeugung von negative Ionen eine genaue Kontrolle der Cäsiumdeposition und -verteilung ist erforderlich. Dies wird durch Kontrolle der Temperatur des Plasmagitters im Bereich von 100 - 200°C unterstützt. Die Temperaturkontrolle erfolgt über einen Wasserkreislauf unter hohem Druck. Die Konstruktion des Plasmagitters muss die hohen Drücke in den Wassersammlern berücksichtigen, um Spannungskonzentrationen zu reduzieren.

Ko-extrahierte Elektronen sind unvermeidbar und verursachen extrem hohe lokale Wärmelasten auf der Oberfläche des Extraktionsgitters, bis zu 40 MW/m^2 im Bereich einiger mm^2. Ein speziell ausgelegter Kühlkreislauf wurde verwendet um die Wärme abzuführen und die thermo-mechanischen Spannungen zu minimieren.

Mehrere Modelle für magnetische Felder, elektrische Felder, Ionentrajektorien, Elektronentrajektorien, Fluiddynamik, Temperatur- und Spannungsfelder wurden verwendet, um das bestmögliche Design zu erreichen. Das Design des Plasmagitters ist geprägt durch gegenläufige Anforderungen. Eine automatische Optimierung mit Hilfe der multidisziplinären Optimierungsmethode wurde eingesetzt. Grenzen und Vorteile des automatisierten Verfahrens werden in Bezug auf den vorliegenden Fall diskutiert.

Contents

Chapter 1

Introduction

1.1   Multidisciplinary design optimization

One of the driving elements of modern society is the continuous search for improved technical solutions. Engineers often employ numerical techniques to assist the evaluation and comparison of new design solutions in search of the best possible option. The search for the best possible solution is called optimization. Multidisciplinary design optimization (MDO) methods have been developed in recent years in order to achieve an optimal design also in the presence of complex problems involving several disciplines.

In this work, numerical and MDO methods are applied to the optimization of the extraction system of a negative-ion source for the NBI system of the nuclear fusion reactor ITER. This ion source is the main component of the test facility ELISE, presently being developed at the Max-Planck-Institut für Plasmaphysik in Garching, Germany.

1.2   Nuclear fusion and neutral beam injection

Nuclear fusion represents an option to cover the rising global energy demand. The fusion process does not produce greenhouse gases nor long-term highly radioactive waste. In addition, fusion power is inherently safe as no chain reaction is involved to sustain the nuclear processes. The concept of a fusion plant is based on the use of the thermal energy released from nuclear fusion of light atomic nuclei to generate steam. This is then used to produce electric energy by means of a steam turbine and an electric generator. The conversion of thermal energy into electric energy is similar to fossil fuel and nuclear fission power plants.

Despite being technically a non-renewable energy source, fusion power would provide a sustainable energy supply. Proposed fusion reactors use deuterium and

tritium, two isotopes of hydrogen, as fuel. Deuterium (D) can be extracted from sea water, where one deuterium atom can be found in every 6300 hydrogen atoms [1]. Tritium (T) can be produced within a fusion reactor via neutron interaction with lithium, which exists in abundant supply in the earth crust or in sea water [2]. Estimated reserves of deuterium and lithium would be enough to cover the global energy needs for 60 million years [3], due to the high energy release in a D–T reaction.

A very high temperature, of the order of 100 million K, is needed for the fusion reaction. At this temperature, the fusion reactants are in a plasma state. The plasma can be confined in toroidal fusion machines by means of a strong magnetic field.

Current experiments rely on several heating methods to reach the operational temperature. One of the main heating systems is the neutral beam injection (NBI), which injects neutral atoms with energies up to 1 MeV into the fusion plasma. As the particles are neutral, they can penetrate the reactor's magnetic field and enter into the plasma chamber undisturbed. The fast atoms are ionized as they collide with the plasma particles and are then trapped inside the reactor by the magnetic field. The resulting fast ions transfer their energy to the plasma particles in repeated collisions, increasing the plasma temperature.

In order to produce a fast neutral beam, several steps are needed. Initially, ions are produced in a plasma source. Subsequently, they are extracted and accelerated by means of a set of grids at different electric potentials and form a fast ion beam. Afterwards, a part of the fast ions is neutralized by letting the beam pass through a gas target. Residual ions are separated from the neutral particles by an electrostatic or a magnetic field and deflected onto an ion dump, while the neutrals are injected into the toroidal plasma.

A fast neutral beam can be generated using positive or negative ions. The neutralization efficiency of positive ions strongly depends on the energy of the particles. The performance of positive ion based systems is acceptable for energies per nucleon[1] lower than 100 keV. The neutralization efficiency of positive ions goes almost to zero for energies higher than 100 keV. On the contrary, negative ions still allow for a neutralization efficiency of 60% at these high energies. However, negative ions are more difficult to produce and require large sources due to a lower extracted current density.

Most of the NBI systems of the current generation of experiments, such as JET [4] in Culham (UK) and ASDEX Upgrade [5] in Garching (Germany), operate using positive ions because high particle energy is not required and they are easier to

---

[1]nucleon: collective name for neutron and proton. NBI can be operated using hydrogen or deuterium isotopes.

produce. However, for the next generation of fusion experiments such as ITER[2] [6] (from Latin: *the way*) a particle energy of 1 MeV is required. Such high energy is necessary to efficiently drive a current and to deposit the beam power into the hot center of the plasma. In addition, it is required to provide a heating power of 16.6 MW per injector, despite the lower current density of negative-ion sources [7].

negative-ion sources and extraction systems have been studied for many years in several countries, mainly in Japan [8] using filament arc sources. Based on that knowledge and experience, a design proposal was developed for the ITER NBI system, partly amended with the later developed SINGAP extraction system [9].

In parallel a radio frequency (RF) driven ion source was developed successfully at the Max-Planck-Institut für Plasmaphysik in Garching for the positive ion NBI system on ASDEX Upgrade. This type of ion source promised significant advantages for ITER (see chapter 3). Its use for negative ions has been studied during the last years by means of three different test facilities at IPP. The RF source is the ITER reference source since 2007, after the ITER requirements were reached in the test facilities at IPP.

However, the size of the present RF sources is only 1/8 of the size of the ITER source. To prove its behavior for significantly larger dimensions a new test facility, ELISE,[3] is under construction at IPP. ELISE will be operated with a "half-size" source, having the same width but only half the height of the ITER source. The experimental results found on ELISE will be implemented in the further design of the ITER NBI system.

1.3   Goal of this work

In this thesis, numerical methods and MDO techniques are applied to the design of the extraction system of ELISE, formed by three grids: plasma grid (PG), extraction grid (EG) and grounded grid (GG). For the extraction system of ELISE, as for the ion source in general, the aim is to fulfill the requirements defined by ITER taking into account the experimental evidence and the technical experience provided by years of operation of prototype sources for NBI at IPP and other institutes.

The goal of this work was to find the best compromise between conflicting design requirements, considering constraints derived from modeling complexity, computational effort, manufacturing and knowledge of plasma physics in negative ions sources. Several models for magnetic fields, electric fields, ion beams, electron trajectories, fluid dynamics, thermal and stress field are required to analyze

---

[2]the international experimental reactor which is presently under construction at Cadarache, France

[3]ELISE: Extraction from a Large Ion Source Experiment

the extraction system of negative-ion sources. Several numerical methods, among which are Finite Element Method (FEM), Computational Fluid Dynamics (CFD) and Multidisciplinary Design Optimization (MDO), have been applied by means of the commercial softwares ANSYS and MATLAB.

Often a single design change affects more than one aspect so that an iterative design process is needed. A "manual" optimization, as well as an automated optimization, is being applied. To achieve a design that represents the best possible solution in a mathematical sense, which is independent of bias, a formalized approach is needed. This approach can be useful in multiobjective and multidisciplinary tasks where the different objectives are incommensurable and/or in conflict, e.g. high stiffness vs. minimal mass of a structure. In multiobjective optimization, a unique solution cannot be defined. It is possible to pursue a Pareto-optimal set of solutions instead.

1.4   Thesis structure

The content of each chapter is summarized as follows:

In chapter 2, the basics of magnetic fusion research are introduced. The characteristics of plasma heating systems, NBI systems and negative-ion sources are discussed. Also, the status of magnetic fusion research is reported.

Chapter 3 Outlines the requirements and the design of an NBI system fro ITER. Special emphasis is placed on the development of negative-ion sources at IPP from small prototypes to half-ITER-size sources. Special attention is given to the description of the physical and technical aspects that are relevant within the framework of this thesis.

In chapter 4, the plasma grid design and its improvement by FEM analysis is explained in detail. In particular, this chapter also describes the electromagnetic and mechanical models for the optimization of the filter field and the mechanical stability of the plasma grid.

In chapter 5, the optimization of the extraction grid cooling circuit is explained. The coupling of the ion beam and the electron trajectories codes with the CFD and thermo-mechanical calculations is presented. The ELISE design is compared to the ITER-SINGAP design of the extraction grid.

Chapter 6 outlines the multidisciplinary optimization. This includes the basics of mathematical optimization, multiobjective optimization and the concept of Pareto front.

Chapter 7 presents the automated multidisciplinary optimization applied to the plasma grid of ELISE using MATLAB and ANSYS. Several design points of the resulting Pareto front are determined. The results as well as limits and advantages of the method are discussed.

Chapter 8 summarizes the key findings of the work, discusses the success of the project and suggests future areas of work.

The methods used in the analysis of the extraction system of ELISE are described in the appendices. The material models, the numerical methods FEM and CFD for evaluation of component behavior, the ray tracing codes for ion beam and electron trajectory simulations are also briefly introduced.

Chapter 2

Magnetic confinement nuclear fusion and plasma heating

2.1 Fusion energy

Fusion energy is released by fusing two light atom nuclei. Since the products of the reaction are lighter than the sum of the reactants, energy is released as given by the formula $E = mc^2$. This process provides energy to the stars, for example when hydrogen nuclei react to produce helium in a multi-step process called proton-proton chain. In the stars this process is possible due to the tremendous gravitational force that compresses the particles to a very high density, heats them and keeps them together long enough to allow fusion reactions to happen. The fusion process in turn sustains the pressure gradient that keeps the star in equilibrium. Unfortunately, the reaction rates of this multi-step proton-proton chain are too low to be exploited as an energy source on earth. Fusion research is focused on the development of reactors that use the two heavier isotopes of hydrogen, deuterium and tritium, with one and two neutrons respectively. The D–T reaction, shown in figure 2.1 provides a higher reaction rate and is therefore more attractive for the use in a fusion power plant [10].

Two atomic nuclei repel each other due to the Coulomb (electrostatic) force. In order to fuse, two atomic nuclei must be accelerated to an energy high enough to overcome the Coulomb barrier. The required energy is of the order of 10 keV, equivalent to a temperature of approximately 100 million °C.[1] A hydrogen gas that is heated to this temperature is fully ionized. This ionized state of gas, in which positively charged atomic nuclei move independently from the negatively charged electrons, is called a plasma and is considered the fourth state of matter for its unique properties. To reach the required temperature and confine the plasma for

---

[1]In fact the thermal energy of a plasma is usually expressed in eV
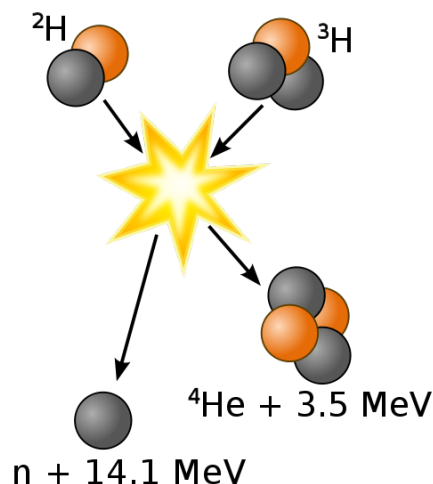
Figure 2.1: Diagram of D–T reaction

long time, several technologies have been subject to research in the last decades. The most promising technology is currently the magnetic confinement.

2.2 Magnetic confinement

The motion of charged particles can be influenced by magnetic fields. In particular they gyrate around the magnetic field lines and are therefore tied to move mainly along them. However, charged particles can diffuse perpendicular to the magnetic field lines through collisions or drifts due to gradients and forces. A good magnetic confinement is required to keep the energetic particles in the plasma away from the material walls of the reactor. In this way, the plasma can be heated to the very high temperatures needed for the fusion reaction.

Early linear machines to magnetically confine plasmas exhibited unacceptable losses of particles at both ends. To overcome this problem toroidal configurations have been developed. In a toroidal configuration the magnetic field is stronger on the inside than on the outside resulting in a $\vec{\nabla}B$ drift which goes in opposite direction for ions and electrons. The resulting electric field and the toroidal magnetic field cause an $\vec{E} \times \vec{B}$ drift of the whole plasma. The solution is to generate a poloidal component of the magnetic field that twists the field lines. In this way top and bottom of the torus are shortcut and the electric field is prevented. The two main approaches to generate this kind of magnetic field are the tokamak and the stellarator.
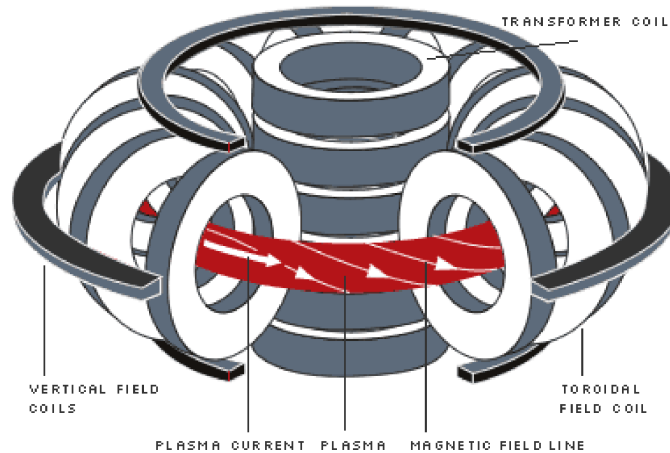
Figure 2.2: Scheme of a tokamak

2.2.1 Tokamak

The poloidal component of the magnetic field can be generated by a toroidal electric current flowing inside the plasma. The current is induced by an additional set of magnets, arranged as a vertical solenoid (also called central solenoid) in the central axis of the torus, similar to a transformer. This solution, called tokamak,[2] was invented by Russian researchers in the 1960s [10]. Currently this is the most developed concept for the realization of nuclear fusion. The next step in the direction of developing a commercial fusion power plant is based on a tokamak device. The international reactor ITER should show that it is technically possible to achieve a considerable energy gain from fusion power with respect to the energy needed to sustain the plasma in stable conditions.

In order to drive a constant current in the plasma, a current ramp is required in the central solenoid. As the ramp cannot exceed a certain maximum current, the tokamak is an inherently pulsed machine in its standard operational scenarios. A possibility for a steady state operation of a tokamak might be provided by non-inductive current drive methods, which, however, are difficult to achieve. Another disadvantage of the tokamak is that due to the presence of a mega-ampere current instabilities in the plasma can lead to violent disruptions that exert considerable forces on the machine structure.

---

[2]tokamak: formed from the Russian words TOROIDALNAYA KAMERA and MAGNITNAYA KATUSHKA, meaning "toroidal chamber" and "magnetic coil"
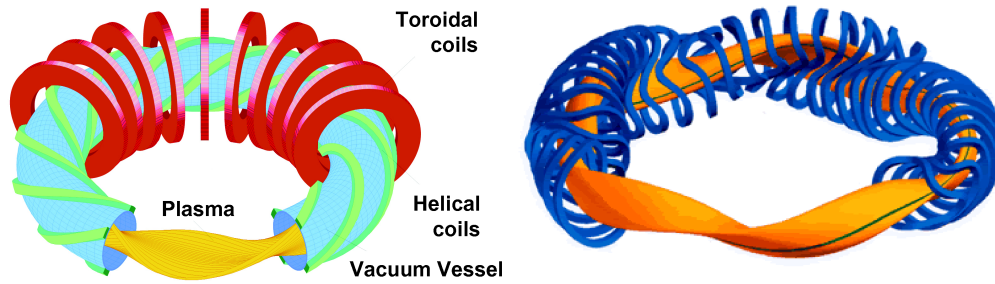
Figure 2.3: First (left) and second (right) generation of stellarator

2.2.2   Stellarator

The stellarator[3] is an alternative possibility to magnetically confine a plasma in a toroidal machine that does not require induced currents and is therefore capable of steady-state operation and free from violent disruptions.

The magnetic field of the stellarator is generated solely by magnetic coils that are shaped such that they generate the necessary twisting of the magnetic field lines and all the necessary magnetic field components to assure stability of the plasma. The first generation of stellarators consisted of planar coils to generate a toroidal component of the magnetic field similar to the tokamak and helical coils wound around the torus to twist the magnetic field lines, as shown in figure 2.3.

The second generation of stellarator (such as Wendelstein 7-X) joins these two types of coils to non-planar toroidal coils with a complex geometry, as shown in figure 2.3, that generate all magnetic field components.

2.3   Plasma heating and non-inductive current drive

To initiate the fusion reaction, the magnetically confined plasma must be maintained at temperatures of the order of 10 KeV. Several heating methods are employed, as explained in the following sections. Some of these heating methods are also used to enhance plasma stability or confinement and may be essential for the operation of the future fusion power plant.

2.3.1 α-particle heating

When the conditions for the fusion reaction are reached, considerable amounts of energetic He nuclei, or α-particles, and neutrons are produced. The α-particles

---

[3]Stellarator: the name refers to the possibility to harness the power source of a stellar object.

have an energy of 3.5 MeV and can be confined magnetically, being positively charged. Through collisions with the other plasma particles they heat the plasma and sustain the fusion reaction. The neutrons, with an energy of 14.1 MeV, leave the plasma undisturbed.

2.3.2   Ohmic heating

Plasma can conduct current and exhibits a certain electrical resistivity. Therefore a plasma can be heated by ohmic heating. In a tokamak a strong current is induced like in a transformer via the central solenoid. In plasmas the resistivity is principally dependent on the temperature of the electrons, being proportional to $1/T_e^{3/2}$. Therefore a strong current can heat the plasma only up to 2–3 KeV as ohmic heating becomes less effective at higher temperatures. The typical ohmic heating power is in the range of 1 MW, depending on the machine size. In a stellarator this heating method cannot be used because no plasma current exists.

2.3.3   High frequency heating

The ionized particles of the plasma are moving along the magnetic field lines and rotating around them. This rotational component is called gyration and can be described by a gyration radius and a gyration frequency. If an electromagnetic wave with a frequency that matches the gyration frequency of the particles is introduced in the plasma, the plasma particles can absorb energy from the wave. The gyration frequency depends on the magnetic field strength B. In toroidal magnetic fields B decreases with the major radius, so the power deposition can be quite local. Three types of heating frequencies are distinguished:

- Ion Cyclotron Resonance Heating (ICRH)

  For the ICRH the frequency of the electromagnetic wave is in the range of the ion gyration frequency, between 20 and 100 MHz. The typical heating power in modern experiments is of the order of 10 MW.

- Electron Cyclotron Resonance Heating (ECRH)

  The ECRH has a frequency in the range of the electron gyration frequency, between 30 and 170 GHz. In modern experiments ECRH power accounts for several MW.

- Lower Hybrid

  So-called lower hybrid waves propagate in the plasma at frequencies between the electron and ion cyclotron frequencies. When these waves are launched in the plasma they can drive a current with good efficiency and this allows

some control of the current profile. The frequency lies in between 1 and 8 GHz and the power delivered to the plasma is typically of the order of 10 MW.

2.3.4 Neutral beam heating

Another method to heat the plasma is to inject energetic neutral particles. Usually, hydrogen or deuterium atoms are chosen to heat H or D plasmas, respectively, in order to avoid contamination and to supply fuel for the fusion reaction. The injected fast particles are ionized by collisions with the plasma particles, and are then confined by the magnetic field. They transfer their energy to the plasma by subsequent collisions. The spatial distribution of the power deposited in the plasma depends on the plasma density and temperature, on the injection geometry and on the neutral beam energy [11]. For ASDEX Upgrade, with a plasma density of 5×10^{19} m^3 at 93 keV deuterium neutral beam, the penetration depth λ is about 0.5 m, comparable to the minor radius of the torus.

The beam is preferably injected with a large toroidal velocity component to reduce the amount of particles trapped in the so-called "banana" orbits, characterized by a high particle loss rate [10, 11]. In addition, if the neutral beam is directed tangentially inside the plasma vessel, a non-inductive plasma current can be driven. This helps to extend the pulse length of a tokamak.

The neutral beam injection provides the larger portion of the heating power in modern fusion machines [12]. In the large fusion experiments the heating power delivered by NBI systems is of the order of 20 MW. The ITER NBI system, shown in figure 3.14, will consist of 2 injectors, each delivering 16 MW power at 1 MeV particle energy using negative ions.

2.4 State of fusion technology

2.4.1 Energy gain factor and ignition

Energy gain factor Q The fusion reaction produces energetic particles as explained in section 2.1. The total fusion power (sum of the energies of α-particles and neutrons) can be designated as P_{fus}. The energy from α-particles is designated $f_{\text{ch}}P_{\text{fus}}$, with $f_{\text{ch}} = 0.2$, while the rest, $(1 - f_{\text{ch}})P_{\text{fus}}$, is carried by neutrons that cannot be confined by the magnetic field. The neutrons end their trajectories at the walls of the reactor, where their thermal energy can be used to heat up a working medium that in turn is used to produce electricity.

The total power entering into the fusion reactor is designated P_{heat}. The ratio

$$Q = \frac{P_{\text{fus}}}{P_{\text{heat}}} \tag{2.1}$$

is the gain factor Q.

Break-even and ignition   The case $Q = 1$ is called the "break-even". When the energy delivered by α-particles to the plasma is high enough to keep the plasma at the temperature necessary to sustain the reaction in steady state the plasma has reached "ignition", no external heating is necessary and Q is infinite. In practice heating methods are needed to control the plasma and to obtain higher confinement. In addition, ignition is not necessary for the commercial use of fusion energy, as a gain factor $Q \approx 15$–30 is enough for a practical reactor.

Lawson criterion   For the fusion reaction to happen and to be economically competitive, high temperatures are not enough. Two other parameters have to be considered, namely the plasma density and the confinement time. The number of particles taking part in the reaction, the plasma density, must also be high. In addition, the energetic particles generated by the fusion process and those injected or heated by external heating methods must be confined inside the plasma long enough. This confinement time is defined as the *energy confinement time*

$$\tau_{\text{E}} = \frac{W}{P}, \tag{2.2}$$

where W is the total energy in the plasma and P is the applied power. For instance, to reach ignition without external heating the energy from α-particles $f_{\text{ch}}P_{\text{fus}}$ must be equal to the power losses W/τ_{E} in the plasma. The Lawson criterion [13] is a figure of merit that defines the conditions needed for a fusion reactor to reach ignition. For T between 10 and 20 keV, the Lawson criterion gives a minimum required value for the "triple product" of the plasma density n, confinement time τ_{E} and ion temperature T;

$$nT\tau_{\text{E}} \geq 5 \times 10^{21} \text{ keVs/m}^3. \tag{2.3}$$

The ideal plasma temperature and density are determined by the cross section for the D–T reaction and the bremsstrahlung[4] and are of the order of $T \approx 10$–20 keV and $n_{\text{e}} \approx 10^{20}$ m^{-3} respectively. To reach ignition the energy confinement time must be of the order of $\tau_{\text{E}} \approx 1$–$3$ s. Although these values have already been reached separately in the biggest fusion reactors, the triple product defined by the Lawson criterion has not yet been achieved in any existing device.

---

[4]Bremsstrahlung: from the German words *bremsen* "to brake" and *Strahlung* "radiation", i.e. "braking radiation", is the electromagnetic radiation produced by the acceleration of a charged particle when deflected. It is a type of undesired plasma cooling.

2.4.2   Present experiments

Currently the Joint European Torus (JET) in Culham, England, the largest existing fusion experiment in the world, holds the record of produced fusion power. During a full D–T experimental campaign in 1997, JET reached a peak fusion power $P_{\text{fus}} = 16$ MW, with an energy confinement time $\tau_{\text{E}} \approx 1$ s, ion temperature $T_i = 30$ keV, electron density $n_e = 5 \times 10^{19}$ m^{-3} and gain factor Q between 0.6 and 0.9 [14].

2.4.3   The future: ITER and DEMO

ITER has been designed to produce 500 MW fusion power with gain factor $Q = 10$, using a plasma that is primarily heated by α-particles from fusion reactions [15]. This is obtained mainly via an improvement of the energy confinement time with respect to JET, which can be achieved by increasing the plasma size. The major radius of the ITER vessel will be 6.2 m, about twice as large as the radius of JET ($R = 3$ m). Construction of the ITER facility began in 2008 in Cadarache in the south of France and first plasma production is expected in 2018 [16].

The next step in the development of a fusion power plant will be a Demonstration Power Plant (DEMO) [17]. DEMO will be a commercial fusion plant prototype capable of delivering electricity to the electrical grid.

From an engineering point of view several important challenges must still be overcome before a commercial fusion plant can be realized, such as the development of low activation materials capable of resisting the fast neutron fluxes during the plant lifetime. A special material testing facility, the International Fusion Materials Irradiation Facility (IFMIF) [18], will address this issue.

Chapter 3

Neutral beam injection for ITER

3.1 Overview of an NBI systems

To understand a complex system such as a negative-ion source for NBI, and in particular its extraction system, the NBI system and the technical requirements for ITER are introduced in this chapter.

A schematic description of a neutral beam injection system is given in figure 3.1. The neutral beam injection requires the following steps:

- Generation of a plasma in an ion source.

- Generation of a fast ion beam by means of acceleration grids.

- Neutralization of the ion beam by the neutralizer.

- Removal of non-neutralized particles.

3.1.1 Ion source

The core component of the neutral beam injection system is the ion source. Here neutral gas is injected into a vacuum chamber and ionized. Positive as well as negative ions can be produced. Ionization can be achieved by different techniques. The quality of the ion source affects beam properties such as homogeneity and the extracted current. The development of high-performance ion sources is therefore one of the most important objectives of research for NBI systems.

The most advanced heating devices in ongoing experiments are positive-ion-based neutral beam injection systems. These systems are routinely operated in almost all the experiments in the fusion community, such as ASDEX Upgrade, as a basic heating device [19, 20].
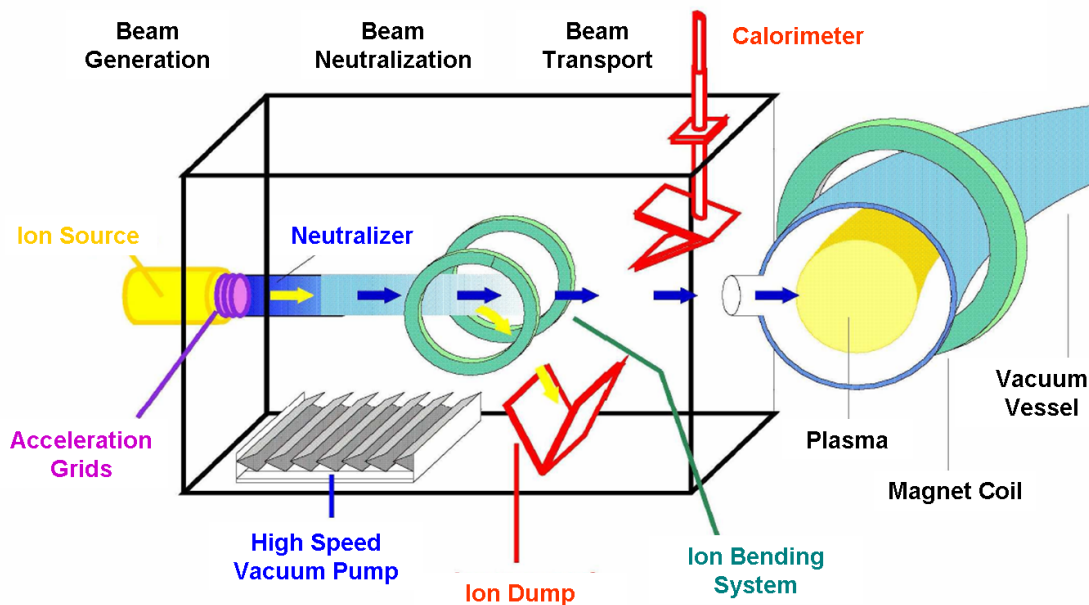
Figure 3.1: Scheme of neutral beam injection

The hydrogen plasma in a positive-ion source has a relatively low degree of ionization and dissociation. In sources for positive ion based systems, ions can easily be extracted by applying a negative extraction voltage using electrodes with many apertures. Typically 3 or 4 electrodes are used with many apertures of about 1 cm in diameter, forming many electrostatic lens systems. positive-ion sources deliver current densities in the range of 2500(2000) A/m^2 H$^-$(D$^-$) [21, 22] and accelerate positive ions to energy of the order of 100 keV.

Positive-ion sources also produce a certain amount of molecular ions (D^{+2}, D^{+3}) that are accelerated as well. These ions are converted into neutral atoms with only a half and a third of the nominal energy.

Two types of ion sources are in use by current neutral beam injectors: *arc*-sources and *RF*-sources. Both types are used at IPP on the ASDEX Upgrade neutral beam injection system with positive ions [21].

Arc sources   Arc sources have been used since the development of the first NBI systems. The arc source is based on an arc discharge between tungsten filaments and the source walls. Tungsten filaments are heated to temperatures between 1700–2700°C and are used as cathodes. Electrons are emitted from the hot tungsten filament and accelerated by a DC voltage of about 200 V into the source wall (anode). Arc-driven negative-ion sources are characterized by relatively high power loads deposited on the source walls and the plasma grid. The tungsten

from the filaments evaporates continuously into the source during operation, which limits the lifetime of the filaments and makes frequent venting of the ion source necessary for their replacement. For ITER, the filaments would have to be replaced twice a year by a remote handling tool in a radioactive environment. In addition, the evaporating tungsten deposits on the inner walls of the source changing the characteristics of the ion source surface.

RF sources The other type of source is the RF source. The power is coupled into the plasma from an RF-antenna. RF sources have demonstrated their reliability on ASDEX Upgrade, where four 2.5 MW RF sources for positive ions are in use [19, 20]. This is currently the only NBI system for fusion experiments in the world that uses RF sources.

There are many advantages of RF sources. The coil can be positioned outside the plasma chamber without contact with the plasma. The absence of filaments in the discharge and the simplicity of the design (few electrical connections, instead of 25 connections in arc sources with 24 filaments) make the operating life of the RF source longer and practically maintenance-free.

In radio-frequency sources an oscillatory electromagnetic field is used to accelerate free electrons, which in turn build up the plasma by ionization collisions. Two processes of plasma generation can be used: *capacitive* and *inductive* coupling. In the capacitive coupling, the electrons are heated by an oscillating electric field between two conductors. An inductively coupled plasma is achieved by applying an oscillating current to a coil. The coil produces the alternating magnetic and electric fields necessary to heat up the electrons.

3.1.2   Extraction

The ion beam is usually generated by extracting the hydrogen ions electrostatically from a hydrogen plasma source. The ions are then accelerated to high energies (from several tens of keV up to 1 MeV). To avoid aberration effects on the ion optics, the beam has to be divided into many small beamlets using electrodes with multiple apertures. Many of these small beamlets combine to one large beam downstream of the extraction system. Ion beams for neutral beam injection characteristically have high beam current of tens of amperes to achieve a power of the order of several MW. Consequently large beam cross-section, typically hundreds of cm^2, are necessary.

3.1.3   Neutralization

To neutralize the accelerated ions, the beam is sent through a gas target (neutralizer) with gas pressure in the range of 0.1–0.5 Pa [23]. Here, the fast particles of

the ion beam are neutralized by charge-exchange collisions with the colder hydrogen molecules of the neutralizer. A gas density of the order of 10^{19} m^3 is required in the neutralizer within the NBI system. Hence, high-speed vacuum pumps are necessary to remove the hydrogen gas around the neutralizer to create the proper vacuum conditions to connect the NBI system to the plasma vessel.

3.1.4   Magnet and beam dumps

Fast residual ions within the neutral beam represent a significantly large fraction of the total beam power. The exact value depends on the neutralization efficiency. These fast ions can create high power loads on the components of the fusion experiment. A bending magnetic [24] or electric [25] field is used to deflect the ions onto an ion dump. This is a critical component of the NBI, subject to heavy heat loads and requiring active water cooling.

The remaining high energy neutral particles are then injected into the fusion device. A calorimeter can be placed in the NBI system to measure the beam power and to allow conditioning of ion source and accelerator.

3.2   ITER requirements

As mentioned in section 2.3.4, the neutral beam heating system for ITER will require a neutral beam with a particle energy of 1 MeV. This particle energy was chosen in order to satisfy the central heating and current drive requirements for ITER [26] and to reach the total neutral beam power of 33.2 MW, delivered by two tangentially arranged injectors [7].

The energy requirements for the ITER NBI cannot be achieved by a neutral beam system based on the production and neutralization of positive ions. It requires the development of negative ion technology.

3.2.1   Why negative ions?

Positive ion based systems have a serious drawback when operated with high particle energy: the neutralization efficiency decreases drastically if the positive ion energy exceeds 100 keV/nucleon. Figure 3.2 shows the neutralization efficiency for positive and negative deuterium ions [27]. It can be seen that the neutralization efficiency goes almost to zero for positive deuterium ions (deuterons) with an energy of 1 MeV.

As a consequence the conversion efficiency[1] of a positive ion based neutral beam

---

[1]Here the conversion efficiency of the heating and current drive system is meant: $\eta_{\mathrm{CDconv}} = P_{\mathrm{HCD}}/P_{\mathrm{eHCD}}$, which is the ratio of P_{HCD}, the power launched by the heating and current drive
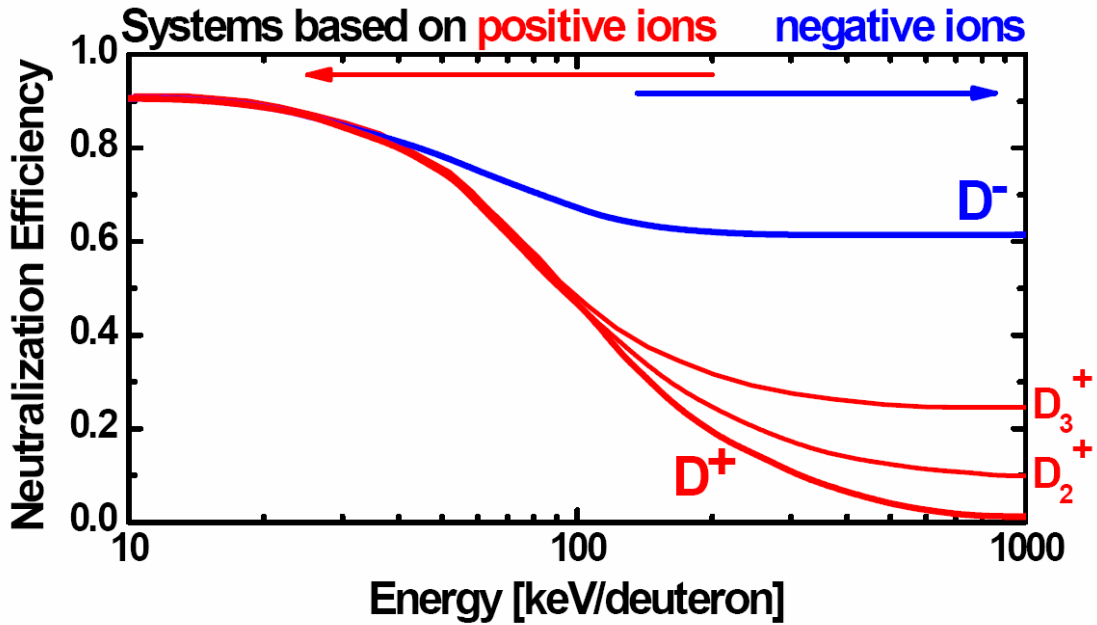
Figure 3.2: Maximum neutralization efficiency for a neutral beam injection system based on positive or negative deuterium ions (deuterons) with respect to their energy [27].

injection system, at its present stage in the range of 20–30% [28], would be even lower at the high particle energy required by the ITER NBI.

On the other hand, the neutralization efficiency of negative ion based neutral beam injection (N-NBI) systems is affected by the particle energy to a much lesser extent. Even for particle energies in the range of several hundred keV/nucleon, the neutralized particle fraction is of the order of 60%.

3.2.2 Detailed requirements

For ITER, a negative ion current of 40 A per beam line is required in order to generate a heating power of 16.6 MW per NB injector. The beam power has to be maintained for a pulse duration of 1 h. To provide the 40 A total current a negative-ion source with dimensions of approximately 1.9×0.9 m^2, with an extraction area of the same size and a net extraction area of all apertures of 0.2 m^2, delivering a current density of 200 A/m^2 in D is necessary.

In addition, in negative-ion sources electrons are co-extracted and must be removed immediately after their extraction, when their energy is only of the order of 10 keV. To avoid excessive heating of extraction and acceleration grids, it is necessary to maintain the extracted electron-to-ion current density ratio $j_e/j_{H^-} < 1$.

(H&CD) system, to P_{eHCD}, the overall electric power used to operate the system.

Table 3.1: Target operational parameters for the negative-ion sources of the heating and diagnostic neutral beam system for ITER [26].

Parameter	Heating Beam	Diagnostic Beam
Accelerated Current Density	> 200 A/m^2 (D)	> 300 A/m^2 (H)
Electron-to-Ion Ratio	< 1	< 0.5
Accelerated Current	> 40 A	> 60 A
Beam Energy	1 MeV	100 keV
Pulse Length	up to 3600 s	3 s every 20 s
Beam Homogeneity	±10 %	
Source Pressure	< 0.3 Pa	< 0.3 Pa

Furthermore, the operational pressure of the ion source has to be limited to 0.3 Pa in order to reduce stripping losses by collisions with residual gas particles in the extraction and acceleration systems [29].

Besides the heating neutral beam, an additional diagnostic neutral beam system based on negative ions is planned for ITER. This serves to measure the amount of helium ash inside the ITER tokamak. It will do so through charge exchange spectroscopy (CXRS). Table 3.1 gives an overview of the ITER requirements regarding the N-NBI for both systems [26].

3.3 RF-driven sources for negative ion beams

The RF-driven ion source for NBI consists of three regions: driver region, expansion region, and extraction region. Figure 3.3 shows a schematic overview, while figure 3.4 shows the corresponding CAD drawing of the RF-driven ion source for NBI.

While positive hydrogen ions can be extracted directly from the plasma boundary, the physics of production, transport and extraction of negative ions is more complex [30]. In general, negative hydrogen ions can be generated by two mechanisms: *volume* processes [31] or *surface* processes [32]. Both processes have been applied in small negative-ion sources with mono-aperture extraction systems. Examples of surface H$^-$ sources are the SNS[2] [33] and LANSCE[3] [34] spallation neutron sources while volume H$^-$ sources are used at DESY[4] [35] and CERN[5] [36].

---

[2]SNS: Spallation Neutron Source, ORNL, Oak Ridge, Tennessee, USA

[3]LANSCE: Los Alamos Neutron Science Center, LANL, Los Alamos, New Mexico, USA

[4]DESY: Deutsches Elektronen SYncrotron, (German Electron Synchtrotron), Hamburg, Germany

[5]CERN: Conseil Européen pour la Recherche Nucléaire (European Council for Nuclear Research), Geneva, Switzerland
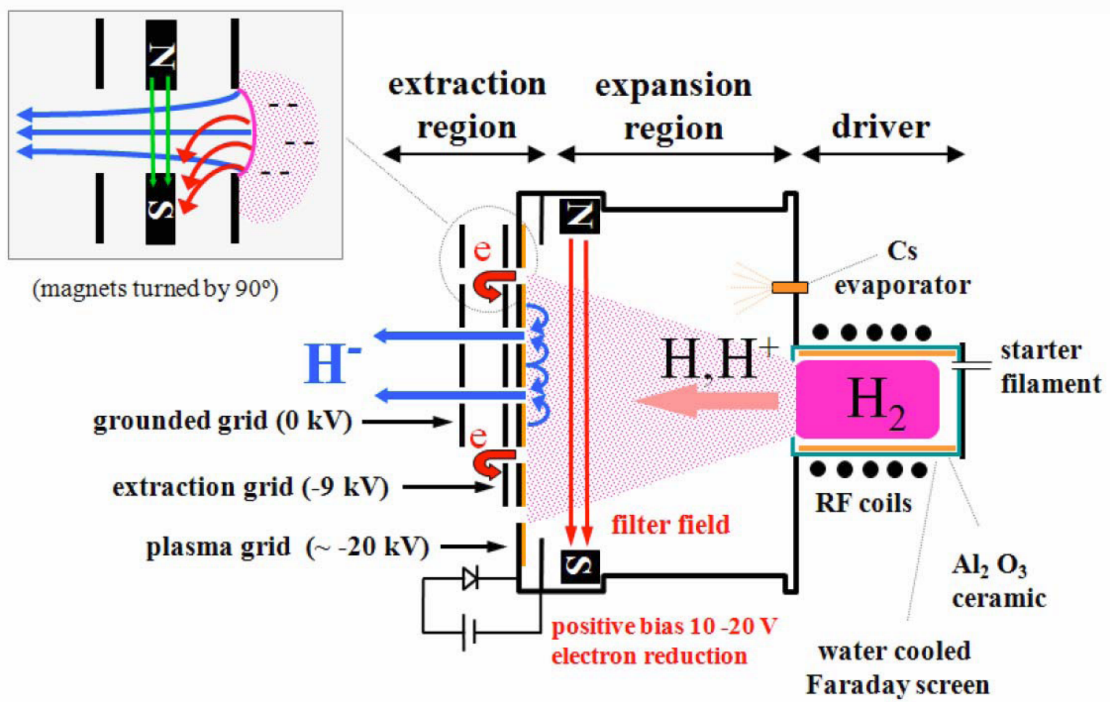
Figure 3.3: Scheme of the RF-driven ion source for NBI. In the box top left, the principle of the suppression magnets for the co-extracted electrons is shown.

Volume production   In the volume process negative ions are generated in the plasma volume by dissociative attachment of slow electrons ($T_e \approx 1$ eV) to hydrogen molecules on high vibrational states [37],

$$\mathrm{H}_2(\nu") + \mathrm{e}_{\mathrm{slow}} \rightarrow \mathrm{H}^0 + \mathrm{H}^-, \tag{3.1}$$
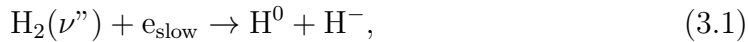
where the vibrational excitation $\nu" \geq 5$ ($\nu" \geq 8$) for hydrogen (deuterium) molecules ensures a high cross-section [38].

Despite intense development efforts, this type of negative-ion sources has shown severe limitations:

- Low extracted negative ion current density and high extracted electron to ion current ratio.

- High operating pressure that induces very high stripping losses in the extraction system.

Surface Production   This process consists of the conversion of neutral hydrogen atoms and positive hydrogen ions from a plasma source into negative ions at a metallic surface with a low work function (converter surface),

$$\mathrm{H}_{\mathrm{x}}^+, \ \mathrm{H} + \mathrm{e}(\mathrm{surface}) \rightarrow \mathrm{H}^-, \tag{3.2}$$
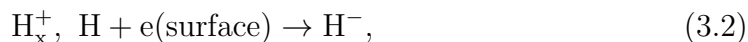
with $x = 1, \ 2, \ 3$.

The surface process presents decisive advantages with respect to the volume process:

- The negative ion yield is increased by a factor of 10 with low co-extracted electron to ion current ratio (< 1)

- The operating pressure can be decreased to 0.3 Pa

Cesium reduces the work function of the walls where impinging neutral atoms and positive ions can get one or two electrons respectively and are accelerated back to the plasma by the plasma sheath potential. The minimum work function is achieved by deposition of 0.5–0.7 monolayers of cesium on a molybdenum substrate [39–44].

It has been observed that the negative ion yield is dependent on the temperature of the plasma grid in the extraction region, which could be experimentally related to a decrease of the work function [45]. The optimum temperature of the converter surface lies between $100\,^{\circ}\mathrm{C}$ and $200\,^{\circ}\mathrm{C}$ [46].

Currently, only the negative-ion sources based on surface processes can achieve the requirements for the ITER NBI source.

3.3.1 Surface-production-based negative-ion sources

In negative-ion-based systems, the extracted current density is up to
330(230) A/m^2 H$^-$(D$^-$) [46, 47]. This is typically a factor of 10 lower than for
positive ion based systems. Therefore, in order to extract the same ion current
from a negative-ion source as from a positive-ion source, the extraction area has
to be 10 times larger.

Currently, arc-driven negative ion based systems are routinely being operated
at the fusion experiments LHD[6] and JT-60[7] in Japan with beam energies in the
range of hundreds of kV and extracted current densities in the range of 100–
150 A/m^2 [8, 48–50].

The production and extraction of negative ions in RF sources based on surface
processes can be divided into four steps.

- Positive and atomic hydrogen particles are generated in a RF-driven plasma
  driver.

- The plasma expands into the source body (expansion region), where a mag-
  netic filter field removes the hot electrons ($T_e > 2$ eV) that can destroy
  negative ions.

- The positive and neutral hydrogen particles hit a cesium-covered plasma grid
  (the yellow grid in figure 3.4), also called converter surface. The low work
  function of the converter surface enhances the conversion of positive ions and
  neutral atoms into negative ions by picking up surface electrons.

- A positive extraction voltage of the order of 10 kV is applied to extract
  negative ions and to form the ion beam.

3.3.2 Driver

In the IPP prototype negative-ion source BATMAN, the plasma is generated by
inductive coupling of 1 MHz RF power to hydrogen gas inside the driver. A water-
cooled coil with 6 turns is wrapped around a ceramic Alumina (Al$_2$O$_3$) cylinder
of diameter $\varnothing = 24.5$ cm, length l = 15 cm and wall thickness 8 mm placed on
the back-plate of the source. The coil is connected to an RF generator capable of
delivering up to 100 kW of power at 1 MHz. A water-cooled and tungsten-coated
Faraday Screen is introduced inside the cylinder to protect it against thermal
loads and erosion by plasma sputtering. A temporary gas puff together with an

---

[6]LHD: Large Helical Device, superconducting stellarator, National Institute for Fusion Science (NIFS), Japan

[7]JT-60, Japan Torus, tokamak, Japan Atomic Energy Research Institute (JAERI), Japan

electron emitting ThO_2-coated tungsten starter filament at the backside of the driver ensures a reliable plasma start-up.

The source volume is evacuated by the large vacuum pumps of the neutral beam box through the apertures of the extractor system down to a pressure of 10^{-3}–10^{-4} Pa. During the pulse, gas is injected into the driver at a pressure of 0.3 Pa. Electron densities $n_e = 10^{18}$ m^3 and electron temperatures $T_e > 10$ eV are obtained in and close to the driver [51, 52]. Plasma parameters in the expansion region are significantly different to avoid massive destruction of negative ions by electron stripping.

### 3.3.3   Expansion chamber and filter field

The expansion region contains several magnet boxes at the peripheral regions of the chamber at a distance of 2 cm (see red bars in figure 3.4) to the plasma grid. Here, the magnetic filter field is generated to reduce electron temperature and density. Typical electron temperatures $T_e < 2$ eV and electron densities $n_e = 5 \times 10^{17}$ m^3 are obtained [53]. Furthermore, a cesium oven is attached to the expansion chamber, evaporating the alkaline metal from a liquid reservoir into the expansion region of the ion source in order to generate a thin cesium layer on the plasma grid.

Cesium (see yellow ampules in figure 3.4) is continuously injected at a constant rate of 10 mg/h from the nozzles (see yellow pipe in figure 3.4) of the oven at the backplate of the expansion chamber.

The expansion chamber is temperature-controlled by an internal water circuit and is covered internally by a layer of 1 mm of copper to increase the temperature uniformity of the surface. The temperature of the source is set to 40-50°C and its control is crucial to avoid cold spots for cesium condensation that act as cesium sinks.

The hydrogen plasma in the negative-ion source has a relatively low degree of ionization ($\approx 1\%$) and dissociation ($\approx 10\%$) [53]. Negative ions form only a small part of the total hydrogen plasma and have a special production process. The additional electron of the negative ion has a very low binding energy (0.75 eV). For this reason the neutralization efficiency is high, but for the same reason negative ions are very vulnerable and subject to destruction processes already in the plasma source.

Therefore, negative hydrogen ions have a limited survival length of a few cm until a neutralization collision takes place. As a consequence, the surface area of the plasma grid close to the extraction apertures contributes dominantly to the extracted negative ion beam. The cesium conditions of the plasma grid surface are extremely important for the extracted negative ion current. The use of a plasma grid temperature of 150±50 °C has been found to be beneficial for the source performance [46].
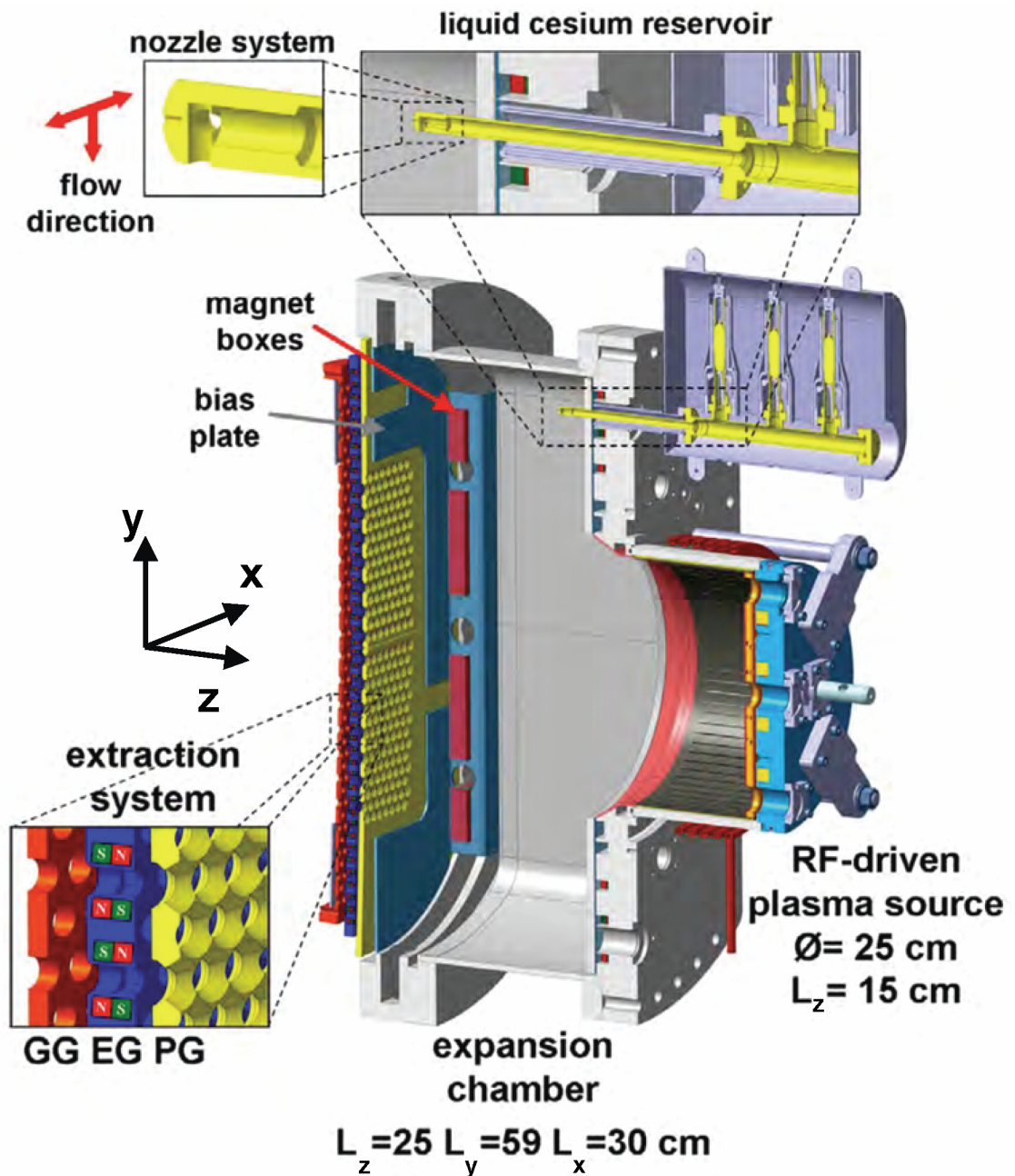
Figure 3.4: Vertical cross section of the RF-driven ion source prototype BATMAN. The cesium evaporation oven and the three grids (plasma grid, extraction grid and Grounded Grid) of the extraction system are emphasized.

The holes of the plasma grid are chamfered to increase the area available for the conversion of neutrals and positive ions to negative ions, to provide a more suitable starting angle of the negative ions and to enhance the homogeneity across the extraction holes by the increased clearance around the extraction area [46].

A certain fraction of the surface-generated negative ions is transported through the source plasma into the multi-aperture system of the plasma grid (see yellow PG apertures in figure 3.4). Here, they are focused into an ion beam by the extraction electric field. The penetration depth of this field is limited because of the field compensation by the space charge of the plasma particles.

Applying a bias voltage[8] between the plasma grid and the source body is an efficient way to reduce the number of co-extracted electrons

The shape and strength of the magnetic filter field is important for the reduction of co-extracted electrons and the increase of extracted H^-. Experiments performed at IPP show a clear correlation between the magnetic filter field in front of the PG and the extracted negative ion current density [54], as shown in figure 3.5. The optimum value for maximum H^- extraction is reached at 3 mT and remains flat for higher FF strength.

In addition, a strong magnetic field in front of the extraction area is also useful to reduce co-extracted electrons [55]. Experiments have shown that in this case the relevant parameter is the integral of the B_x component in the direction of the source of energetic plasma particles, i.e. the driver for RF sources. The electron to ion ratio is dependent on the $\int B_x dz$ calculated between the PG and the driver exit. Preliminary results show that the $\int B_x dz$ necessary to minimize the co-extracted electron current density is in the range of 1–1.5 mT·m (strength at the center of the ion source), as shown in figure 3.6 [54].

3.3.4   Beam extraction

An extraction system with three grids is used for the ion beam formation and to filter out the co-extracted electrons. The grids are called plasma grid (PG), extraction grid (EG) and grounded grid (GG). In the first gap between PG and EG, an extraction voltage of U_{ex}=5–10 kV is applied. A second voltage of U_{acc}=10–20 kV is used in order to focus the filtered negative ion beam onto a calorimeter for measurement of the accelerated current density.

negative-ion sources are characterized by the co-extraction of electrons together with the negative ions, due to equal polarity. If the electrons are accelerated

---

[8]The bias voltage changes the potential distribution and the fluxes of particles inside the ion source. A low bias voltage influences the electrons, reducing their flux towards the extraction region. If a high bias voltage is applied, also the negative ions flux is reduced. An optimum value of bias voltage reduces the co-extracted electrons and does not decrease significantly the extracted negative ions.
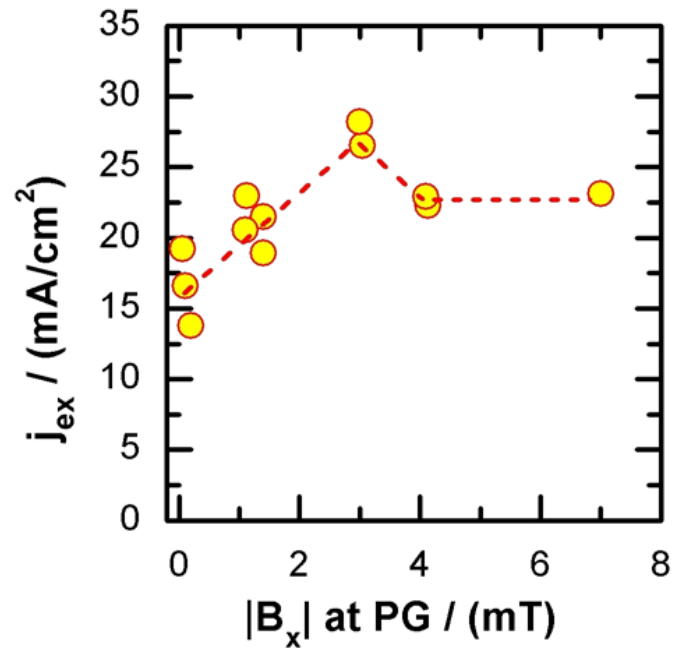
Figure 3.5: Correlation of extracted negative ion current density with B_x component of magnetic field in front of PG
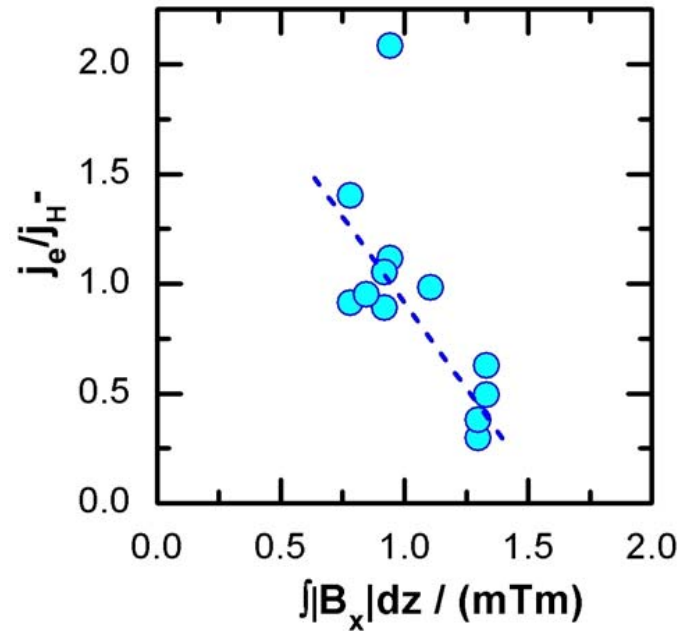
Figure 3.6: Correlation of electron to ion ratio and $\int B_x dz$

to high energies, they can create serious damage to accelerator grids and other beamline components, such as the neutralizer. In addition, accelerating electrons to full energy and removing them later in the residual ion dump represents a waste of energy. Hence, the co-extracted electrons have to be removed at low particle energies and thermalized on an appropriate electron dump.

The removal of the co-extracted electrons is realized by a magnetic field generated by Sm_2Co_{17} magnet rods embedded into the extraction grid. The magnetic field bends the electron trajectories so that the electrons impinge onto the extraction grid surface, producing a localized heat load of the order of 40 MW/m^2. However, D$^-$/H$^-$ ions can still pass through the filter nearly unaffected because of their higher mass. Figure 3.7 shows a numerical simulation of a beam of D$^-$ ions and electrons for an extraction system with 14 mm aperture diameter computed with the KOBRA3 code [56].

In addition, the electron deflection field (EDF) penetrates into the plasma source, superimposes locally with the FF, and influences the extraction of ions as well as electrons. It has been shown that the EDF has to be sufficiently high to suppress the co-extracted electrons [46].

The heat generated on the EG by co-extracted electrons must be removed by a water-cooling system. Despite the use of the cooling circuit, the extraction grid can be damaged if the heat load is too high. This can happen if the co-extracted electron current is higher than in normal operation. The maximum heat load that can be tolerated by the extraction grid without damage is a limiting factor for the performance of the ion source. An optimal performance of the EG cooling circuit is therefore desirable. The design of this optimized cooling circuit is one of the goals of the present work (cf. chapter 5).

3.4   From single-driver testbeds to a full size ITER source

The measurements of physical parameters which are important for the optimization of the negative-ion source are performed at the NBI group of the IPP technology department. Three test facilities are used: BATMAN,[9] MANITU,[10] and RADI.[11] The test facilities BATMAN and MANITU have moderately sized ion sources (0.59×0.32 m^2), while the test facility RADI has a source with approximately half the size (0.80×0.80 m^2) of the future ITER source (1.90×0.90 m^2), as shown

---

[9]BATMAN: Bavarian Test Machine for Negative Ions, IPP Garching, Germany

[10]MANITU: Multi Ampere Negative Ion Test Unit, IPP Garching, Germany

[11]RADI: built with parts from a former RADIal neutral beam injector, IPP Garching, Germany
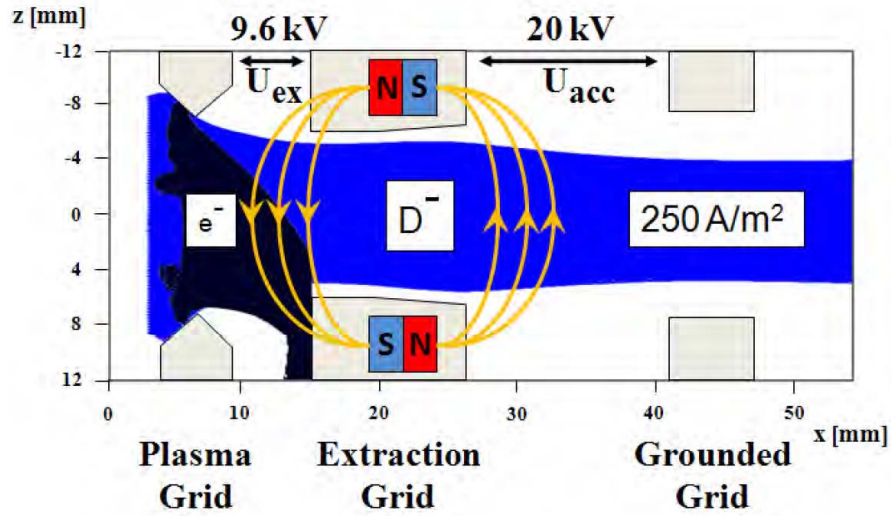
Figure 3.7: Simulation of the extraction and beam formation of a negative deuterium ion beam (blue) in a three stage extraction system for a negative-ion source with an extracted ion current density of 250 A/m^2. The suppression magnets have been rotated by 90° (along the z axis) to show the electron deflection field that bends the co-extracted electron trajectories (black), hitting the extraction grid.

in figures 3.8 and 3.9. Specifications and achieved operational parameters of the three existing test facilities and the ITER requirements are given in table 3.2.

BATMAN   The first facility, BATMAN [46] has the dimension of a JET-PINI[12] source [12], circa 1/8 of the dimension of the future ITER source, and has been used as "proof of principle" to show the efficiency and reliability of the RF concept for the production of negative hydrogen ions.

   With the IPP RF-driven prototype source on BATMAN, accelerated current densities of 330 A/m^2 with H$^-$ and 230 A/m^2 with D$^-$ [46] have been achieved at the required source pressure of 0.3 Pa and with a sufficiently low electron-to-ion ratio (< 1 D$^-$, < 0.5 H$^-$). However, BATMAN has a small extraction area and limited pulse length of several seconds.

   The IPP negative-ion source test facilities can be operated with hydrogen and deuterium. Both modes are required for the ITER heating and diagnostic neutral beams. However, the use of hydrogen is preferred during source conditioning and for experimental studies.

   The interaction of implanted deuterium in the calorimeter with the deuterium ion beam results in the production of fast neutrons with 2.45 MeV of energy and radioactive Tritium by the D-D fusion reactions:

---

[12]PINI: PLUG IN NEUTRAL INJECTION

Table 3.2: Comparison between source parameters required by ITER, those achieved in IPP negative-ion sources and those of the new test facility ELISE (p_s source pressure, V_{ex} extraction voltage, t_p pulse duration, D_s source dimensions, D_{ex} extraction surface dimension, h beam homogeneity).

		BATMAN	MANITU	RADI	ELISE	ITER
j_{H^-} $\left[\frac{A}{m^2}\right]$	(D⁻)	230	120	-	200	200
	(H⁻)	330	150		300	300
p_s [Pa]		0.3	0.3–0.4	0.3	0.3	0.3
j_e/j_{H^-}	(D⁻)	< 1	1.5–2	-	< 1	< 1
	(H⁻)	< 0.5	< 1		< 0.5	< 0.5
V_{ex} [kV]		9–11	9	-	10	9–10
t_p [s]		< 10	200	< 10	3600ᵃ	3600
D_s [m²]		0.32×0.59	0.32×0.59	0.8×0.8	0.9×0.9	0.9×1.8
D_{ex} [cm²]		70	190	-	1000	2000
h [%]		-	-	< 10ᵇ	±10	±10

ᵃ Plasma pulse: 3600 s; extraction: 10 s every 180 s.
ᵇ For plasma.
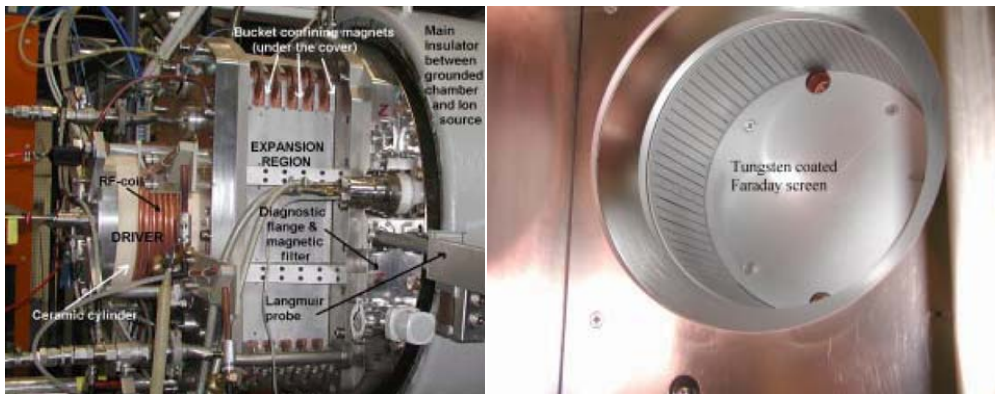
Figure 3.8: BATMAN source from the outside (left) and the inside (right), where the Faraday Screen is visible

Figure 3.9: Ion source of MANITU (left), with a single driver, and of RADI (right), with four (2x2) RF-drivers. The RADI source is approximately half the size of the ITER source (with 2×4 drivers).

$$D + D \rightarrow {}^3He + n$$
$$D + D \rightarrow T + p \qquad\qquad (3.3)$$

Hence, long-pulse deuterium operation requires a neutron shield around both the calorimeter and the ion source as in MANITU or a remote control system as done in BATMAN. In addition to the radioactive effects, the physics of deuterium discharges differs from that of hydrogen. The co-extracted electron current is higher for deuterium operation, which results in a higher power load on the extraction grid. This limits the allowable RF power and thus the maximum D^- current density. With an increased filter field, produced by additional magnet rods near the PG, the electron-to-ion ratio can be reduced. However, a ratio below $j_e/j_{H^-} < 0.5$ that is easily accessed with hydrogen pulses has not yet been achieved with deuterium [46].

MANITU The MANITU [57] test facility has an ion source comparable to BATMAN, with a somewhat larger extraction area, and is dedicated to long pulse operation. In this facility, plasma and beam homogeneity in space and time are investigated. The capability to provide 3600(600) s $H^-(D^-)$ extraction on a mid-size extraction area of 190 cm^2 has been demonstrated using the same source dimensions as in BATMAN with current densities of 150(120) A/m^2 $H^-(D^-)$. This stable one-hour pulse operation showed that the RF-driven ion source concept is able to meet the ITER requirement for pulse duration. Still, values of extracted

negative ion current and electron to ion current ratio similar to BATMAN were obtained for shorter pulse lengths of several seconds.

The negative-ion source test facility MANITU is capable of running long pulses. This requires the replacement of the titanium getter pumps, used in BATMAN, by cryosorption pumps and the installation of cw[13] power supplies for the RF and high voltage system. The reduction and stabilization of the electron current, while maintaining a sufficiently high negative ion current, are the most critical issues for long pulse operation in order not to damage the extraction grid. The operational experience showed that the long-pulse stability is strongly correlated to the cesium conditions on the plasma grid. These are determined by the thickness of the cesium layers and by the temperatures of the source components during the plasma and the preceding vacuum phase. It remains an open question which parameters determine a long pulse stability.

RADI   The third facility RADI [58] is an intermediate step between the present small sources (BATMAN and MANITU) and the full-size ITER source. The aim is to try a multi-driver concept for sufficiently homogeneous illumination of the total grid area. Four BATMAN-like drivers are used, as shown in figure 3.9.

However, in this test facility, no extraction of negative ions is possible. The RADI test facility has no ion extraction system and the plasma grid is replaced by a slotted dummy grid with a gas conductance comparable to the ITER grid.

As a result of the successful development of RF sources for negative ion production and extraction at IPP, the ITER board has decided to adopt the IPP RF-driven ion source as the reference design for the negative-ion source of the ITER NBI [59]. To close the technological gap between the RF prototype sources and the full size ITER NBI source the new test facility ELISE is currently being built to develop and test a "half-size" negative ion RF source with long pulse operation and extraction.

ELISE   Although RADI will demonstrate the operation of a large RF source and the homogeneity of large RF plasmas, the results will have limited significance due to the absence of an extraction system. The extraction of the negative ions plays an important role for the transport of ions in front of the plasma grid and for the cesium dynamics. Therefore, IPP is presently constructing a new test facility ELISE[14] for the extraction of a half-size RF-driven ITER-like negative-ion source. Figure 3.10 shows ELISE compared to MANITU and to the ITER ion source.

An overview of the ELISE test facility is shown by the computer model in Figure 3.11. Figure 3.12 shows details of the ion source and the extraction system.

---

[13]cw: continuous wave

[14] ELISE: Extraction from a Large Ion Source Experiment, IPP Garching, Germany
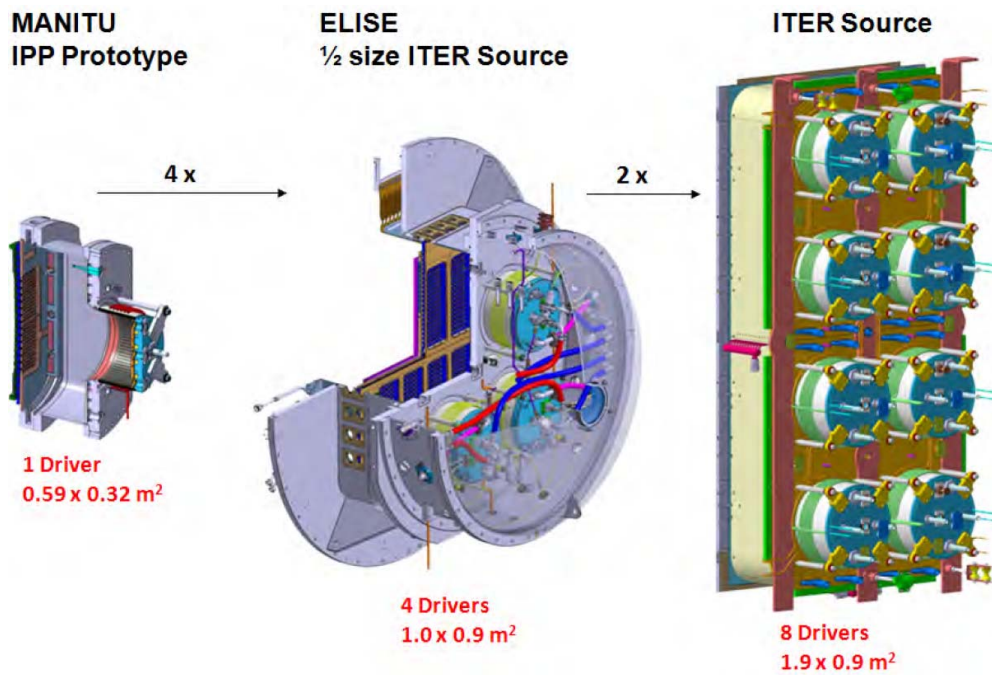
Figure 3.10: Comparison of the existing IPP prototype source of MANITU with the ion source for the future ELISE test facility and the negative-ion source planned for the ITER N-NBI.
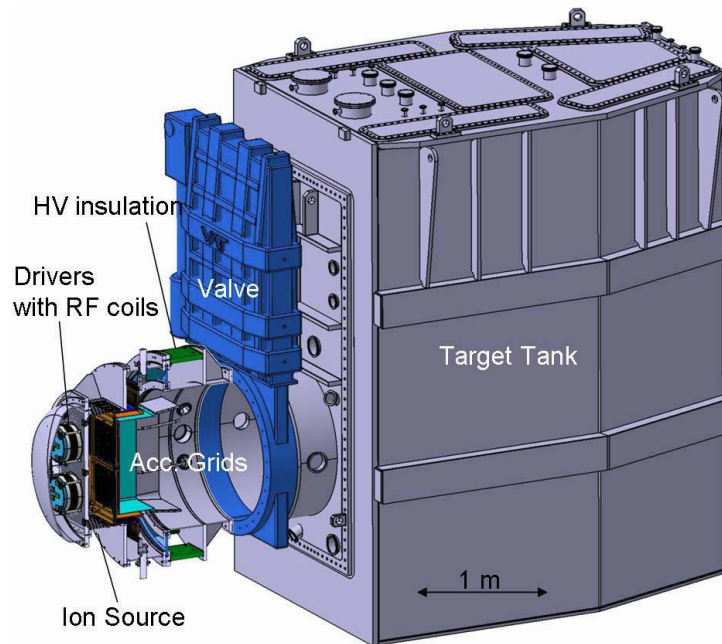
Figure 3.11: CAD drawing of the ELISE test facility

The design parameters are presented in table 3.2. Due to the limitations of the present IPP HV power supply, the extraction can be applied only for 10 s every 3 s; however, stationary plasma operation is foreseen. Tests on MANITU have shown that this simplification can be made with identical beam properties.

The source at high potential (60 kV) is separated from the ground potential of the tank and the calorimeter by a main insulator. Unlike the ITER source the ELISE source will be operated mainly in air to facilitate diagnostic access in the region near the plasma grid and to ease external modification of confinement and filter field. Therefore the whole source and extraction system has to be a leak tight vacuum containment capable to take loads applied by the air pressure. The drivers can be operated in air for easier access again or be put under a vacuum dome to simulate the ITER condition, e.g. the insulation of the RF coils.

The "half-size" extraction system of ELISE compared that of ITER and the ions source of BATMAN is shown in figure 3.13.

ITER test facilities The ITER heating neutral beam, as shown in figure 3.14, will be built at Consorzio RFX in the next years, in a close collaboration between European and Japanese associations [7]. This comprises the operation of two future
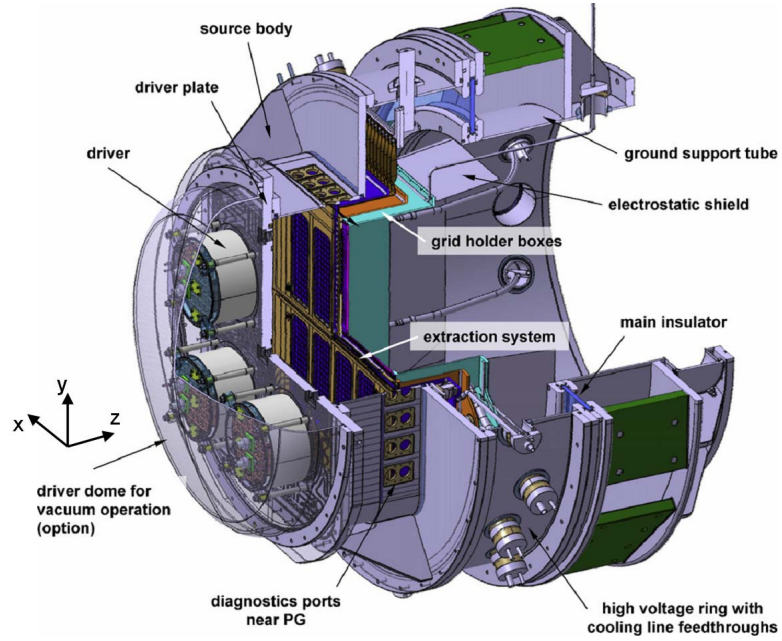
Figure 3.12: ELISE source with extraction system and HV insulation
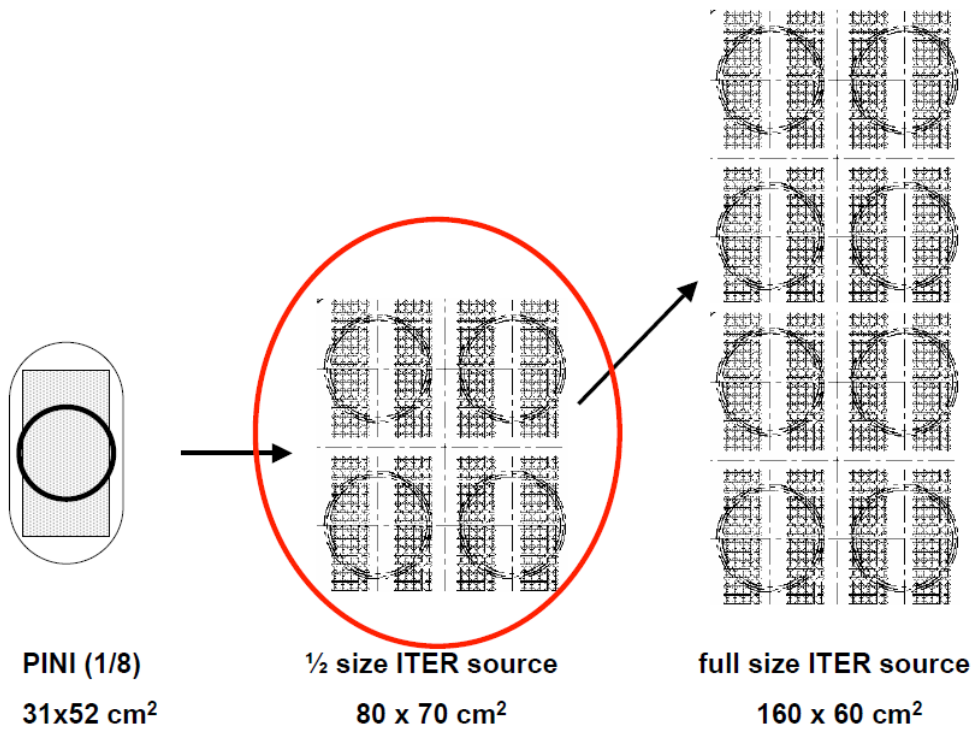
Figure 3.13: Comparison of different extraction systems
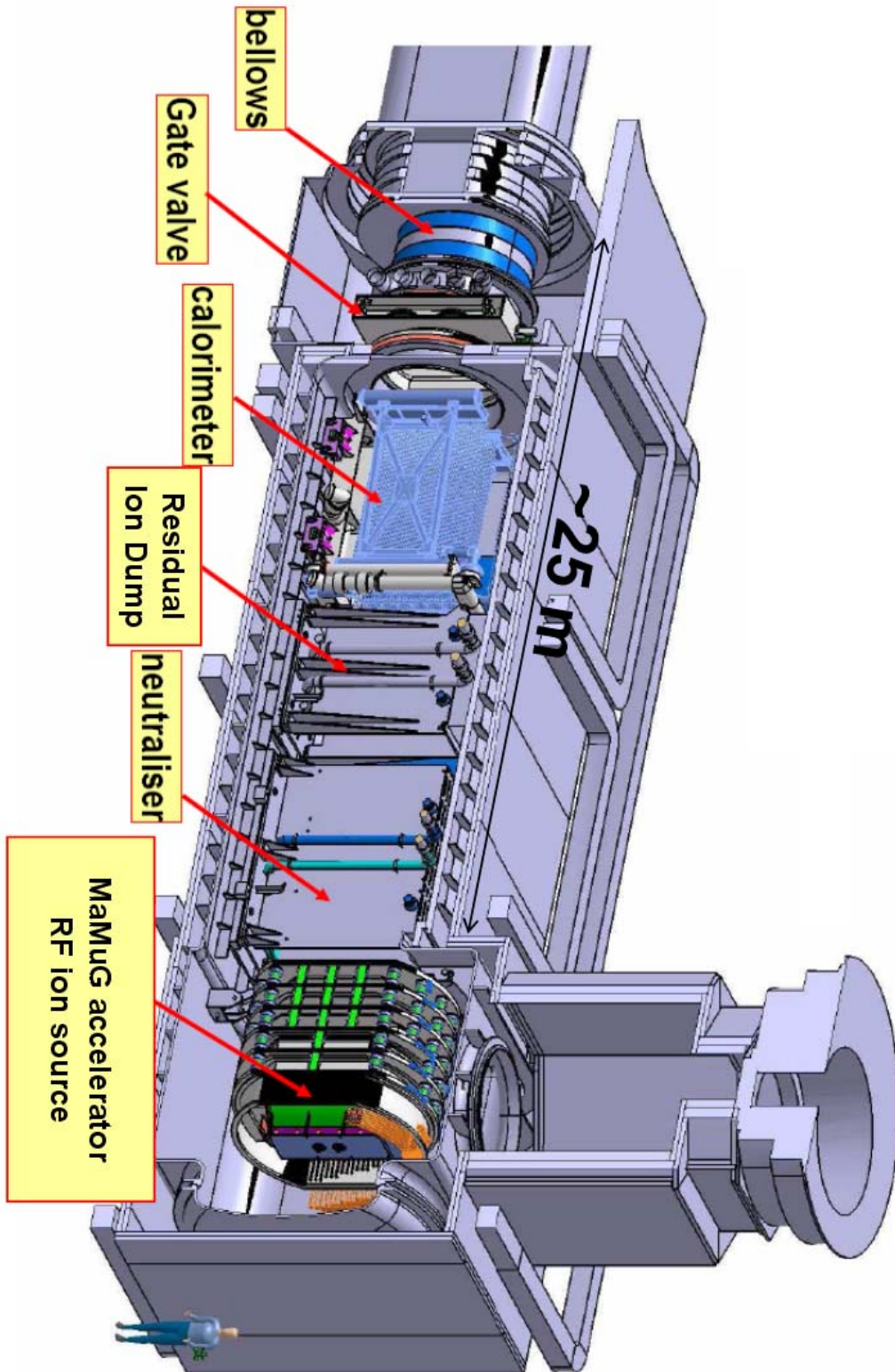
Figure 3.14: View of the ITER neutral beam injector
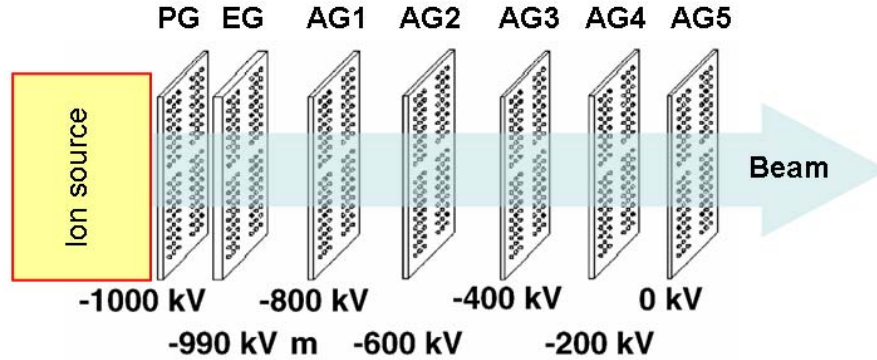
Figure 3.15: Schematic drawing of the MAMuG accelerator design, consisting of plasma grid (PG), extraction grid (EG) and 5 acceleration grids [7, 29].

neutral beam test facilities: SPIDER[15] [60] and MITICA.[16] [61] SPIDER will be an ion source test facility for 100 keV negative ion beams, while MITICA will be a 1:1 prototype of an ITER injector with a full 1 MeV beam line. The design of the RF-driven ion source has been adapted from IPP Garching. The Japanese MAMUG[17] design [62] is used for the acceleration system. This accelerator consists of plasma grid, extraction grid and 5 additional acceleration grids, forming 5 acceleration stages of 200 keV each, as illustrated by figure 3.15. The distances between the individual grids are typically between 50 mm and 90 mm.

3.5 Grids for the ELISE testbed

The extraction system of ELISE is a three grid system, plasma grid (PG), extraction grid (EG) and grounded grid (GG) each consisting of two identical segments arranged in a flat plane. The size of one grid segment is about the same as one of the four grid segments for the full ITER size. Additionally a so-called bias plate is installed in front of the PG with "window frame"-like openings around the beamlet groups.

The grid system accelerates the ion beam horizontally, in Z direction. The vertical direction is defined as Y direction and the horizontal direction parallel to the grids as the X direction (cf. figure 3.12).

The reference design for the aperture geometry of ELISE is based on the SIN-

---

[15]SPIDER: Source for the Production of Ion of Deuterium Extracted from Rf plasma, Test Facility, Padova, Italy

[16]MITICA: Megavolt ITer Injector & Concept Advancement, test facility, Padova, Italy

[17]MAMUG: Multi Aperture MUlti Gap design, Japan
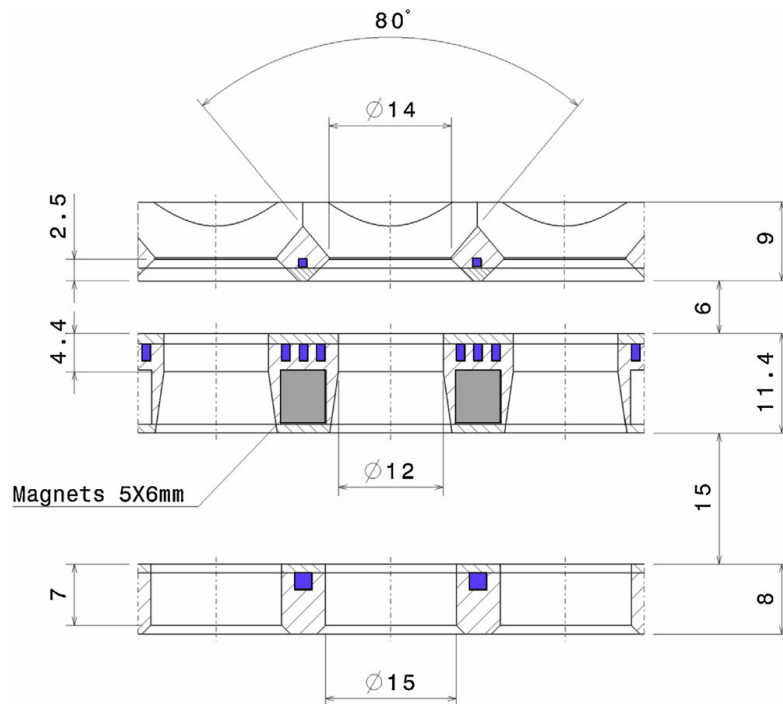
Figure 3.16: Aperture geometry of ELISE

GAP design for extraction and pre-acceleration, using $\oslash$ 14 mm apertures arranged in the same pattern (4 groups with 5×16 apertures per segment). The aperture spacing is 20 mm $\times$ 20 mm. An overview of the aperture geometry of all grids is presented in figure 3.16.

The plasma grid has been designed on the basis of the IPP experience with an 80° chamfer on the plasma side of the apertures. This increases the area for the conversion of neutral atoms and positive ions into negative ions in the region close to the apertures and allows for a more suitable starting angle for the negative ions [46].

The extraction grid and the grounded grid will be operated at 55°C (ITER reference value), while the plasma grid will be operated at $150 \pm 50°C$ to optimize the H$^-$ production rate.

All grids are mounted on grid holder boxes (cf. figure 4.3 in chapter 4) which are nested inside each other and immersed into the source body. This design enables an absolutely flat surface of the plasma grid and allows good diagnostic access from all sides just above the grid surface. The grid holder boxes are supported against each other by ceramic post insulators and mounted as a unit to the high voltage ring.

All grids will be manufactured by electro deposition of Cu onto a Cu base

plate with pre-machined cooling channels. This process has been developed and extensively used for positive ion systems for many years and allows sophisticated cooling channel designs with high reliability for leak tightness even with very small wall thicknesses of several tenths of millimeters.

The power load on the ELISE grounded grid has been estimated from the BATMAN and MANITU experience to be 10% of the total power. For ELISE this is 60 kW per grid segment. A cooling scheme similar to the plasma grid is foreseen to maintain the same advantages of low pressure drop and temperature uniformity.

In this study several aspects of the design for the PG and EG of ELISE have been analyzed and optimized as introduced in the next two subsections.

3.5.1 The plasma grid

The plasma grid is designed according to the RF source requirements (less power load). A vertical plasma grid current of up to 8 kA will be provided as well as an external permanent filter field. The design of the plasma grid is discussed more in detail in chapter 4.

The plasma grid of ELISE requires uniform temperature and operation at $150\pm 50°$C. This is achieved by means of a water circuit under 20 bar pressure. Due to the significant pressure load, mechanical stresses can be critical.

In addition a filter field is produced by means of a current of several kA flowing through the grid. The uniformity of the filter field depends on the current distribution inside the grid. This distribution is in turn strongly dependent on the plasma grid geometry. A uniform magnetic filter field is desirable to produce a uniform plasma inside the ion source. For the design of the plasma grid thermal, mechanical and electromagnetic fields must therefore be taken into account. In this thesis an optimized design of the plasma grid has been developed. This combines maximum $\pm 5°$C temperature non-uniformity, mechanical stresses lower than the allowable limit and uniform filter field in front of the extraction area.

3.5.2 The extraction grid

The extraction grid is loaded with the intense heat produced by the co-extracted electrons and is cooled by an embedded water circuit. The heat load on the extraction grid of ELISE typically has a peak power density of 40 MW/m^2. A more efficient cooling circuit is advantageous because it increases the reliability of the extraction grid both during normal operation and off design conditions. In this thesis an optimized design of the cooling circuit has been developed for the EG of ELISE to minimize grid temperature, mechanical stress and deformation. The design of the extraction grid is discussed more in detail in chapter 5.

3.6   Summary

In this chapter the principal characteristics of the NBI for ITER and in particular of negative-ion sources have been summarized and the present state of the research has been described, with emphasis on the testbeds at IPP. The relevant physical aspects of a negative-ion source have been discussed focusing on the phenomena involved in the design of the extraction system. The characteristics of the extraction system of the next large RF negative-ion source ELISE, in particular the requirements for plasma grid and extraction grid, have been introduced.

Chapter 4

Plasma grid

4.1 Introduction

Various engineering disciplines have to be taken into account for the design of the plasma grid of ELISE. The requirements of the ITER source have to be fulfilled taking into account the experimental evidence and the technical experience gained at IPP the experiments described in section 3.4.

In this chapter, the improvement of the design of the plasma grid of ELISE by means of several numerical tools is discussed in detail, with special emphasis on the analysis of the following aspects:

- electric current distribution

- temperature distribution

- magnetic field shape and strength

- mechanical stresses

The shape of the plasma grid determines the mentioned aspects simultaneously. Therefore, the analyses has been performed taking into account the interdependencies, as shown in figure 4.1.

The electromagnetic fields, temperature distribution and structural behavior are dependent on the grid geometry. The analyses have been performed sequentially and, if needed, the PG geometry has been modified with respect to the starting design. For all these aspects, the material properties play an important role, defining the component behavior and the requirements, e.g the allowable mechanical stresses. The process is repeated until the design criteria are satisfied.
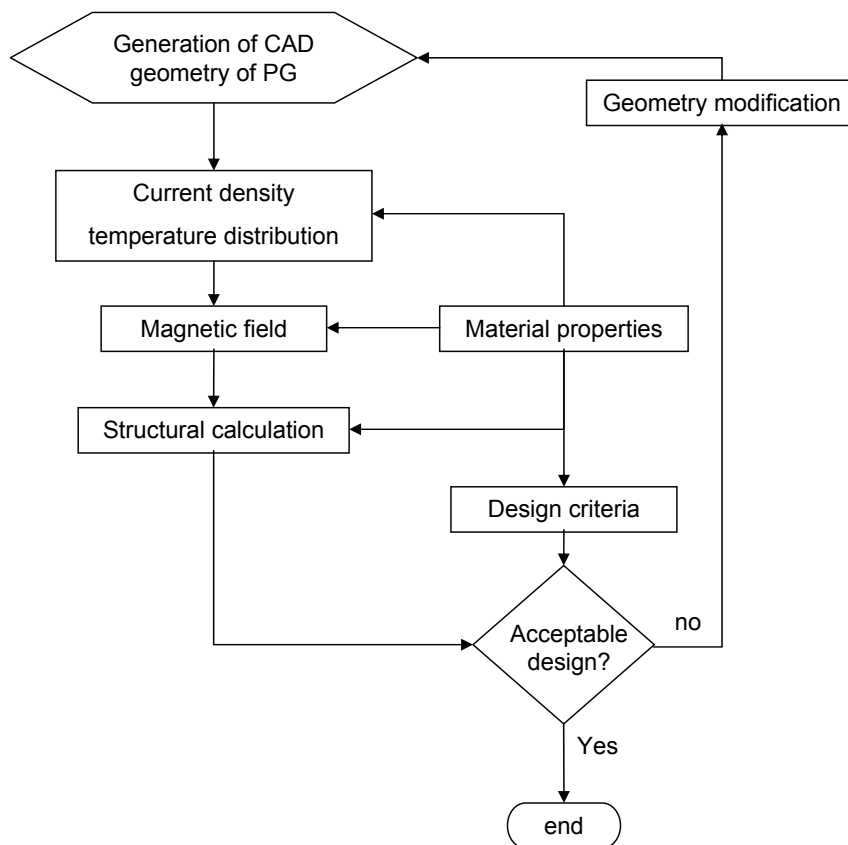
Figure 4.1: Flow diagram of design procedure for the plasma grid.
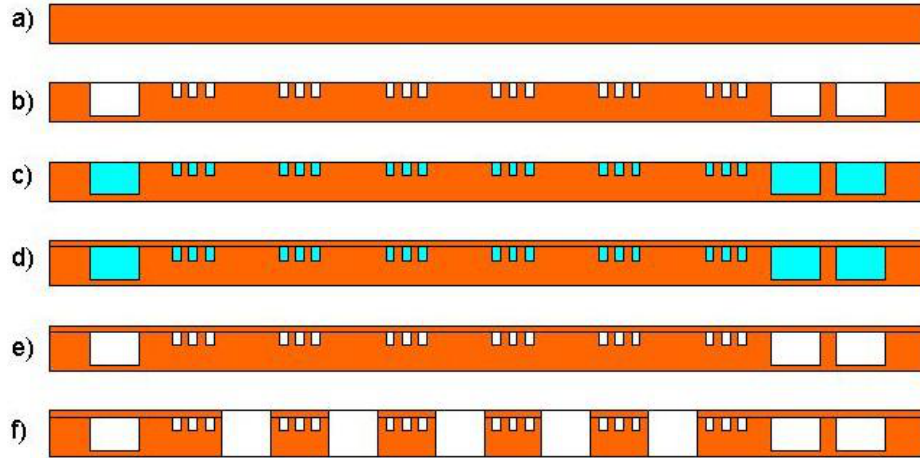
Figure 4.2: Scheme of manufacturing process for the extraction grids of ELISE.

4.2 The plasma grid of ELISE

The ELISE PG geometry is compatible with the ITER reference design for the negative-ion source [63]. The grid consists of two segments (four in ITER) made of copper. Each grid segment has 320 extraction apertures. In each segment the apertures are arranged in four groups of 5x16 beamlets, as shown in section 3.4 to match the sub-division of the beam line components in the ITER neutral beam injector. A complex internal water circuit is embedded inside the grid for temperature control. As for the grids of the NBI systems of JET and ASDEX-Upgrade, the manufacturing of the new PG design is possible by electro-deposition of copper. The process is explained in detail in figure 4.2. A copper ground plate (a) is milled to produce grooves for cooling channels and water manifolds (b). The channels are then filled with wax (c) and a layer of galvanic copper is deposited on the top side of the grid (d). The wax is then removed (e) by heating the grid. Finally the extraction apertures are milled (f).

The plasma grid will be PVD[1] coated with a $\approx 3\ \mu$m thick Molybdenum layer on the plasma side in order to obtain the optimum work function, as described in section 3.3.1.

As in ITER, ELISE uses a strong electric current, the plasma grid (PG) current, that flows vertically through the grid to generate the necessary magnetic filter field (FF). The plasma grid is attached to its support (a stainless steel grid holder box) in an electrically insulated way, so that the PG current does not flow into the grid holder box. The PG current is therefore concentrated entirely inside the plasma

---

[1]PVD: PHYSICAL VAPOR DEPOSITION. A method to deposit thin films by the condensation of a vaporized form of a material onto a surface
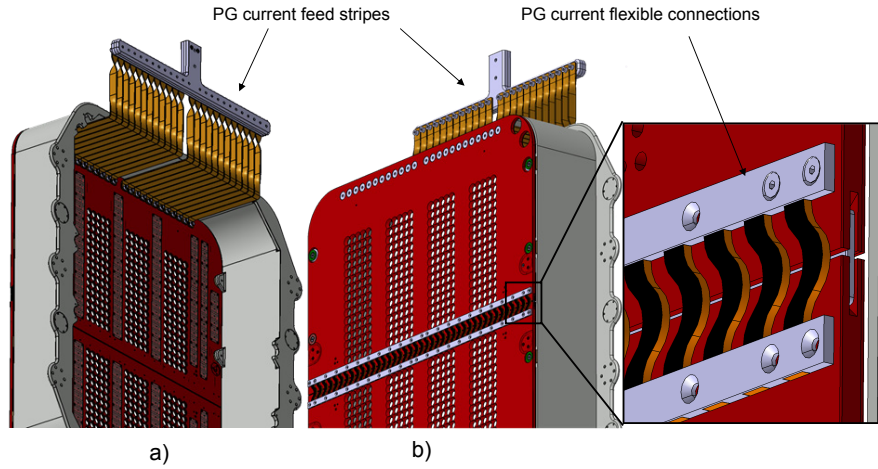
Figure 4.3: (a) Plasma grid current feed with 24 copper stripes attached to the back of the plasma grid and (b) flexible connections between the plasma grid segments. The grid holder box is shown in gray.

grid to achieve a higher magnetic field.

The PG current is fed by means of 24 copper stripes attached to the back of the plasma grid as shown in figure 4.3. For good Cesium conditioning, the plasma grid must be operated at $150 \pm 50\,°C$. Therefore, one end of these stripes is heated by contact with the plasma grid, the other end is cooled. The cross section of the current feed has been designed so that, when 8 kA of total PG current is applied to the 24 stripes, the hot end of current feed is ohmically heated to $140\,°C$, as shown in figure 4.4. In this way the interference with the temperature-control of the plasma grid, that must be maintained between $100°C$ and $200°C$, is minimized. When no PG current is required, the thermal losses are also limited due to the length and small cross-section of the copper stripes.

Copper has been preferred over stainless steel for its high electric conductivity to thermal conductivity ratio. Between the PG segments, 42 flexible connections, also shown in figure 4.3, carry the PG current and allow for 3 mm horizontal and 1 mm vertical displacement. The components are designed to allow up to 8 kA of total current. The filter field permanent magnets can possibly be installed such that they strengthen the magnetic field on the plasma side of the grid and weaken it on the beam side, visible in figure 4.5.

20		46.713		73.426		100.138		126.851	
	33.356		60.069		86.782		113.495		140.208
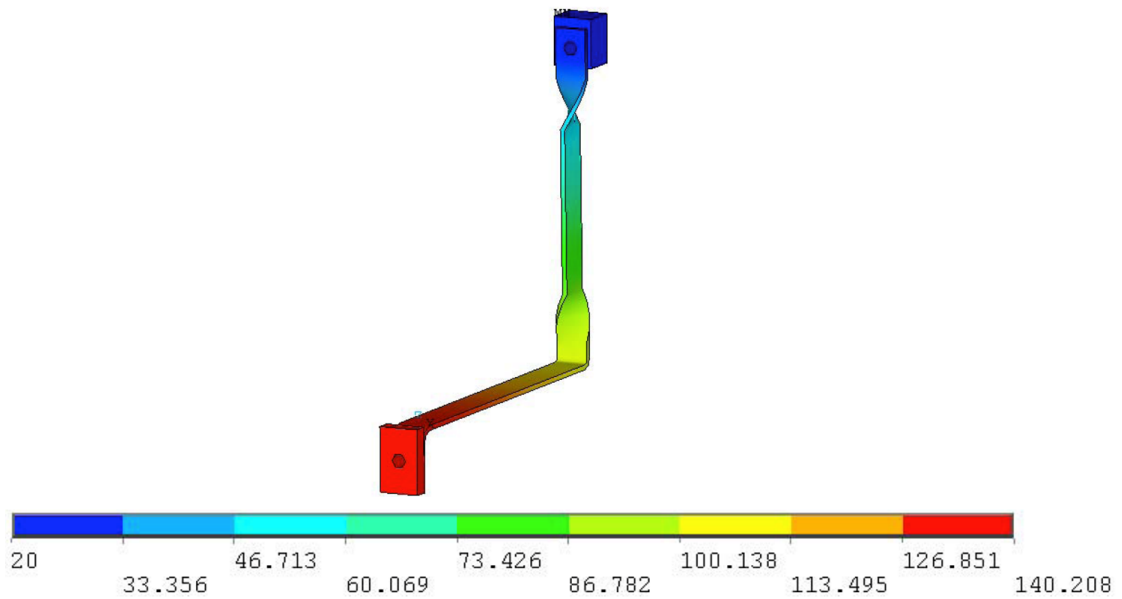
Figure 4.4: Temperature distribution in current feed when a PG current of (total) 8 kA is flowing in the 24 copper stripes.
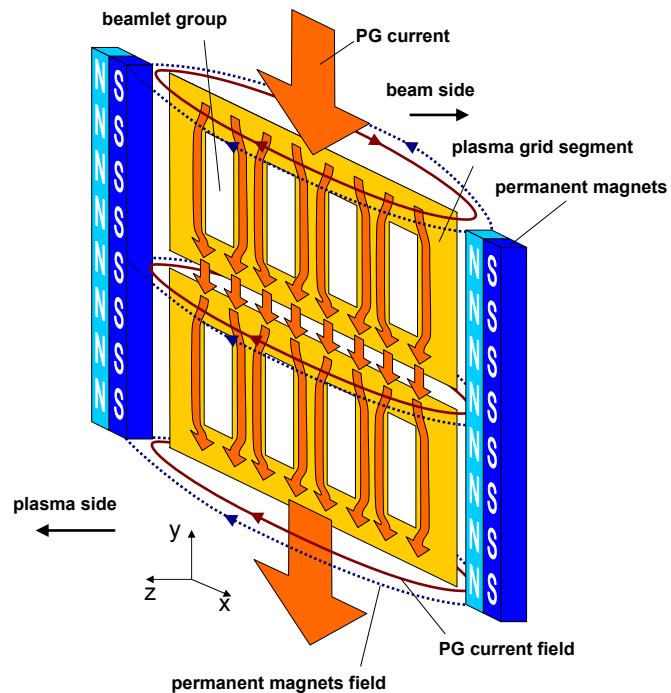
Figure 4.5: Scheme of magnetic filter field. Permanent magnets (blue) and PG current (orange) generate a magnetic field that add on the plasma side (left) and subtract on the beam side (right).
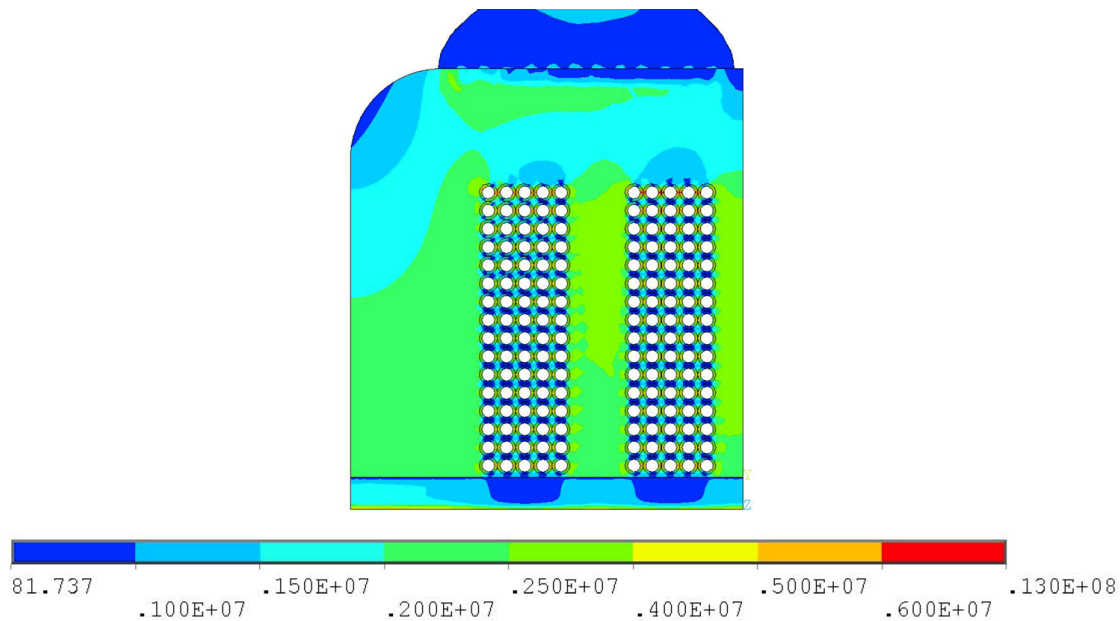
Figure 4.6: PG current density [A/m^2] distribution in the ITER plasma grid. The current density is high in between the beamlet groups due to the presence of the extraction apertures.

4.3   Filter field in the ITER reference design and in BATMAN

In the ITER reference design the plasma grid between the beamlet groups consists of a thick copper plate [63]. The beamlet groups narrow the current cross-section, thus increasing the electric resistances of the PG current, as shown in figure 4.6. As a result the PG current flows mainly in between the beamlet groups and on the sides of the grid.

By means of ANSYS FEM, the current density distribution in the PG has been evaluated. The results have been used to calculate the magnetic filter field. The BATMAN experiment [46] configuration (permanent magnets only) has also been calculated and compared with the ITER reference solution: 4 kA DC PG current plus 30×20 mm^2 Sm$_2$Co$_{17}$ permanent magnets on the sides of the source, originally developed for the arc-driven source [63].

Two main parameters have been considered in this analysis, which are important for the operation of the source. One is the B_x, horizontal component of the magnetic field (cf. figure 4.5), calculated at different distances with respect to the PG on the plasma side. The second is the $\int B_x dL$, integral of B_x calculated along a line perpendicular to the PG, in its center, in Z direction. In the RF source fast

electrons come from the drivers, so the $\int B_x dL$ is calculated between the PG and the ion source back plate, positioned at 220 mm from the PG. Figure 4.7a and 4.8 show the results of the simulations for the following 4 cases:

- BATMAN ion source:

  - only Sm_2Co_{17} permanent magnets of 39×18 mm^2 section (standard configuration, as this is the experimental reference).

- ELISE ions source:

  - Only with Sm_2Co_{17} permanent magnets of 30×20 mm^2 section.
  - with 4 kA PG current and 30×20 mm^2 section Sm_2Co_{17} magnets along the sides.
  - with 8 kA PG current and 30×20 mm^2 section Sm_2Co_{17} magnets.

From this preliminary study, these considerations arise :

- Absolute B_x value of the BATMAN FF is significantly higher than in ITER reference FF.

- The $\int B_x dL$ calculated for an ITER-like RF source is much lower than the $\int B_x dL$ for the BATMAN source. This is due to the fact that the width of the BATMAN source is much smaller than in an ITER-like source and therefore, the permanent magnets are positioned closer to each other.

- As expected, the magnetic field at 2 mm from the PG surface, on the plasma side, is considerably non-uniformity. Two kinds of "ripple" can be identified. The small ripple is due to the single apertures, where current can flow only on metal parts around the holes. A big ripple is then due to the fact that the current flows preferentially between the beamlet groups, where the grid is thick and no big electrical resistance is present, as shown in 4.7a. This non-uniformity on the magnetic filter field is still present at 20 mm from the PG surface, as shown in figure 4.7b, while the small ripple disappeared.
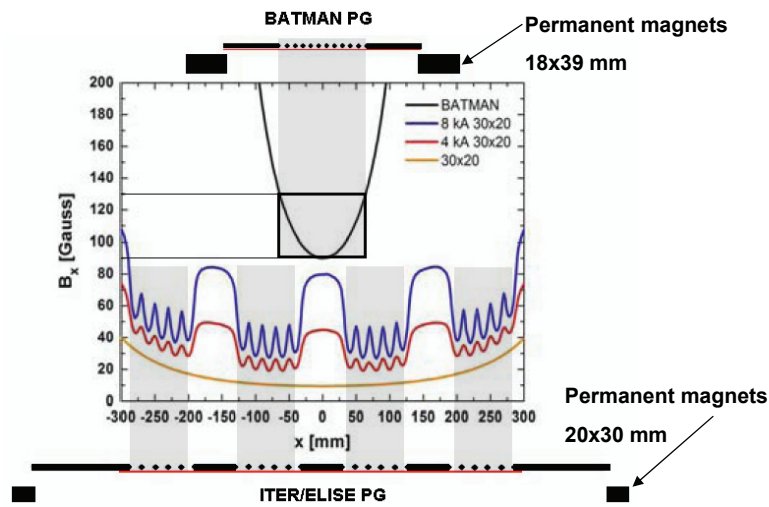
(a) "Ripple" of the B_x component of the FF across the extraction area of ELISE for different combinations of plasma grid current and permanent magnets in a distance of 2 mm from the plasma grid. Aperture positions indicated above and below graphs and by gray shading. For comparison, the B_x field of BATMAN is plotted in the figure.
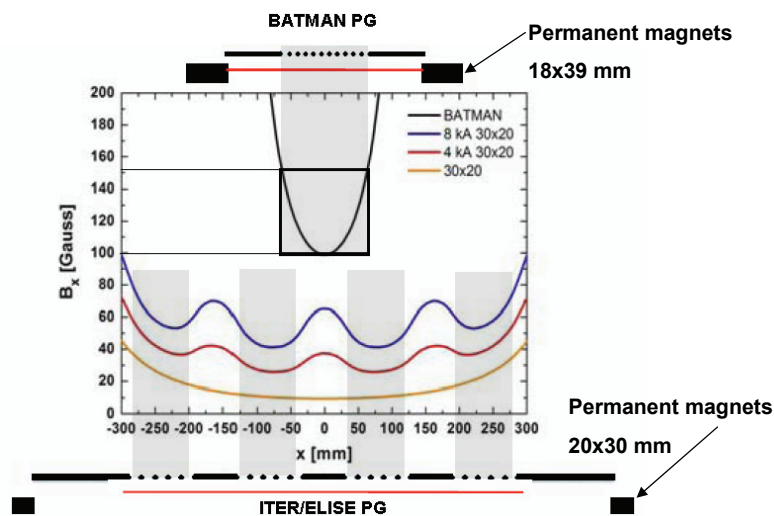
(b) "Ripple" of the B_x component of the FF across the extraction area of ELISE for different combinations of plasma grid current and permanent magnets 20 mm from the plasma grid.

Figure 4.7: Comparison between different filter field configurations at 2 and 20 mm distance from the plasma grid
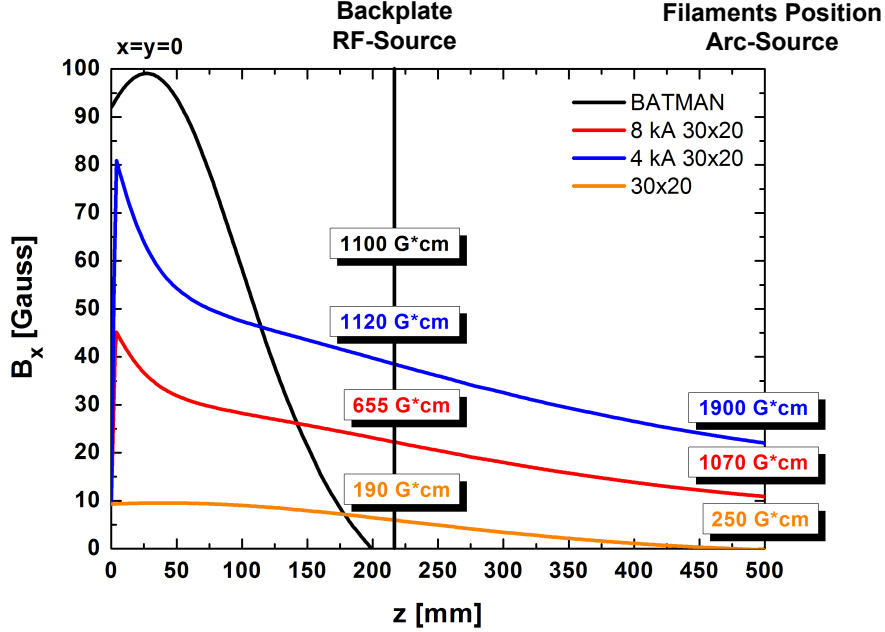
Figure 4.8: B_x filter field component for different combinations of permanent magnets and plasma grid current. (black: BATMAN, red: ITER-like source with 8 kA PG current and permanent magnets, blue: ITER-like source with 4 kA PG current and permanent magnets, yellow: permanent magnets only).

The filter field of the ITER reference design differs considerably from the BATMAN FF, mainly due to the different size of the sources. The $\int B_x dL$ values shown in Figure 4.8 are calculated for the various configurations with respect to the fast electron source, the driver region of the RF source.

The $\int B_x dL$ of the FF could be increased in ITER by raising the PG current, but this produces a higher field also in the accelerator region causing undesired deflection of accelerated ions and high power loads on the accelerator grids. In addition, the ripples and non-uniformity of FF are increased. Up to now it is not clear which FF strength is necessary for a large RF source like ELISE, but it can be expected that a non-uniform FF with these large ripples affects the beam homogeneity. Therefore, an intense research effort has been dedicated to reduce the FF non-homogeneity in ELISE.

In addition, to the filter field the electron suppression magnets embedded in the EG produce the Electron Deflection magnetic Field (EDF) for the deflection of the co-extracted electrons. The EDF penetrates into the source and super-imposes with the filter field. The experience acquired at IPP suggests that the EDF influences drastically the plasma source performance [46]. The analysis of the superimposition of FF and EDF is shown in section 4.5.

4.4 Plasma grid geometry for optimized magnetic filter field

The proposed solution for ELISE is to change the PG geometry such that the resulting current distribution reduces the non-uniformity in the FF and generates a higher magnetic field in the central part of the PG with the same current. The PG geometry has been iteratively changed and optimized using ANSYS FEM code. A typical section of the ELISE PG has also been modeled. The analyses consist of two steps:

- An electric-thermal model of the grid has been created in ANSYS to calculate the temperature field and the electric current density distribution in the PG. The following loads and boundary conditions have been taken into account:

  - Ohmic heating, caused by the PG current
  - Heat load from plasma: 20 kW/m^2
  - Temperature control:
    * water at 150 °C
    * convection coefficient $\alpha = 30000$ W/m^{2}K (cf. section 5.3.1).

- Permanent magnets and the region around the PG have been modeled in ANSYS with magnetic elements and the current density distribution has been imported from the electric model described above.

Improvements in the FF uniformity have been obtained by increasing the ohmic resistance of the areas between the beamlet groups and along the grid sides. This was achieved by changing the shape of the vertical manifolds of the cooling circuit of the PG and introducing pockets in the regions between the beamlet groups and on the sides of the PG, visible in figure 4.9. In addition, ribs have been introduced in the downstream side of the PG. This increases considerably the mechanical stiffness in the areas between the beamlet groups and on the sides of the PG without reducing significantly the electrical resistance. This design also gives the possibility to insert magnets in the pockets in a later stage of the experiment to test different FF configurations.

The result of the magnetic field calculations is shown in figure 4.10. It can be seen that the small ripple caused by the apertures is still present and cannot be reduced due to the presence of the extraction apertures, but the big ripple has been reduced significantly and almost disappears at 20 mm from the PG. In the new plasma grid design, the current flowing in the apertures region is higher by 50% because more current is flowing in the center of the PG than in the previous

design. Accordingly, the magnetic field in front of the PG is larger for the same total current. The minimum value of the magnetic field in front of the PG is increased by 50% and the big ripples in the magnetic field at 2 mm from the surface have been reduced. The non-uniformity in the FF almost disappears at 20 mm from the PG surface.

The $\int B_x dL$ has been calculated along different lines perpendicular to the PG, both in the reference and in the new design. It can be seen that the new design produces a more uniform $\int B_x dL$ distribution. In addition, it is slightly higher in front of the extraction areas, as visible in figure 4.11.

4.5 Electron deflection field (EDF) configurations

In ELISE, it is possible to align the EDF both in horizontal and vertical direction, enabling investigations of the source performance, i.e. extracted negative ion and co-extracted electron currents, for both cases. In the first part of this chapter, the role of the EDF has not been taken into account. In this section the interaction of these magnets with the FF has been investigated as follows.

Two possible configurations have been considered (cf. chapter 5). In the first one the electron suppression magnets are oriented as dipoles in vertical rows between the apertures so that the EDF is parallel to the FF, alternating in horizontal direction. This will be called "parallel" orientation. This field is therefore, on the plasma side of the plasma grid, either adding or subtracting to the component B_x of the filter field. The second configuration consists of suppression magnets oriented as dipoles horizontally generating an EDF "orthogonal" to the FF. This option has been used in the BATMAN experiment and other experiments worldwide so far.

As at the beginning of the design phase of ELISE it was not clear whether the orthogonal configuration was suitable for ITER, the EG of ELISE was designed for both orientation to test the difference between the two configurations experimentally. Besides the effect on the filter field, the electron deflection is obviously dependent on the orientation of the EDF, resulting in an impinging electron footprint turned by 90°, which will be described in chapter 5.

The parallel and orthogonal configurations have been investigated with AN-SYS, the results are shown in figure 4.12. It can be seen that in parallel orientation, the EDF and FF are alternatively added and subtracted for each aperture column to the FF. This creates zero-field regions once every two apertures, and could lead to a strong non-uniformity in filtering the electrons and is potentially dangerous. In fact, even if the overall power deposition on the EG is within the operational range, there could be a very localized heat load in correspondence to the apertures where the electron leakage is higher, leading to a localized melting

of the EG (cf. chapter 5).

On the contrary, the orthogonal orientation of the EDF and FF generates a much more uniform magnetic field in front of the PG. Small magnetic field distortions due to gaps without magnets are visible from the FF calculation, but they can be considered acceptable in terms of FF homogeneity.

As a result, it was concluded to start ELISE with the EDF in orthogonal orientation to the FF for safe operation. Also, ITER has meanwhile adopted the orthogonal configuration as the reference design .

4.6   Mechanical analysis

After the improvement of the PG design with respect to the magnetic FF homogeneity, the following step is the mechanical verification. It is evident that by introducing the vertical manifolds and the pockets in the PG, a large amount of material has been removed. Therefore, the structural stability of the plasma grid must be assessed given the high pressure inside the cooling channels.

4.6.1   PG cooling circuit

The cooling circuit of the plasma grid for ELISE has to be designed taking into account the following loading conditions:

- The power load on the plasma grid for RF sources, that has been estimated from BATMAN experiments to be 20 kW/m^2.

- The ohmic heating from the PG current, relatively low, accounting for 2 kW per segment.

- The plasma grid will be operated at temperatures up to 200°C. Therefore, its temperature will be actively controlled by a dedicated PG cooling system with pressurized water at 20 bar (outlet counter pressure).

In the proposed ITER-design the cooling water flows through the entire width of the grid from the inlet on one side to the outlet on the opposite side. For ELISE, it was tried to reduce the temperature gradient within the grid and therefore minimize the distortion of the grid. A complex cooling geometry has been designed as shown in figure 4.13. Two comb like manifolds, one each for inlet and outlet, are placed between the beamlet groups. Small channels between each aperture row connect these inlet and outlet sub-manifolds and heat the grid only in that small area of 5 apertures. In this way the temperature can be kept more homogeneous over the whole plate and consequently creating less deformation, especially the

Table 4.1: Cooling parameters for the plasma grid of ELISE

Total water flow	0.2 l/s
Inlet water temp	$150 \pm 50°C$
Counter pressure outlet	20 bar
Pressure drop	< 1 bar
Max. water velocity	3 m/s
ΔT Water/Grid	10/15 K

out of plane bowing. Due to the small distance between grids, for instance 6 mm between plasma grid and extraction grid, deformations are especially important for their influence on the ion beam optics [64].

The parameters of the cooling circuit are given in table 4.1. The maximum temperature difference along the grid surface has been calculated to be less than 16 K. This will be sufficient for a homogeneous Cesium coverage as MANITU experiments indicate.

4.6.2 Structural analysis

Although the electro-deposition method has been used for NBI grid systems for many years, the mechanical properties of electro-deposited copper were not systematically evaluated. In order to optimize the magnetic filter field the current flowing in some parts of the plasma grid had to be reduced. This was achieved by reducing the wall thickness of the water manifolds to a minimum, but still guaranteeing a grid design capable to withstand the internal pressure of the cooling circuit at temperatures up to 200°C. Therefore, a comprehensive test campaign has been performed to evaluate the material properties of electro-deposited copper, as described in the appendix A.

Based on the material properties determined in the test campaign different load cases have to be considered for the structural analysis of the three grids of the extraction system. The extraction grids are operated at different pressures, as listed in Table 4.2, according to the requirements of pressure drop and downstream pressure of each grid. For instance, the plasma grid requires 20 bar downstream pressure to avoid boiling of water at 200°C. The pressure drop due to water flow is lower than 1 bar, because of the low water velocity. Thus, 20 bar is the operating pressure for the plasma grid. All the grids are tested at room temperature (RT) with a factor of safety of 1.48, according to the pressure vessel regulations. Therefore, the test pressure is defined as the operating pressure times 1.48, i.e. 30 bar for the plasma grid.

Table 4.2: Operating and testing parameters of grids

Grid	T_{test} [°C]	T_{oper} [°C]	P_{test} [bar]	P_{oper} [bar]
PG	20	200	30	20
EG	20	55	25	16
GG	20	55	16	10

The calculations for mechanical stresses in the grids are all performed at the test pressure load by means of linear elastic models. This assumption is realistic if the stresses in the model do not exceed the material yield strength. One can however assume that very localized stresses can be tolerated even if they exceed the material yield strength in test conditions because the material will experience a one-time localized plastic deformation that will have the effect of relaxing the stress peaks but will not lead to a failure of the component. It is the analyst judgment to determine if the mechanical stress in a component is acceptable and to decide how the geometry should be modified to reduce the risk of failure.

Stresses in the elastic range scale linearly with the applied pressure and one can assume that during tests, the stresses will be larger by a factor of 1.48 than during operation conditions.

The components will be subject to number of load cycles smaller than 10000. Therefore, it is sufficient to keep the maximum mechanical stresses lower than the yield strength of the material to avoid low cycle fatigue. For the plasma grid the allowable stress is defined as the yield strength of the material at 200°C that was found to be 140 MPa. For the extraction and grounded grid, the allowable stress is the yield strength of the material at room temperature (20°C, 200 MPa).

At room temperature, the values of the maximum allowable stress (shown in table A.1) are near to the yield strength of the material for EG and GG while there is a safety coefficient of 1.49 for the PG (table 4.3). At operating conditions temperatures will be higher, especially for the PG, and pressures will be lower. Scaling the maximum allowable stresses for each grid according to the reduced applied pressure and comparing these results with the yield strength of the material at operating temperature results in a safety factor during operating condition for each grid, as reported in table 4.3.

4.6.3   FEM models

Due to the complex geometry of the plasma grid and in particular the high ratio between grid size and smaller edge dimension, an accurate FE analysis would require to mesh the grid geometry with a very large number of nodes and elements. In order to limit calculation time, but not the accuracy of the FEM calculations, the most critical areas of the grid have been identified by a global model and

Table 4.3: Summary of material yield strength and safety coefficients for different grids and load conditions. σ_y: yield strength, σ_{all}: allowable stress, T_{test}: room temperature, T_{oper}: operating temperature, FS: factor of safety

Grid	σ_y [MPa]		FS		σ_{all} [MPa]	
	T_{test}	T_{oper}	T_{test}	T_{oper}	T_{test}	T_{oper}
PG	209	144	1.49	1.54	140	93
EG	209	205	1.05	1.60	200	128
GG	209	205	1.05	1.64	200	125

analyzed by local models with fine mesh size. Four areas, shown in figure 4.14, corresponding to manifold T-junctions of the water circuit and the metal insert at the inlet/outlet of the grid, have been chosen, assuming that the wider local section of the water channel leads to larger deformations and mechanical stresses.

Only one of the mentioned critical areas will be discussed here (figure 4.14). The mesh of the FEM model, is shown in figure 4.15. A uniform mesh is generated with a typical dimension of the elements of 1 mm.

Boundary conditions are defined as shown in figure 4.16. These comprise an internal pressure load of 30 bar on the inner surface, as used in the testing, and appropriate supports and surface constraints to allow proper expansion of the grid model.

The first evaluation of the Von Mises stresses shows how stresses are concentrated in the inside of the cooling channel and in particular in the edge of the T-junction. The value of 158 MPa is found, which is higher than 140 MPa (the maximum allowable stress at RT, as defined in table 4.3). Therefore, a modification of the design is necessary.

As a consequence, the thickness of the lower manifold wall has been increased from 1 to 1.2 mm. The evaluation has been repeated and, as shown in figure 4.17, maximum Von Mises stress is reduced to 133 MPa, an acceptable level according to the criteria discussed in section 4.6.2.

The geometrical modification of the plasma grid affects the PG current distribution. The extent of this modification has been evaluated in a subsequent analysis similar do the one described in section 4.4, which has shown no relevant change in the FF uniformity.

4.7 Results

The plasma grid geometry has been optimized using electro-magnetic analyses shown in section 4.4 and mechanical evaluations described in section 4.6. The new design results in:

- A 50% increase in magnetic field in front of the grid

- Acceptable FF uniformity considering the shape of the B_x profile over the grid width at various distances from the PG.

- Mechanical stresses lower than the allowable stresses

4.8   Summary and further improvements

As an example for a design improvement taking account several requirements at the same time, the design of the plasma grid of ELISE has been analyzed. The new PG design developed for ELISE offers a significant improvement of the FF homogeneity and FF strength in front of the PG both measured as B_x and $\int B_x dL$, for equal PG current intensity, with respect to the ITER reference design.

In ITER, the PG current is limited to 4 kA. In fact the PG current produces a strong magnetic field also in the accelerator, bending the trajectories of the extracted negative ions and therefore disturbing the beam generation.

In ELISE the FF intensity in front of the PG and the the $\int B_x dL$, with 4 kA of PG current, is still lower than the BATMAN FF configuration taken into account in this study.

Several design solution that produce a strong and uniform FF in the plasma source and a low or no magnetic field in the accelerator are presently under discussion.

The plasma grid design described in this chapter represents an acceptable solution for the ELISE ion source. Mockups of the plasma grid for ELISE have already been manufactured and tested successfully. However, a further improvement in the design of the plasma grid is possible if a formal optimization procedure is applied. Due to the multidisciplinarity of the problem, an MDO approach has been adopted and is discussed more in detail in chapter 7.

Cooling circuit manifolds

a)

b)

Pockets are covered by a
steel plate
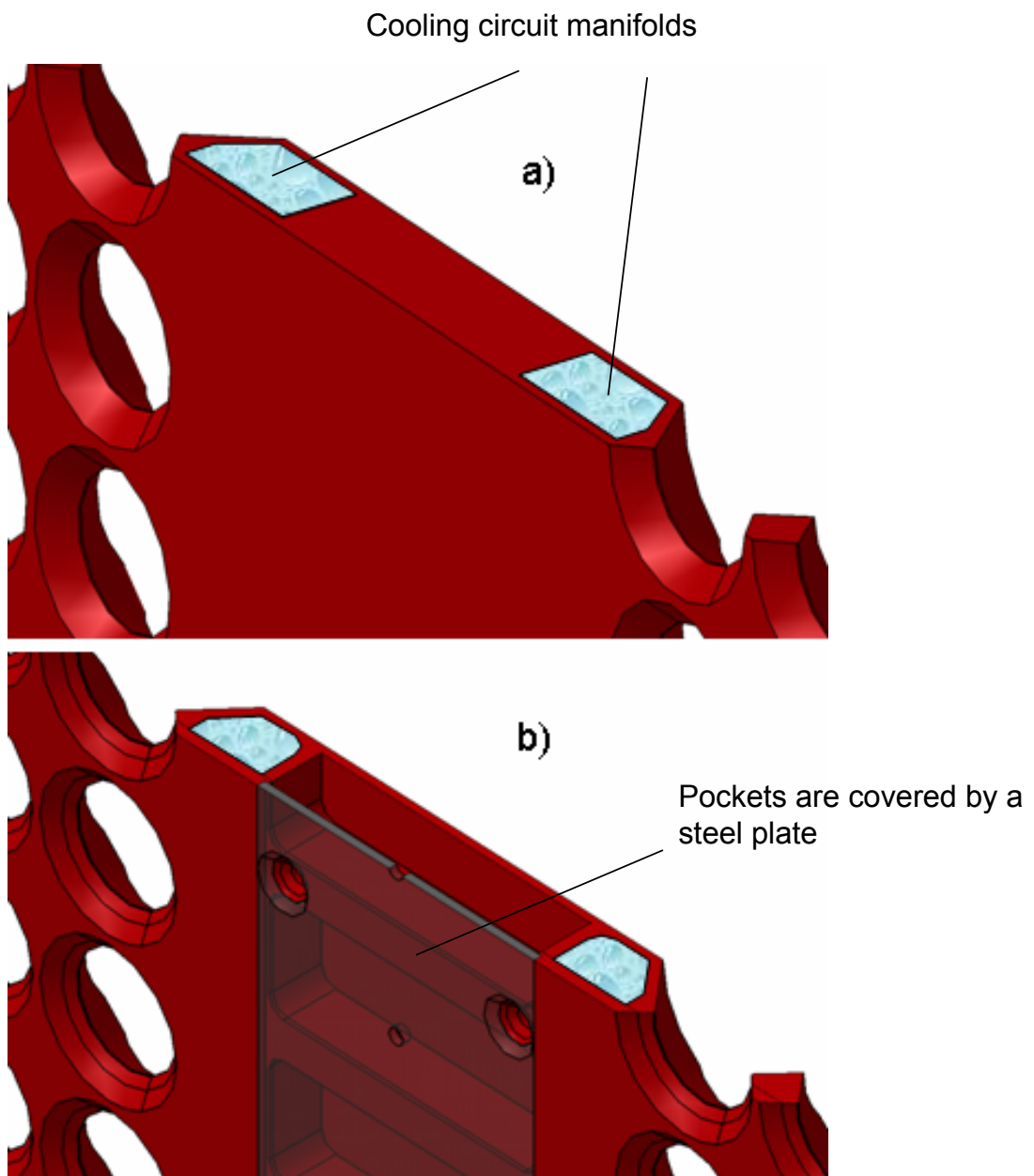
Figure 4.9: Section of different types of PG design. (a) Similar to the ITER reference
PG. (b): ELISE PG with pockets to reduce the electric conduction between the apertures.
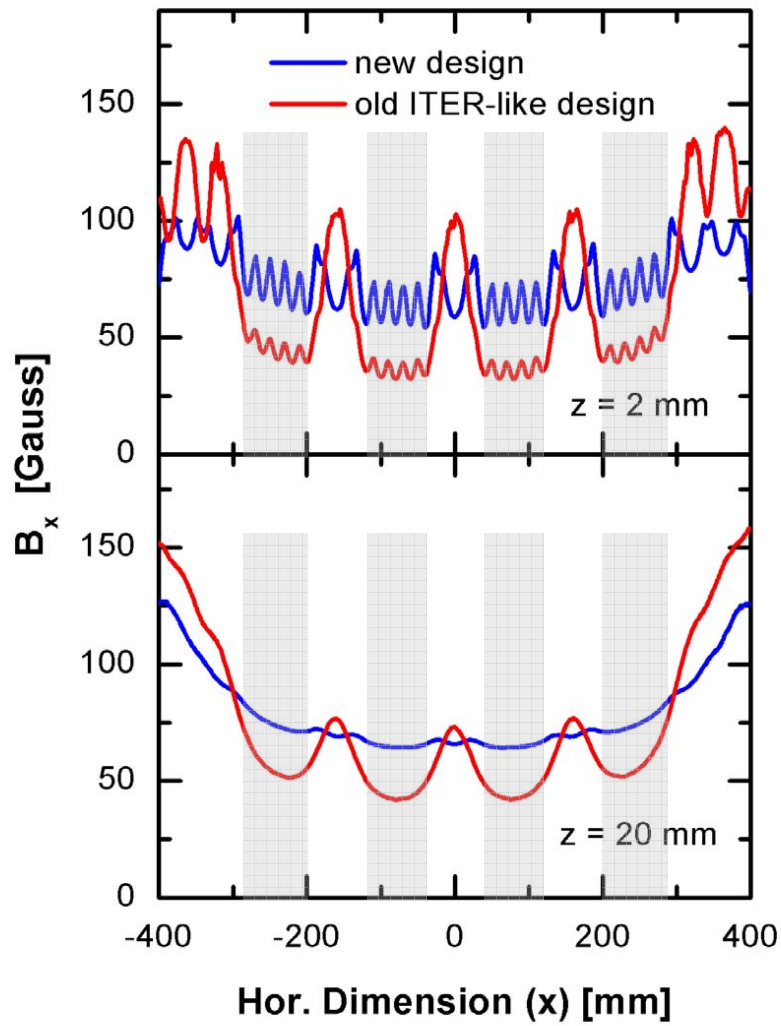
Figure 4.10: Filter field distribution across the extraction area of ELISE for the old and new plasma grid geometry in a distance of 2 mm and 20 mm from the plasma grid for 8 kA current and permanent magnets.
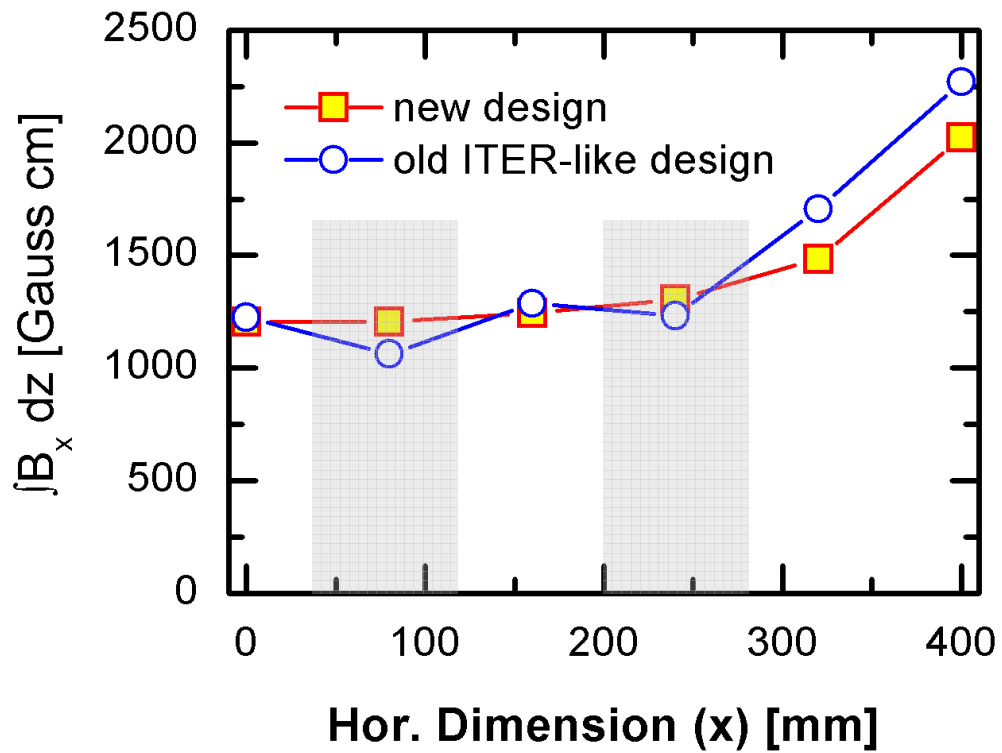
Figure 4.11: $\int B_x dL$ calculated for the x component (horizontal dimension) of the magnetic field at the center of the beamlet groups and in between the beamlet groups for 8 kA current and permanent magnets (20×30 mm). The beamlet groups are indicated in gray.
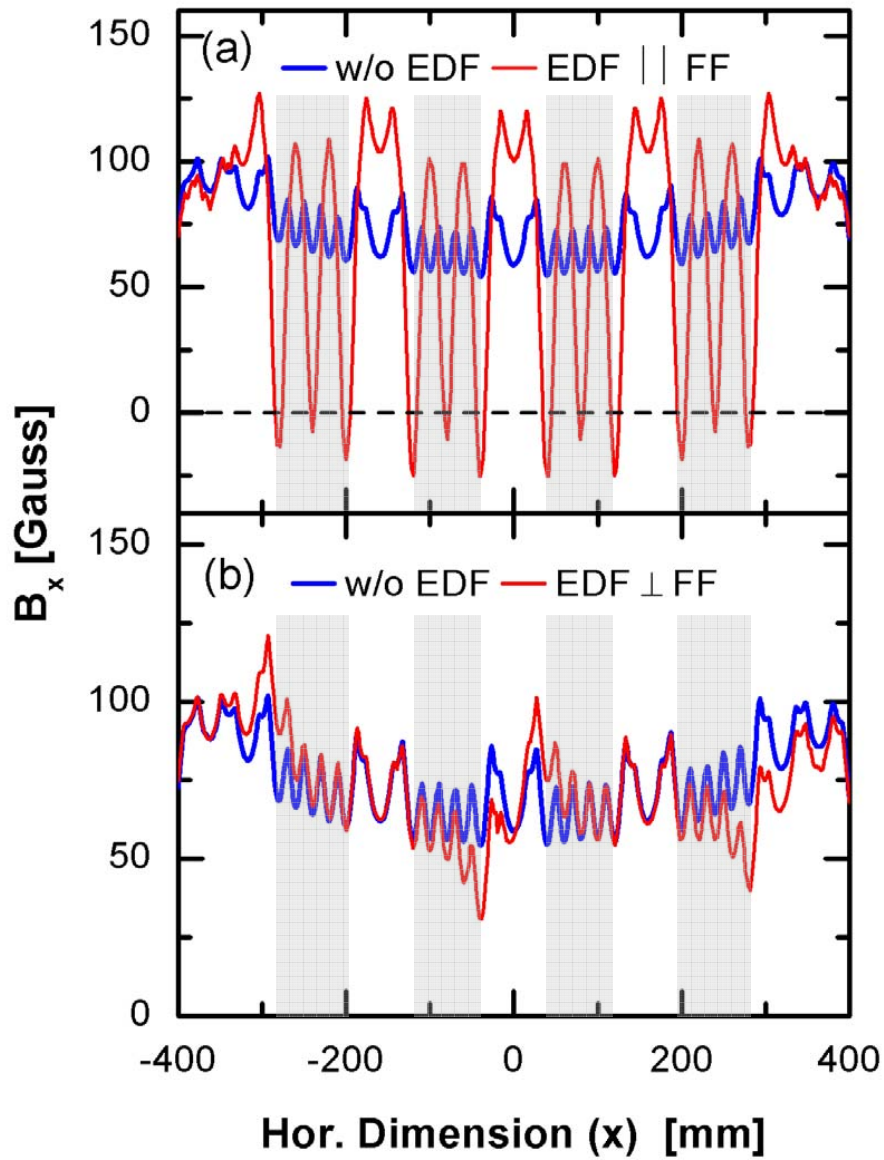
Figure 4.12: Effect of orientation of the electron deflection field (EDF) on the B_x component calculated at a distance of 2 mm from the plasma grid for 8 kA current and permanent magnets. (a) Parallel configuration (vertical magnets). (b) Orthogonal configuration (horizontal magnets). Blue graph without EDF, red with EDF.
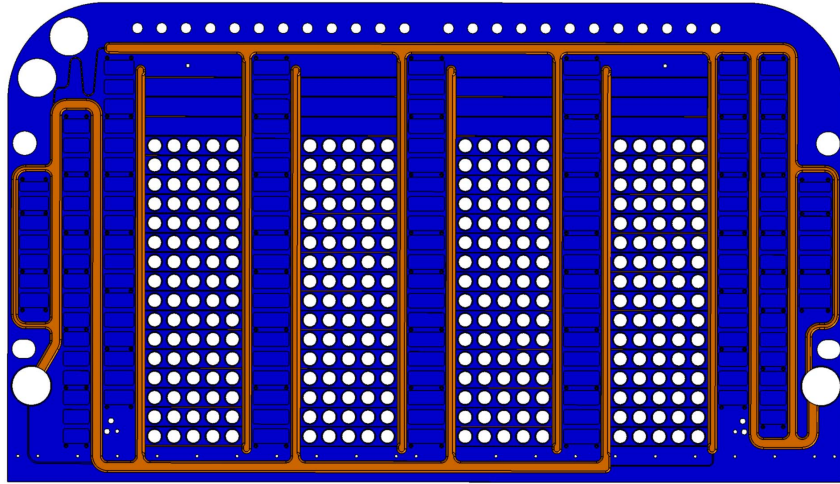
Figure 4.13: Plasma grid cooling scheme. The long arrows show the water flow direction, the short arrows indicate the expansion direction of the grid. On grid segment is fixed in on one position and has a slot for lateral expansion on the opposite side. The upper positions are designed for free expansion in all directions.
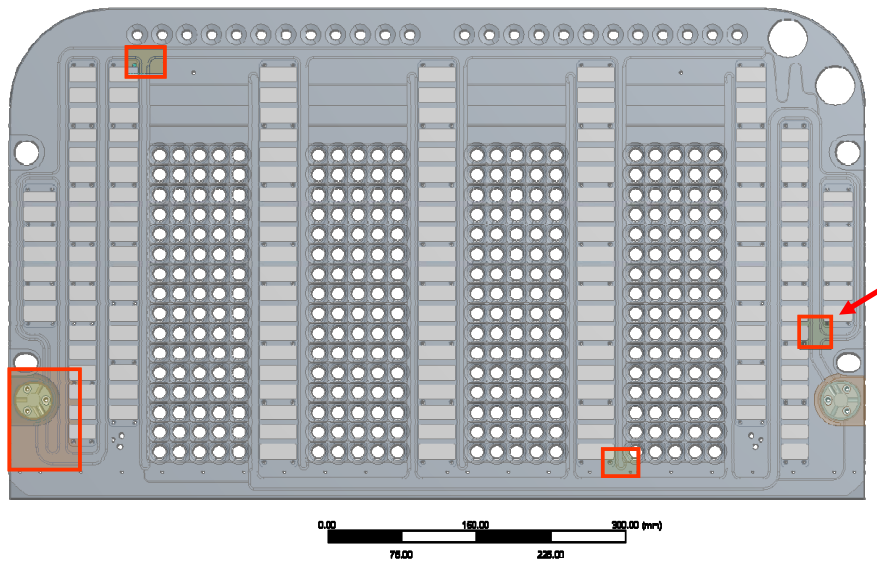
Figure 4.14: Plasma grid model. Critical areas for mechanical stresses are highlighted. The arrow points to the region discussed in this work.
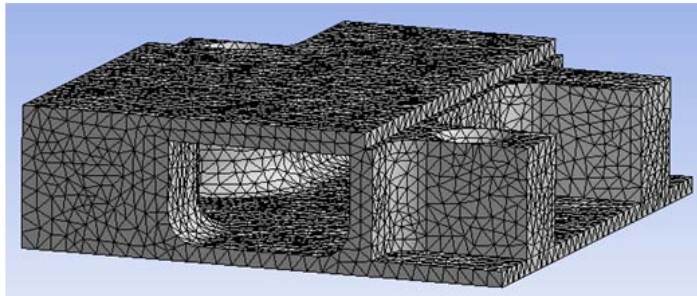
Figure 4.15: FEM model of one of the critical areas of the ELISE plasma grid.
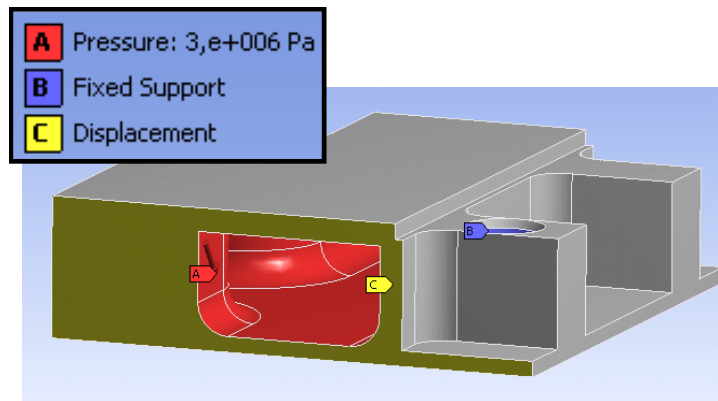
Figure 4.16: Boundary conditions for one of the critical areas of the ELISE plasma grid.
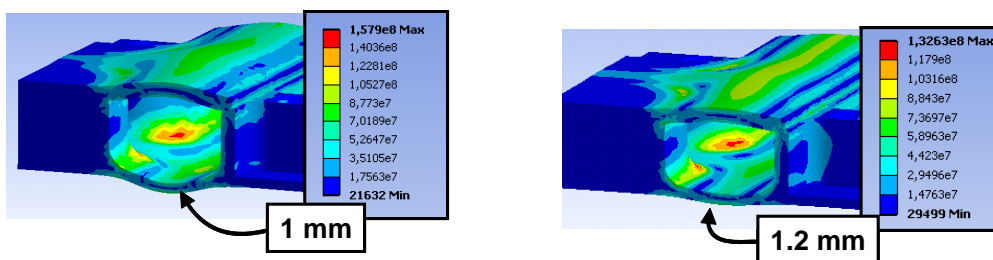
Figure 4.17: Left: first evaluation of Von Mises Stresses for one of the critical areas of the ELISE plasma grid. Right: final evaluation of the Von Mises Stresses for one of the critical areas of the ELISE plasma grid.

Chapter 5

Extraction grid

5.1 Introduction

Another example of a component with several requirements and with complex interaction between physical and technical aspects is the extraction grid. The extraction grid is one of the most important components of the extraction system because its design influences several aspects of the negative-ion source.

The grid is typically at 5-10 kV voltage difference with the plasma grid in order to extract the negative ions from the source. The extraction grid geometry and its distance from the Plasma grid are therefore important to determine the optical characteristics of the extracted ion beam.

Inevitably electrons are co-extracted by the extraction grid and must be deflected. This is performed by many rows of magnets, embedded inside the grid, that produce an Electron Deflection Field (EDF), already discussed in section 4.5. This Electron Deflection Field reaches the plasma side of the Plasma grid and influences the source performance in a way that is not fully understood. The main purpose of the Electron Deflection field is to filter the co-extracted electrons and to separate them from the beam. This is possible due to the different mass of electrons and ions. The negative ions are not significantly affected by the EDF and continue their trajectory through the extraction apertures almost undisturbed. On the contrary electrons are deflected onto the EG in crescent-shaped profiles as described in section 5.2. The power density in the footprints of the electron impact sites is very high, in the order of tens of MW/m^2, with a total load for one extraction grid segment in the order of hundreds of kW.

A water cooling is necessary to remove the heat from the extraction grid to avoid overheating and thermo-mechanical stresses. However thermal loads in the extraction grid cannot be avoided, but only minimized. The thermal load causes deformation of the extraction grid, in particular bowing and lateral expansion of
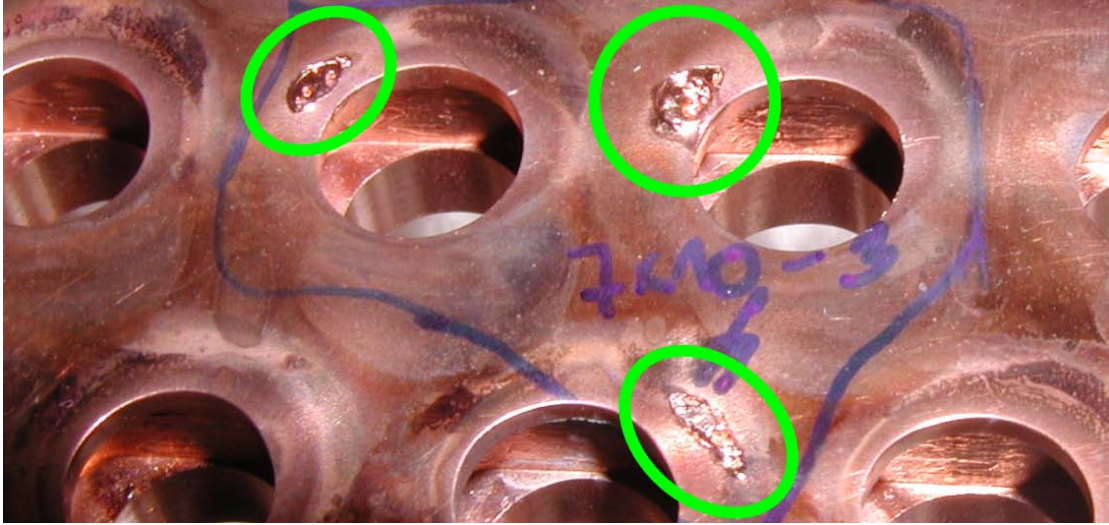
Figure 5.1: Extraction grid of BATMAN experiment damaged by co-extracted electrons.

the Grid, both detrimental for the optical performance of the extraction system. In fact bowing changes the distance between plasma grid and extraction grid, while lateral expansion of the grid can cause an offset between the extraction apertures that in turn causes undesired beam steering. Thermo-mechanical stresses are also a concern, due to the high thermal gradient and have to be kept as low as possible.

There is a certain degree of uncertainty in the parameters to be considered for the design of the extraction grid. For instance during source conditioning, electron to ion current ratio can be considerably higher than 1 [65]. Past experiments at IPP have shown a local melting of the EG surface [64], that only affects individual apertures, visible in figure 5.1. It is therefore highly advisable to aim for a robust design of the extraction grid, so that random variations of the power load on the extraction grid can be tolerated.

Experimental evidence shows that a higher extraction voltage results in higher negative ion current [66]. This means that, with a view to the general future development of negative-ion sources, a higher extracted negative ion current density can be achieved with an extraction grid capable of sustaining a higher extraction voltage. Therefore a cooling circuit design that allows for higher thermal load from impinging electrons on the Grid surface, derived by the higher co-extracted electron current, is desirable.

For these reasons a significant effort has been undertaken at IPP to develop an optimized cooling system for the EG.

In this chapter the procedure for the evaluation of the power loads and the optimization of the cooling circuit design for the extraction grid of ELISE is shown.

This comprises the evaluation of the electron trajectories and power loads, as well as the study of the cooling efficiency of several geometries of cooling channels. The efficiency of the cooling circuit has been evaluated also with a CFD code, due to the complex geometry of the cooling channels. Coupled thermal-mechanical calculations have been performed to compare several different EDF configurations with the design of the ITER extraction grid [29], that represents the initial input of the design of the extraction system for ELISE.

This study refers to an extracted electron current density of 400 A/m^2 and extraction voltage of 10 kV, resulting in a total power load of 150 kW on each EG segment. These values, close to those required for the ITER source [55], have been chosen so that water temperature in the cooling channels remains below the boiling point and therefore a relatively simple one-phase model can be used for the computational fluid dynamics (CFD) simulations. However the cooling circuit of the ELISE EG allows higher heat load regimes, as shown later in section 5.5.

5.2 Electron trajectories and power loads

The reliable operation of the extraction grid in a negative-ion source depends mostly on the capability to withstand the heavy loads caused by the co-extracted electrons. The power density distribution on the extraction grid surface depends on many factors:

- The voltage difference between the Plasma and the extraction grid

- The magnetic field configuration

- The shape of the plasma grid and the extraction grid and their distance

- The characteristics of the extracted negative ion beam (e.g. the extracted current density).

The determination of the power density distribution on the extraction grid is therefore a complex problem in the most general case. However for the design of the ELISE extraction system some parameter are fixed, due to the requirements of the ITER NBI system. In this study the extraction voltage is fixed to 10 kV, the shape of the extraction grid and the extraction apertures are those defined in section 3.4, while the shape of the plasma grid has been defined in Chapter 4. The distance between the Grids is 6 mm, like in ITER. The extracted ion beam current density calculated by KOBRA3, with an extracted ion current density of 250 A/m^2. The only remaining parameter that can change the power density distribution on the extraction grid surface is the magnetic field configuration. The
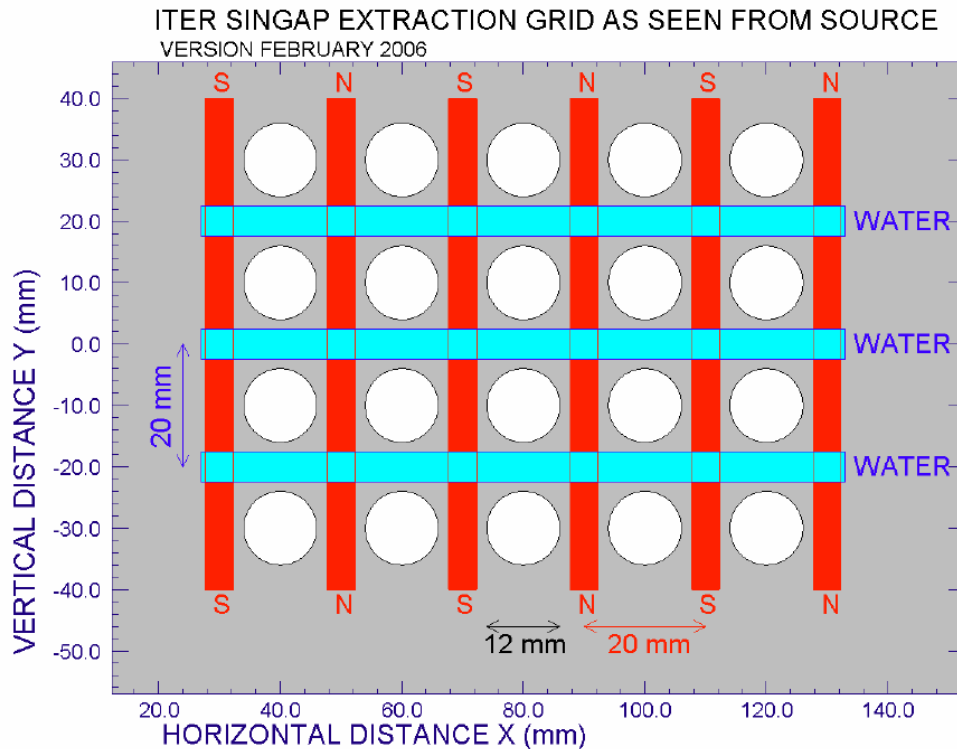
Figure 5.2: Detail of the geometry of the SINGAP extraction grid as seen from the source. The aperture diameter is 12 mm. The width of the magnets is 4.6 mm. The water channels are 5 mm wide.

two main sources of magnetic field in the extraction region are the filter field (FF) and the Electron Deflection Field (EDF).

The design proposal for the ITER-SINGAP extraction system was to arrange the electron deflection field and the filter field in *parallel* configuration. The EDF in this configuration has a strong horizontal component that alternates its direction from row to row of apertures. Also the filter field has mainly a horizontal component, being generated by vertical packets of magnets like in BATMAN or MANITU [46] or by a PG current like in ELISE [67]. This means that in SINGAP the transverse component of the EDF was either adding or subtracting from the filter field, alternatively, from row to row of apertures, like shown in figure 5.2. This is shown in figure 4.12 from the calculations described in the previous chapter.

Most of the negative-ion sources for NBI worldwide (including the testbeds at IPP BATMAN and MANITU) use an *orthogonal* Electron Deflection Field with respect to the filter field. This means that the magnets of the EDF are positioned in horizontal rows, producing a magnetic field that has a main vertical component
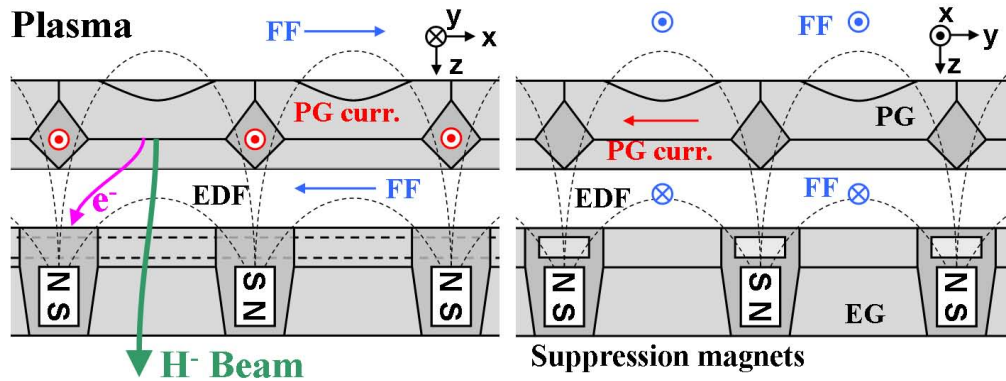
Figure 5.3: Parallel (left) and Orthogonal (right) configurations of EDF with respect to FF with ion and electron trajectories schematically represented.

that does not add or subtract directly to the FF horizontal component. Instead the superimposed FF slightly distorts the EDF to the right or to the left, alternatively, from row to row of apertures. These two configurations are compared in figure 5.3.

Power loads on extraction grid surface The co-extracted electrons are deflected in different ways according to the orientation of the EDF. The parallel configuration of EDF and FF produces footprints of the power load on the EG surface from the electron impact points that have a "crescent-like" shape, shown in figure 5.4. The profile shape differs according to the superimposition of EDF and FF, i.e. the power density is lower for the electrons deflected by the added EDF and FF, while it is higher for the subtracted fields.

This can be explained by the deflection of the co-extracted electrons which depends on the strength of the magnetic field resulting from the superimposition of EDF and FF.

In parallel configuration, when the two fields are added, the deflection of the electron trajectories, caused by the stronger horizontal component of the resulting magnetic field, is higher. As a consequence the power load density on the extraction grid surface is smaller. Vice versa in case EDF and FF are subtracted.

In case the EDF and FF are in orthogonal configuration it is not possible to represent the resulting fields in terms of addition or subtraction, due to the 3-dimensional nature of the problem. The electron trajectories are deflected into the extraction grid surface in patterns similar to the to the power load distribution generated by the "parallel" orientation of EDF and FF, but rotated by 90°. The power load distribution for the orthogonal configuration is positioned alternatively to the left or to the right of the extraction apertures, with a symmetric profile, shown in figure 5.4.

The ELISE EG has been designed to allow both configurations, giving the
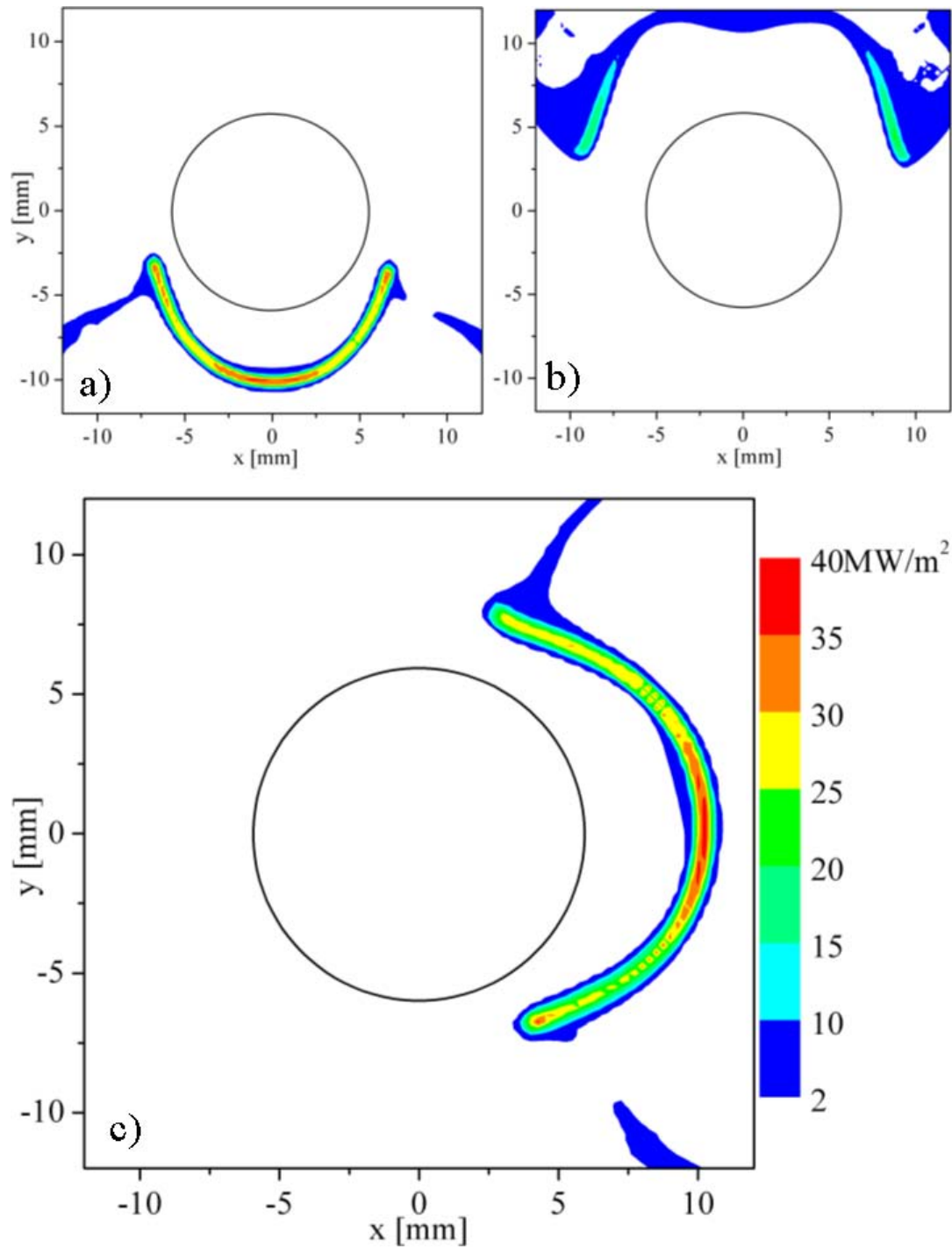
Figure 5.4: Power density deposition by co-extracted electrons (for 10 kV acceleration and 250 A/m^2 current density) for EDF parallel to FF in subtracted (a) and added (b) fields, and for EDF orthogonal to FF (c).
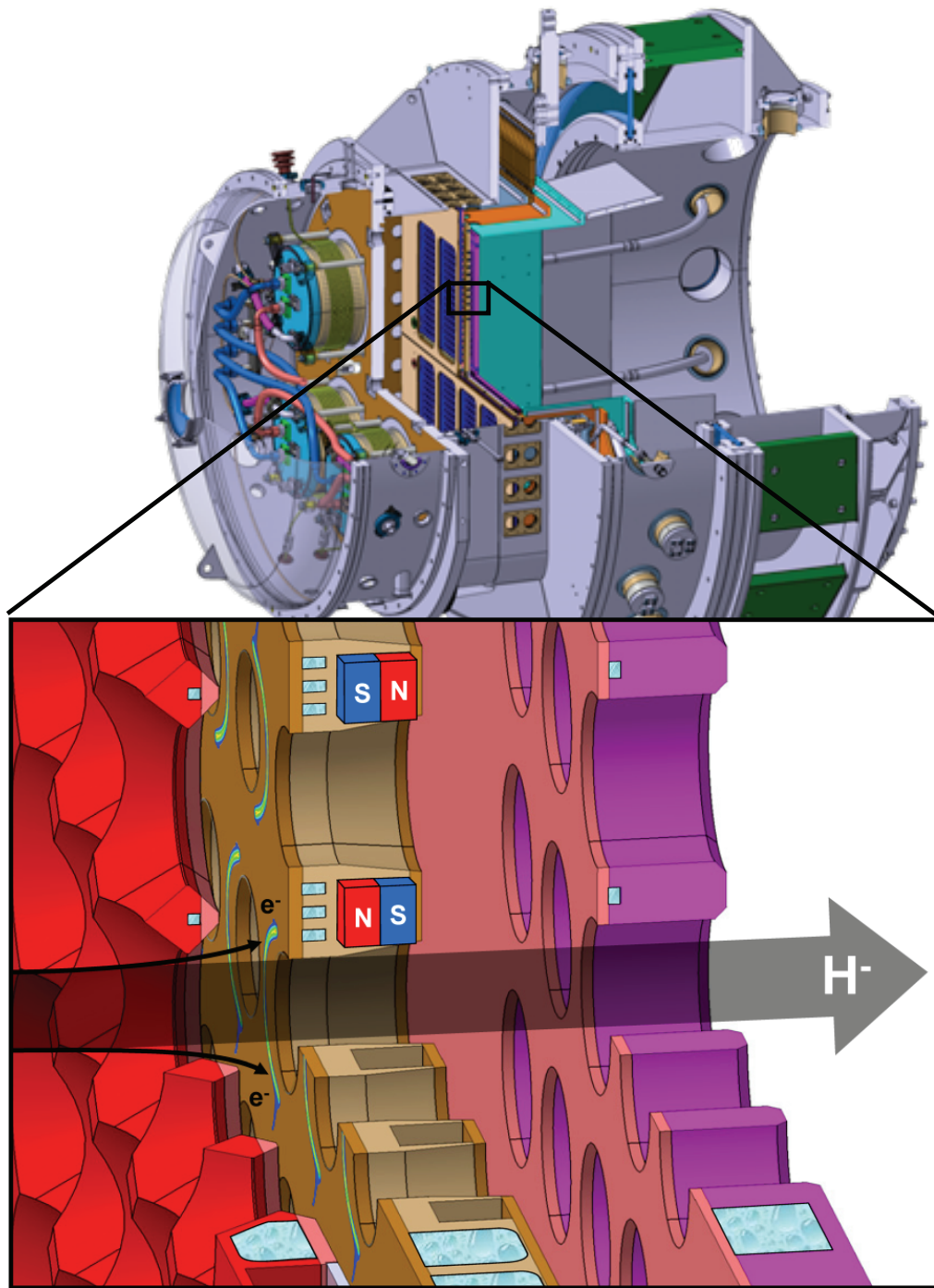
Figure 5.5: ELISE source and (magnified) section of the extraction system of ELISE. The extracted negative Hydrogen ion beam and the co-extracted electrons are schematically represented. The EDF permanent magnets are shown in orthogonal configuration.

possibility of a comparison of the respective performances in the same ion source [68]. A section view of the extraction system of ELISE is shown in figure 5.5.

The electron power distribution on the EG surface has been evaluated for the orthogonal and parallel configurations using the FEM code ANSYS [69] for the 3D magnetic field analysis, the KOBRA3 [56] code for the ion trajectories in combination with the Etron code [70] for the electron trajectories.

The power load distribution on the grid surface calculated for the ITER-SINGAP extraction grid had a maximum power density of 16 MW/m² [9]. The power load distributions calculated for the ELISE extraction grid, shown in figure 5.4 have a higher peak value, about 40 MW/m² because, conservatively, electron reflection from the Extraction grid surface has not been taken into account from the Etron code. In addition for safety reasons the co-extracted electron-to-ion current ratio has been assumed to be $j_e/j_{H^-} = 1.5$.

5.3   Optimization of cooling channels

Once the power loads distribution for the two magnetic field configurations parallel and orthogonal has been determined it is possible to optimize the design of the cooling circuit for the extraction grid. A design solution to remove the heat from the extraction grid was already present in the SINGAP design, proposed by ITER. In the framework of this thesis a study has been performed to select an alternative solution for the cooling circuit of the extraction grid of ELISE, based on a different water channel design. This alternative solution has been used for the design of the extraction grid of ELISE and has then been compared to the ITER-SINGAP solution, via several computational models, to asses the performance increase.

5.3.1   Number and geometry of the cooling channels

The SINGAP cooling system consists of straight cooling channels of 5×2 mm cross section, one channel between each row of apertures, as shown in figure 5.6. A cooling channel is positioned 1 mm below the extraction grid surface. The extraction grid is manufactured from pure copper, a material with the extremely high thermal conductivity $k = 400$ W/mK. Dividing the conductivity of copper by the thickness l_{th} of the material above the water channel (1 mm) it is possible to define a *heat transfer coefficient* for the bulk copper above the water channel:

$$h_{Cu_{1mm}} = \frac{k}{l_{th}} = \frac{400}{0.001} = 400000 \; W/m^2K$$

where $h_{Cu_{1mm}}$ is the the rate of transfer of heat through one square meter of a structure divided by the difference in temperature across the structure.

As a comparison it is possible to define a heat transfer coefficient also for the surface of the cooling channel, the *convection coefficient* of a water channel:

$$\alpha = \frac{k_w}{D_h} Nu$$

where k_w is the thermal conductivity of water, D_h is the hydraulic diameter of the water channel and Nu is the *Nusselt number* that can be found using several correlations. In general:

$$Nu \propto Re^x \cdot Pr^y$$

with the *Reynolds number (Re)* and the *Prandtl number (Pr)* defined as :

$$Re = \frac{\rho_w v D_h}{\mu_w} \quad ; \quad Pr = \frac{c_{pw}\mu_w}{k_w}$$

v is the water velocity, ρ_w the water density, μ_m the water viscosity, and c_{pw} the specific heat of water. Due to the dependence of ρ_w, μ_m and c_{pw} on the water temperature, the convection coefficient is also strongly dependent on the temperature on the cooling water.

For a cooling channel with water velocity in the range of $12\,\mathrm{m/s}$ the convection coefficient is in the range of $\alpha = 50000 \div 100000\ \mathrm{W/m^2K}$, depending on the water temperature and channel geometry. This lower heat transfer coefficient of a water channel surface, compared to the bulk copper material, has as a consequence that, locally, the heat removal by the surface of a water channel is less efficient, resulting in local higher temperatures. It is possible to verify this with a simple 2D FEM model of a section of the SINGAP extraction grid where a high power load ($10\,\mathrm{MW/m^2}$) is applied to the grid surface cooled by the SINGAP-like wide water channel. The heat is removed more efficiently from the sides of the channel than from the area above the water channel, as it is visible in figure 5.6.

Therefore, although water is necessary to remove the heat from the extraction grid and transport it out of the extraction system, a wide cooling channel is not an efficient solution to limit local maximum grid temperature.

A cooling channel geometry based on multiple channels with high aspect ratio, and larger cooling surface, has been investigated. This design is based on the IPP experience with the calorimeter panels of the ASDEX Upgrade for the positive NBI system [71] and on an analysis of the geometry of the cooling channels of rockets combustion chambers [72]. For better cooling efficiency it is not possible to simply increase the water velocity inside the cooling channels above the design value of $12\ m/s$ as this might trigger cavitation and material erosion. A simple 2D conceptual study has been performed in ANSYS by means of a thermal model. Four different channel geometries, as defined in figure 5.6, have been compared. In
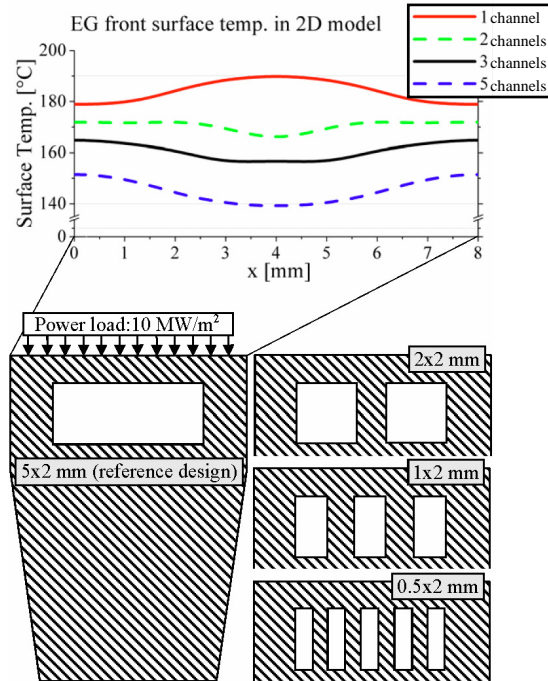
Figure 5.6: Temperature distributions on the front surface of the EG model for the four different cooling channel geometries that have been compared in a 2D conceptual study with a uniform power load. Left, the ITER SINGAP reference solution.

this preliminary evaluation a constant heat transfer coefficient of 80000 W/m^2K and water temperature of 55°C have been used for simplicity. From figure 5.6 it is evident how a higher number of channels, and a larger aspect ratio (channel height/width), can improve the cooling efficiency considerably.

Considering that it is not possible to significantly increase the convection coefficient by increasing water velocity, the heat transfer has been enhanced increasing the total "wet" surface. In addition dividing the channels in many smaller channels, vertical ribs of bulk copper are created in between the water channels. These ribs act as additional heat conduction efficiently removes the heat from the upper surface of the grid (where the power is deposited) and transports it to the long sides of the cooling channels up to the colder bottom side of the grid.

With this approach it is possible to increase the cooling efficiency increasing the number of cooling channels up to a certain point, where other factors become important, like increase of pressure drop or manufacturing reasons. In the case of the cooling circuit for the extraction grid the 3-channels geometry, with channels of section $1 \times 2\,mm^2$ (width × height), represent the optimum solution (see figure 5.7). Smaller channels are very difficult to manufacture in copper and would raise the cost to unacceptable values.
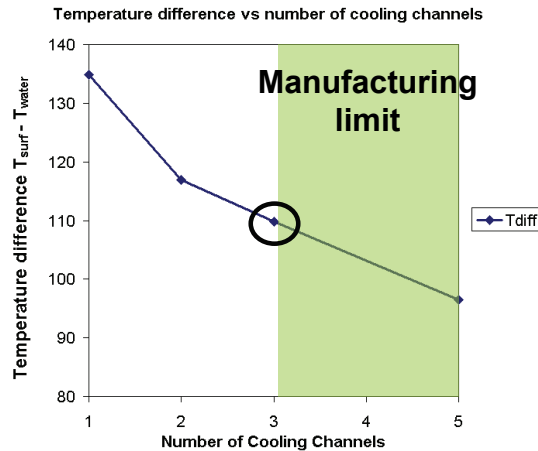
Figure 5.7: The maximum number of cooling channels for the cooling circuit of the EG is limited to 3 due to manufacturing reasons.

5.3.2 Cooling circuit for ELISE EG

Once the optimal number and geometry of cooling channels has been determined for the 2D geometry, the concept has been adopted for the design of the real geometry of the extraction grid of ELISE.

Due to the presence of the extraction apertures, straight cooling channels through each row of apertures, like in the extraction grid of SINGAP (figure 5.8), are not an optimal solution. In fact part of the grid surface, especially in the horizontal gap between the apertures, is relatively far from the straight cooling channel. This is particularly critical for the orthogonal configuration of EDF and FF, because in this case the hot spots from the power loads due to the co-extracted electrons lie in the region between the apertures that is less efficiently cooled.

With the 3-channels concepts it is possible to introduce curved channels and therefore to reach a larger grid surface. This is particularly important to optimize the cooling of the extraction grid for both orientation of EDF (parallel and orthogonal) and both power load distributions of co-extracted electrons.

Two curved channels and one straight channel, with 1 mm width for 2 mm depth, have been adapted to the ELISE EG aperture geometry, as visible in figure 5.9. Curved channels are longer and have higher pressure drop with respect to the straight ones. To assure the same average water velocity and flow rate of straight and curved cooling channels, the curved channels have been designed with an enlarged section between the beamlet groups.

To limit the pressure drop the cooling circuit has been split into two, as shown in figure 5.9, with one inlet and one outlet for each side of the grid segment, each one supplying only one half of the segment.
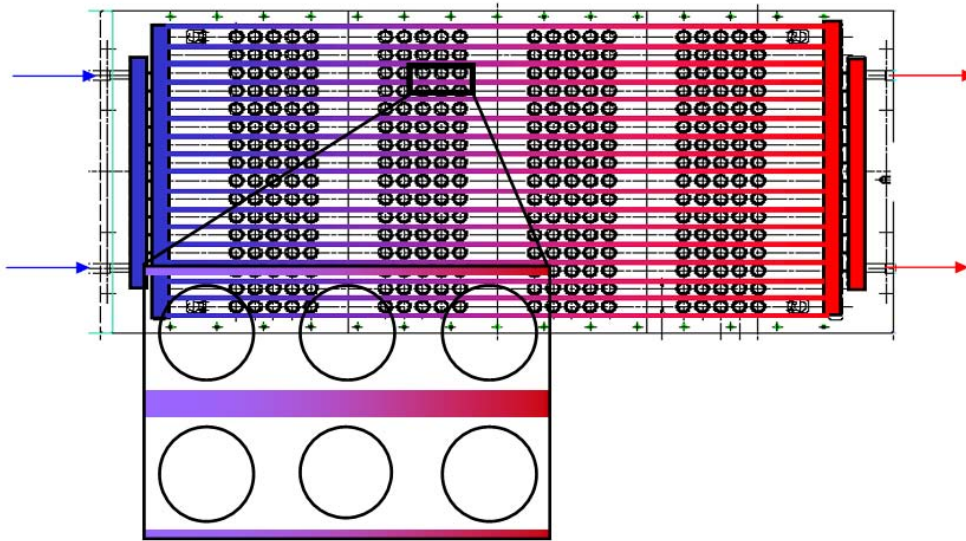
Figure 5.8: Scheme of cooling circuit for the extraction grid of SINGAP. A portion of the grid is magnified to show the straight cooling channels.

The water flow for the SINGAP configuration is 2 kg/s for each grid segment, leading to 12 m/s water velocity in the cooling channels. The same water velocity has been kept for ELISE, giving 2.4 kg/s for each extraction grid segment.

Grooves for electron deflection magnets are embedded between each row and column of apertures in vertical as well as in horizontal direction thus allowing both magnetic configurations, parallel and orthogonal of EDF and FF. As show in figure 5.10 the permanent magnets can be inserted through window openings on the back side which will be closed by screwed cover plates.

5.4 CFD and FEM models

After the design of the cooling circuit for the extraction grid of ELISE has been defined, a series of 3D simulations have been performed to compare the ELISE EG cooling circuit design to the SINGAP reference design.

Figure 5.11 shows a view of the extraction grid of ELISE where a portion of the Grid used for the CFD and FEM simulations has been highlighted. A similar portion of the SINGAP extraction grid has been selected.

This portion contains two rows of apertures. Due to the very localized heat load from the co-extracted electrons discussed in section 5.2, a very fine surface mesh, shown in figure 5.12, is required to model thermal gradients accurately, with a typical size of 0.25 mm. The number of nodes required to mesh the portion of the extraction grid is a few millions, the exact number depending on the geometry
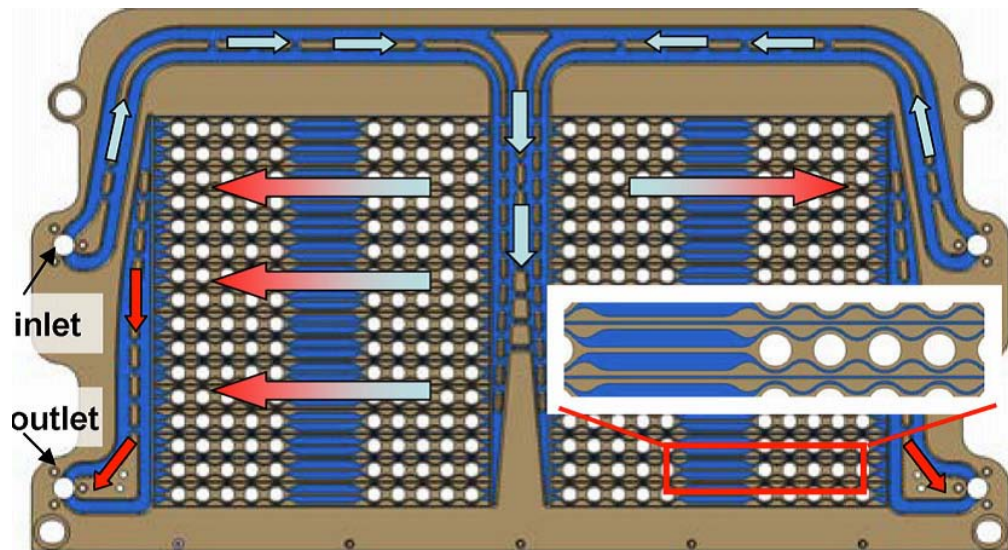
Figure 5.9: View of the cooling circuit inside a segment of the extraction grid of ELISE. The cooling channels are magnified to show the complex geometry, with curved channels and widenings to balance the pressure drop of curved and straight channels.
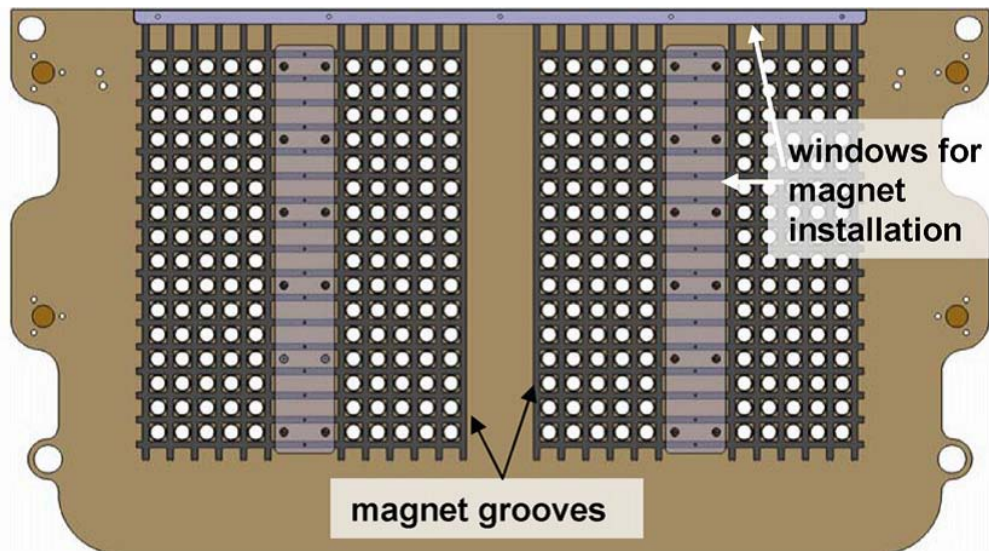
Figure 5.10: View of the back-side of the ELISE extraction grid. Vertical and horizontal magnet grooves allow both orthogonal and parallel configuration of EDF and FF.
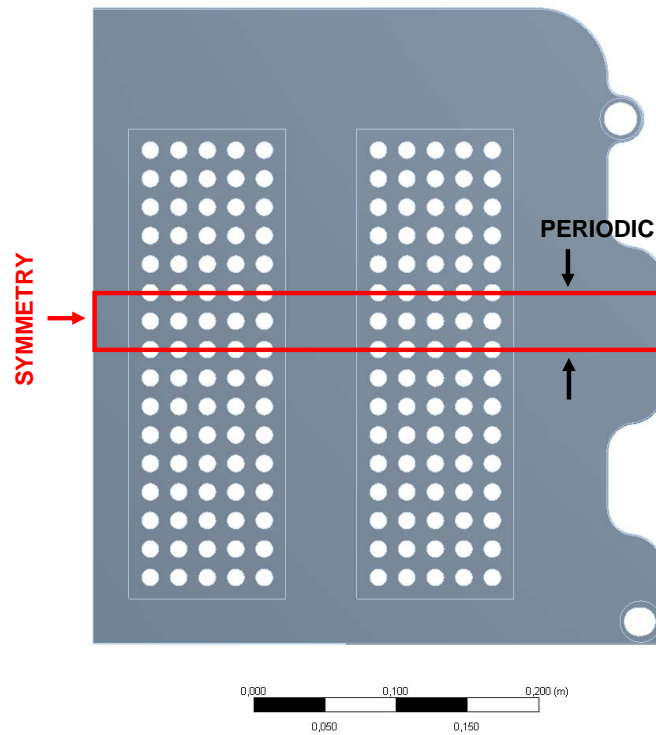
Figure 5.11: View of the extraction grid of ELISE. The section used for the CFD and mechanical simulations is highlighted and symmetry and Periodic boundary conditions are shown.

of the cooling circuit.

Introducing into the model symmetric and periodic boundary conditions, also shown in figure 5.11, the small grid portion represents the behavior of an infinitely long grid.

Considering the relatively complex geometry of the cooling circuit, fluid-thermal calculations have been performed by means of the CFD code CFX [73]. This is particularly important to evaluate the Heat Transfer Coefficient (HTC) on the surface of the curved cooling channels, where the changes on flow direction generate a strongly non-uniformity HTC. This higher accuracy in turn provides a better estimation of the temperature distribution in the extraction grid.

To model the flow near the wall in the CFD simulations the Shear Stress Transport (SST) model has been used. All the models have channels meshed with 30 inflation layers to achieve an accurate resolution of the boundary layer.

Several meshed models have been compared to determine the best mesh parameters for the simulations in order to assure the independence of the results from the mesh.
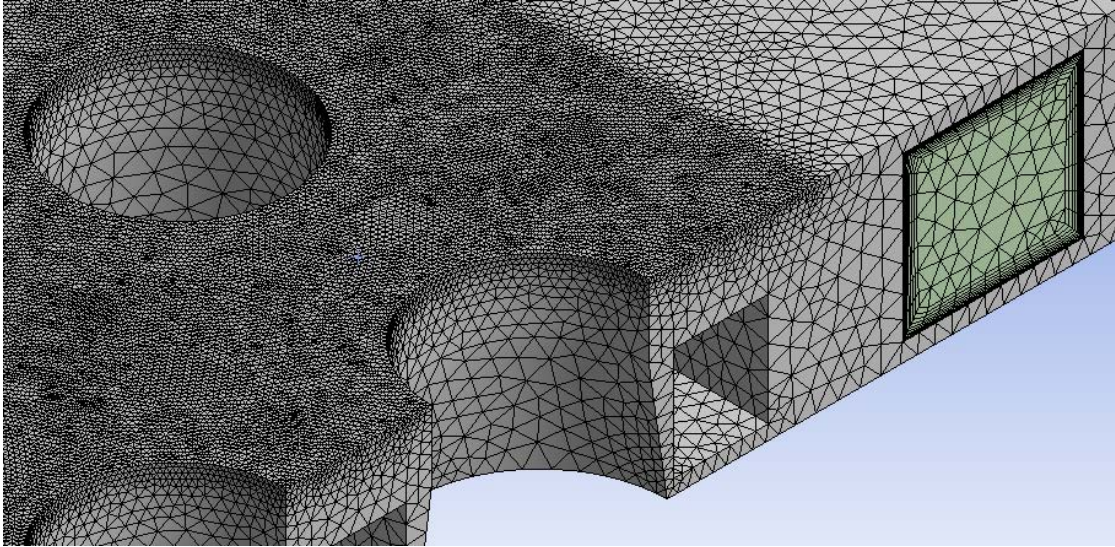
Figure 5.12: Close-up of the mesh for the portion of the extraction grid of ELISE modeled with ANSYS for the fluid dynamic code CFX. The water manifold is shown in green, while the grid material in shown in gray.

To consider the thermal conduction between fluid in the cooling channels and solid material in the extraction grid, conjugate heat transfer has been applied [74].

For the thermo-mechanical calculations the temperature field from CFX has been imported in *ANSYS mechanical APDL*,[1] where a linear-elastic model of the extraction grid, based on the same grid portion, has been implemented. As for the CFD analyses, appropriate symmetric and periodic conditions have been defined for the mechanical simulations.

The two extraction grid geometries ELISE and SINGAP have been evaluated applying power loads distribution from co-extracted electrons resulting from both parallel and orthogonal configuration, as defined in section 5.2.

5.5   Results

The four simulation cases resulting from the comparison of the extraction grids of ELISE and SINGAP for the two magnetic field configurations orthogonal and parallel have been evaluated using the following parameters:

- Maximum temperature of extraction grid surface.

- Maximum temperature of channel surface.

---

[1]formerly *ANSYS Classic*
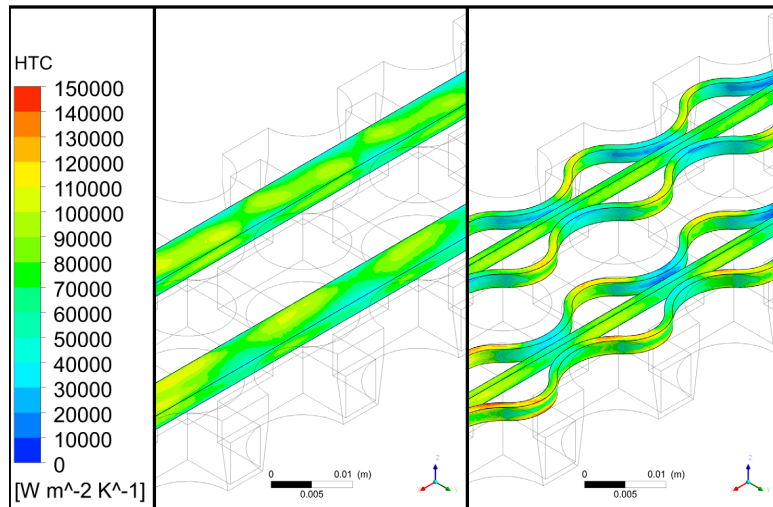
Figure 5.13: Heat transfer coefficient distribution in EG cooling channels for SINGAP (left) and ELISE (right), EDF and FF in orthogonal configuration.

- Maximum bowing (deflection in direction of plasma grid).

- Maximum Von Mises Stresses.

Calculation times for the CFD simulations were in the order of hours, while the FEM simulations for the mechanical analyses could be performed in 10s of minutes, using quad-core Xeon X5450 3 GHz with 32 GB of RAM with four CPUs in parallel.

5.5.1   CFD calculations

As expected the HTC on the surface of the cooling channels of the extraction grid of ELISE, is significantly non-uniform if compared with the straight channel geometry of the SINGAP solution, as shown in figure 5.13. Nevertheless the cooling circuit of ELISE is more efficient for heat removal as shown in figure 5.14. In addition the surface of the cooling channel has lower temperature for ELISE compared to the SINGAP solution, as visible in figure 5.15.
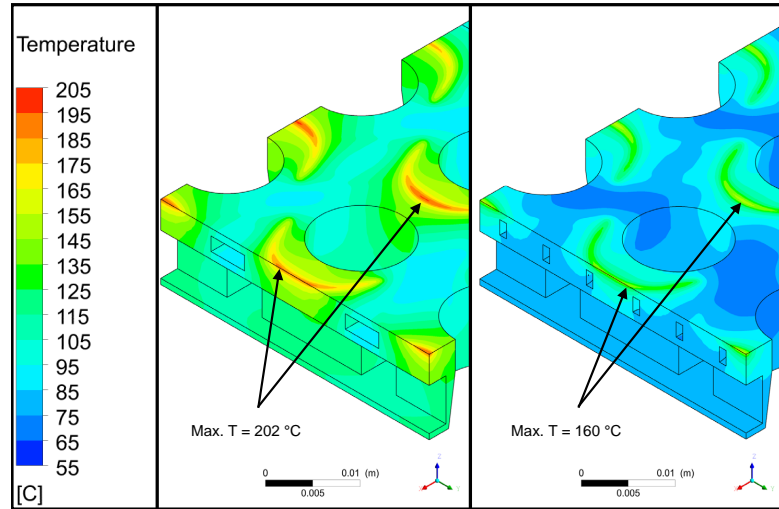
Figure 5.14: Temperature distribution in SINGAP (left) and ELISE (right) for EDF and FF in orthogonal configuration.
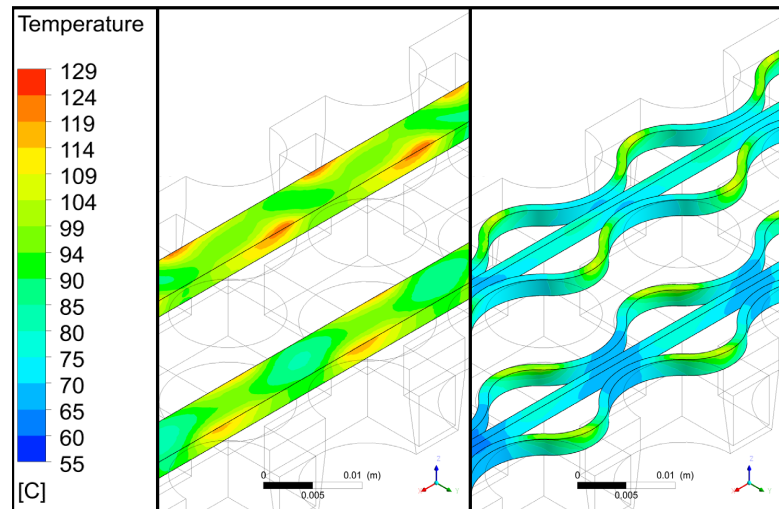
Figure 5.15: Surface temperature of cooling channels for the extraction grid in SINGAP (left) and ELISE (right)

The results of the CFD calculations are summarized in table 5.1. It is possible to see how the channel design for the extraction grid of ELISE is more efficient than the SINGAP design for both power loads distribution resulting from orthogonal and parallel magnetic field configurations. For the orthogonal configuration of EDF and FF the ELISE design of the EG cooling circuit provides 29% and 14% lower maximum grid temperature and maximum cooling channel temperature, respectively. For the parallel configuration the figures are 16% and 13% reduction of maximum grid temperature and maximum cooling channel temperature, respectively.

Table 5.1: Summary of results of CFD and FEM calculations for SINGAP and ELISE EG: max. surface temperature, max. water temperature, bowing deformation, max. mechanical stresses. For absolute temperatures add 55°C inlet water temperature.

	EDF-FF	SINGAP	ELISE	Diff. [%]
Max ΔT grid surf. [°C]	Paral	123	106	-16
	Ortho	147	105	-29
Max ΔT channel surf. [°C]	Paral	88	77	-13
	Ortho	74	64	-14
Max Δz [mm]	Paral	1.11	1.07	-4
	Ortho	1.10	0.40	-71
Max σ [MPa]	Paral	194	161	-17
	Ortho	252	125	-50

Therefore the new cooling circuit of ELISE represents a more robust solution, capable to better tolerate variations of the power density deposited on the grid surface compared to the SINGAP design.

Inlet water temperature is defined as 55°C. The calculated maximum water temperature remains below 150°C for all simulations. Therefore no boiling is present in the cooling channels as pressure at the EG outlet is set to 6 bar, below the vapor pressure. The critical heat flux for the EG cooling channels estimated according to Gunter [75] is 18.7 MW/m². The calculated maximum heat flux on the channel surface is 7 MW/m² for SINGAP and 5.5 MW/m² for ELISE, therefore assuring an increased margin of safety. This is a significant advantage also for Deuterium operation (see chapter 3), where the co-extracted electron to ion current ratio is higher, and higher extraction voltage is required [55].

Via a separate analysis (not shown here) it has been calculated that the average water velocity in the cooling channel is 12 m/s, while in the manifolds it is between 5 m/s and 7 m/s. Due to the presence of channels with smaller section and curved geometry, the cooling circuit for the extraction grid of ELISE has a pressure drop of 7.6 bar. This is considered an acceptable increase with respect to the 3.6 bar calculated for SINGAP also calculated separately.

5.5.2 Mechanical analysis

The temperature fields resulting from the CFD calculations have been used to evaluate thermo-mechanical stresses in the EG for the two magnetic configurations and to compare the ELISE and the ITER design. Maximum stresses and deformations are shown in table 5.1.

The results of the simulations show significant improvements of the ELISE design compared to the SINGAP design. In particular the improvement is more consistent comparing the two cooling circuit design under the load conditions with the orthogonal configuration of EDF and FF, where the grid bowing is reduced by 71% and the mechanical stresses by 50%. For the Parallel configuration the difference is less marked, with 4% and 17% less grid bowing and mechanical stresses respectively.

This result can be interpreted considering that for the parallel configuration the power load from co-extracted electrons is deposited mainly on the surface laying above or below the extraction apertures (cf. figure 5.4), therefore on top of the cooling channels both in SINGAP and in ELISE. In this configuration the cooling channels of the ELISE design provide a better cooling than the SINGAP design, due to the optimized design, but the temperature gradients in the grid, that affect deformations and mechanical stresses, are not significantly reduced.

On the other hand with the orthogonal configuration the power load is deposited left or right respect to an extraction aperture (cf. figure 5.4), therefore relatively far from the straight cooling channels of the SINGAP design. The curved cooling channels of the ELISE Design are even more efficient in this case, as they are designed to remove heat from a wider region around the extraction apertures.

In this study, pressure loads and the corresponding mechanical stresses are not taken into account, since they are not relevant for the small cooling channels. However they are important for the manifolds as has been shown in a specific separate analysis.

5.6 Summary

Ion beam and electron trajectories extracted from apertures with the geometry of the ELISE extraction system have been simulated to determine the power load deposition on the extraction grid surface caused by co-extracted electrons. A 2-dimensional local model of the extraction grid has been created to compare various cooling channel geometries with the ITER reference design. Considering design and manufacturing constraints an optimal 3-channel geometry has been identified. The 3-channels geometry has been adapted to the real geometry of the extraction grid and several solutions have been adopted to cool down most of the area of the

grid, to reduce pressure losses and to assure a uniform water flow in the many cooling channels.

CFD simulations have been performed to evaluate heat transfer coefficients and flow uniformity in the extraction grid cooling circuit. Conjugate heat transfer has been used to evaluate the efficiency of the cooling channels with respect to the heat removal.

Thermo-mechanical calculations have been performed on the basis of the temperature field resulting from the conjugate heat transfer analyses. Mechanical stresses and deformations have been calculated by means of FEM models representing a portion of the grid.

The ELISE design has been compared to the ITER reference design. In addition the two configurations of EDF with respect to FF, orthogonal and parallel, have been compared. Consistent performance improvements have been achieved with the ELISE design in all relevant parameter with respect to maximum grid temperature increase, maximum cooling channel temperature increase, maximum mechanical stresses and deformation, for both magnetic field configurations.

Chapter 6

Multidisciplinary optimization

6.1 Introduction

Multidisciplinary design optimization (MDO) is an are of engineering that makes use of optimization techniques to solve design problems involving two or more disciplines. Incorporating all relevant disciplines of a defined system simultaneously, engineers are able to find an optimum design. In many cases this method is better than a design found by performing the optimization in each discipline separately because it can make use of interactions between the disciplines. However, the complexity of the problem including all disciplines simultaneously significantly increases.

MDO has been implemented mainly in the field of aerospace engineering, such as aircraft and spacecraft design. For the conceptual and preliminary design stages of the proposed Boeing blended wing body (BWB) aircraft concept MDO has been used extensively [76]. However, these techniques have been used also in a number of other fields such as design of automobile components [77] and naval architecture [78].

The field of multidisciplinary optimization is presented in a comprehensive and detailed view in many text books e.g. [79, 80]. A thorough discussion is omitted here and only an introduction is given to the concepts and the methods used in the remainder of this thesis.

6.1.1 General definition of an optimization task

The goal of any optimization is to achieve the best possible design solution of a system or process in terms of one or more criteria within the scope of given requirements and limited resources. The criteria, which serve as a measure of the quality of a design, are called objectives. The requirements a design has to satisfy

are called constraints. The quantities that influence or define a certain design are called design variables.

The problem must be defined mathematically, therefore the design variables are assembled in a *vector* $\mathbf{x} = (x_1, x_2, \ldots, x_n)^T$ that belongs to a subset D of the n-dimensional real space $\mathbb{R}^n$.

The general formulation of a optimization task is given by 6.1:

$$
\begin{aligned}
\text{minimize } & f(\mathbf{x}) \\
\text{subject to } \mathbf{h}(\mathbf{x}) \ &= \ \mathbf{0}, \\
\mathbf{g}(\mathbf{x}) \ &\leq \ \mathbf{0}, \\
\mathbf{x} \in \mathrm{D} \ &\subseteq \ \mathbb{R}^n
\end{aligned}
$$

(6.1)

The function $f(\mathbf{x})$ representing the correlations between objective and design variables $\mathbf{x}$ is called an objective function. There can be more than one objective function defined $\mathbf{f}(\mathbf{x}) = (f_1(\mathbf{x}), f_2(\mathbf{x}), \ldots, f_{n_{ob}}(\mathbf{x}))$. The inequality and equality constraint functions are called $\mathbf{g}(\mathbf{x}) = (g_1, g_2, \ldots, g_{m_1})^T$ and $\mathbf{h} = (h_1, h_2, \ldots, h_{m_2})^T$ respectively. The lower and upper boundaries, $\mathbf{lb} = [x_{i_{lb}}]$ and $\mathbf{ub} = [x_{i_{ub}}]$, give the allowed range of the design variables $\mathbf{x}$ and thus define the design space D.

Finally, designs that satisfy all constraints are called feasible solutions. All feasible solutions x form the so called feasible set D_f:

$$D_f = \{x \in D | \mathbf{g}(\mathbf{x}) \leq \mathbf{0} \wedge \mathbf{h}(\mathbf{x}) = \mathbf{0}\}$$

The set that represents the feasible criterion points is $f(\mathbf{x})$ or A, the image of the set D_f under the action of f.

Problem formulation is one of the most difficult parts of the optimization process. It involves the selection of design variables, constraints, objectives, and models of the disciplines. The definition of the models determines the quality of the results as well as the computational effort. The problems under consideration in this work are based on finite element analyses [81].

6.1.2 Example of optimization task

If only one objective function exists, the problem is called a single objective problem. If more than one objective functions exist, the problem is a multiobjective problem. For the latter case additional aspects arise, which will be explained in detail in paragraph 6.2.

The different aspects and complexity of an optimization task can be illustrated by the following cantilever beam optimization problem.
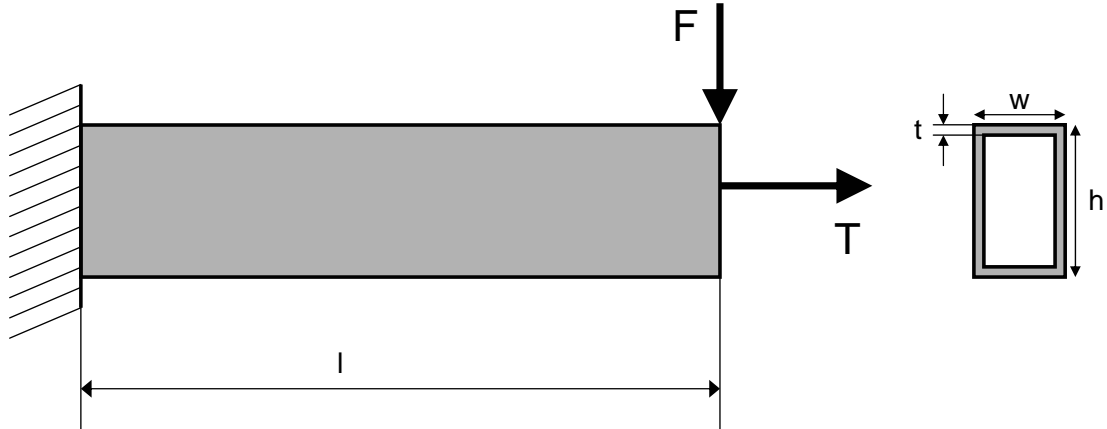
Figure 6.1: Example of optimization problem: cantilever beam subject to two load cases.

The cantilever beam shown in figure 6.1 is subject to two loads, a tip force F and a torsional moment T. The goal is to minimize the mass and the tip deflection of a cantilever beam. The cantilever beam has to be able to withstand the two loads. The maximum bending stress $\sigma_b(\mathbf{x})$ occurring in the beam should exceed the allowable stress $\sigma_p(\mathbf{x})$ of the respective material and the maximum shear stress $\tau_s(\mathbf{x})$ should not exceed the allowable shear stress $\tau_p(\mathbf{x})$. The dimensions can be varied in terms of height h, width w, as well as wall thickness t of the respective cross section. These three variables cannot be chosen independently from each other, e.g. the wall thickness is limited by the height and width.

Having described the problem, the cantilever beam optimization problem can be formulated in accordance to equation 6.1 as follows:

$$\min \mathbf{z} = [z_1, z_2] = \mathbf{f}(\mathbf{x}) = [m(\mathbf{x}), u_t(\mathbf{x})]$$
$$\text{with } \mathbf{x} = [h, w, t]$$
$$\text{subject to}$$
$$g_1(x) = \sigma_b(x) - \sigma_p(x) \leq 0$$
$$g_2(x) = \tau_s(x) - \tau_p(x) \leq 0$$
$$g_4(x) = t - w/2 \leq 0$$
$$g_5(x) = t - h/2 \leq 0$$
$$\text{and}$$
$$0 < t, w, h$$

where m is the mass and u_t is the tip deflection.

This example covers a large part of the challenges that can occur in structural optimization when two conflicting objectives are defined. The minimization of both objectives simultaneously is not possible. Thus, there is no unique solution

but a set of best compromise solutions. Eventually, the designer has to perform a trade-off analysis to the set of solutions and chose the optimized solution, of which objective has higher priority and in which measure.

6.2 Multiobjective optimization

In contrast to single objective problems, the quality of a design has to be compared in several dimensions in multiobjective problems. In practice, a multiobjective optimization is interesting when the problem has multiple objectives representing conflicting requirements, i.e. improving one objective has degrading effects on another objective. For this case, there is no single solution representing the minimum for all objectives simultaneously. However, a set of solutions exists called the *Pareto set* [82]. These solutions have in common that no other solution exists in the design space that is simultaneously better in all objectives. There are no optimal solutions where one objective function is improved, respect to the Pareto set, without increasing, i.e. worsening, the other objective function.

In engineering the Pareto frontier is particularly useful because, by focusing on the set of choices that are Pareto-efficient, a designer can make trade-offs within this set only, rather than considering the full range of every parameter. In the following subsection the specific definitions, characteristics, and principles of multiobjective optimization are introduced.

6.2.1 Concept of optimality in multiobjective optimization

The Pareto set consists of *Pareto optimal* points. A point $\mathbf{c}_0$ in the attainable set A is Pareto optimal if and only if there is not another $\mathbf{c} \in A$ such that $c_i \leq c_{0i}$ for all i and $c_i < c_{0i}$ for at least one i.

To illustrate the concept of Pareto dominance, one can take a look at the solution $\mathbf{c}$ in figure 6.2. Solution $\mathbf{c}$ dominates the solutions $\mathbf{d}$, $\mathbf{e}$, and $\mathbf{f}$ in the upper right rectangle, whereas solution $\mathbf{c}$ is dominated by the solutions $\mathbf{a}$ and $\mathbf{b}$ in the lower left rectangle. The other solutions like e.g. $\mathbf{g}$ are indifferent to $\mathbf{c}$. One can observe that there is a set of solutions that are not dominated by any other. They are so called non-dominated solutions and form a non-dominated front, which is indicated by the dash-dotted line.

The fundamental goal of a multiobjective optimization is to determine the Pareto set. The Pareto-optimal set is also called the Pareto-front. In figure 6.2 the gray marked area resembles the complete set of feasible solutions D_f, and the solutions $\mathbf{a}$ and $\mathbf{b}$ are Pareto-optimal. The set of all Pareto-optimal solutions forming the Pareto-frontier is marked as a dotted line. The above phenomena apply only for conflicting objectives. If the objectives are not conflicting one can
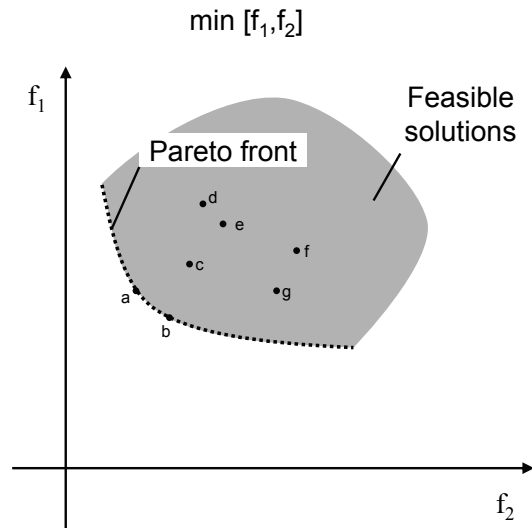
Figure 6.2: Example of a problem with 2 objective functions illustrating the concept of Pareto optimality

easily show that the multiobjective problem degenerates to a single-objective one. The Pareto-optimal set then comprises just a single optimum.

6.2.2 Solving method

The weighted sum approach is the simplest and intuitive way of aggregating multiple objectives into a single one. Here, the weighted sum approach will be briefly introduced and discussed:

Weighted Sum Approach The composite objective function is formed as a linear combination of all objectives. Weighting factors are then defined for each objective. These weights represent the relative preference between the already defined objectives. For example, in formal notations:

$$
\begin{aligned}
\min \mathbf{z} \;\; = \;\; & \mathbf{f}(\mathbf{x}) = \sum_{i=1}^{n_{ob}} w_i f_i(\mathbf{x}), \; \sum_{i=1}^{n_{ob}} w_i = 1, \; w_i \geq 0 \\
\text{subject to} \\
\mathbf{g}(\mathbf{x}) \;\; \leq \;\; & 0, \; \mathbf{g} = [g_1(\mathbf{x}), g_2(\mathbf{x}), ..., g_{n_{ic}}(\mathbf{x})] \\
\mathbf{h}(\mathbf{x}) \;\; = \;\; & 0, \; \mathbf{h} = [h_1(\mathbf{x}), h_2(\mathbf{x}), ..., h_{n_{ec}}(\mathbf{x})] \\
x_{i_{lb}} \;\; \leq \;\; & x_i \leq x_{i_{ub}}, \; i = 1, 2, ..., n_{dv}, \; i \in \mathbb{N}
\end{aligned}
$$

$$(6.2)$$
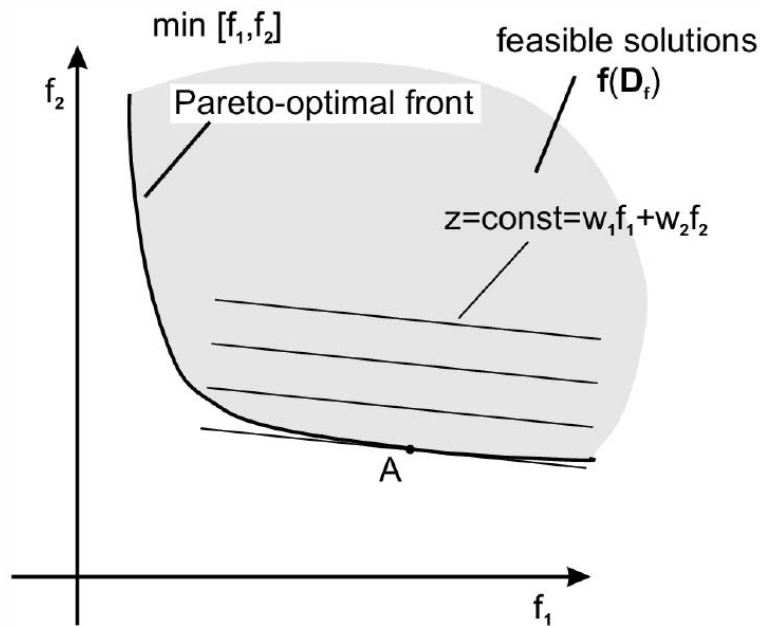
Figure 6.3: Description of the weighted sum approach for an example of optimization with two objective functions representing conflicting requirements.

The w_i are the weighting factors for each objective. In figure 6.3 the approach is demonstrated for two objective functions. The feasible region of the design space D_f is plotted in the objective space. For a given choice of the weighting factors w_1 and w_2, the isolines for constant z-values are plotted, which form straight lines. The gradient of these isolines is determined by the ratio of the weights w_1/w_2. Graphically, the optimization process can be imagined as moving a straight line parallel to the isolines towards lower z-values until it is tangent to the Pareto-Frontier. The tangent point A is then the resulting optimal design.

This method represents a considerable advantage, because it reduces a multiobjective problem to a single-objective problem. A large variety of algorithms exists for single-objective optimization. The possibility to use sophisticated single-objective algorithms also provides the advantage of a high efficiency and well defined convergence properties.

In the other hand, the method also possesses several drawbacks. One disadvantage is that only one Pareto-optimal solution is obtained per optimization run. In order to obtain multiple Pareto-optimal solutions to approximate the complete Pareto-front, multiple runs with different weighting have to be performed. Also, a uniformly spaced weight vector does not necessarily result in uniformly spaced

solutions on the Pareto-front. Another serious drawback is the difficulty to obtain all Pareto Optimal solutions for non-convex objective spaces. It results, it may not be possible to obtain the entire Pareto front.

However it is not possible to know a priori the shape of the objective space, therefore in this study first search for the Pareto solution and then its shape and characteristics are analyzed. Only at that point it will be possible to evaluate the efficacy of the approach chosen for the optimization.

6.2.3   Optimization process - overview

After the optimization problem has been formalized, an optimization method can be employed to solve it. In order to solve the optimization problem defined in section 6.1.1, an automated, i.e. computer based, method can be used. There are two main components of this automated process, namely:

- a simulation model, which provides objective and constraint function results for a given set of design variables

- an optimization algorithm, that provides the steering logic for changing the design variables to improve the solution.

This iterative process starts from an arbitrarily chosen start point (e.g. a random set of design variables). Afterwards the simulation model evaluates this starting design. The evaluated outcomes of the simulation model are entered into the optimization algorithm, which will then change the design variables based on some internal logic. The new design or set of designs are again evaluated by the simulation model and the result is presented to stopping criteria. The stopping criteria are usually based on solution convergence. If this criteria are met, an optimum has been achieved and the process is stopped. Otherwise, the next iteration is started. In figure 6.4 the fundamental concept of an iterative optimization method is illustrated.

In the context of optimization, a decisive factor is the computational cost of the simulation model. Depending on the algorithm, a large number of evaluations are required. The high computational cost can be unaffordable results in exclusion of the optimization tool.

Although the history of modern optimization is relatively short, approximately 30 years, a considerable amount of optimization algorithms have been developed. For this study, a gradient based algorithm is used in the MATLAB function *fmincon* [83]. This algorithm has been chosen because it can be applied to constrained nonlinear problems, as described in chapter 7, is robust and has a low computational cost.
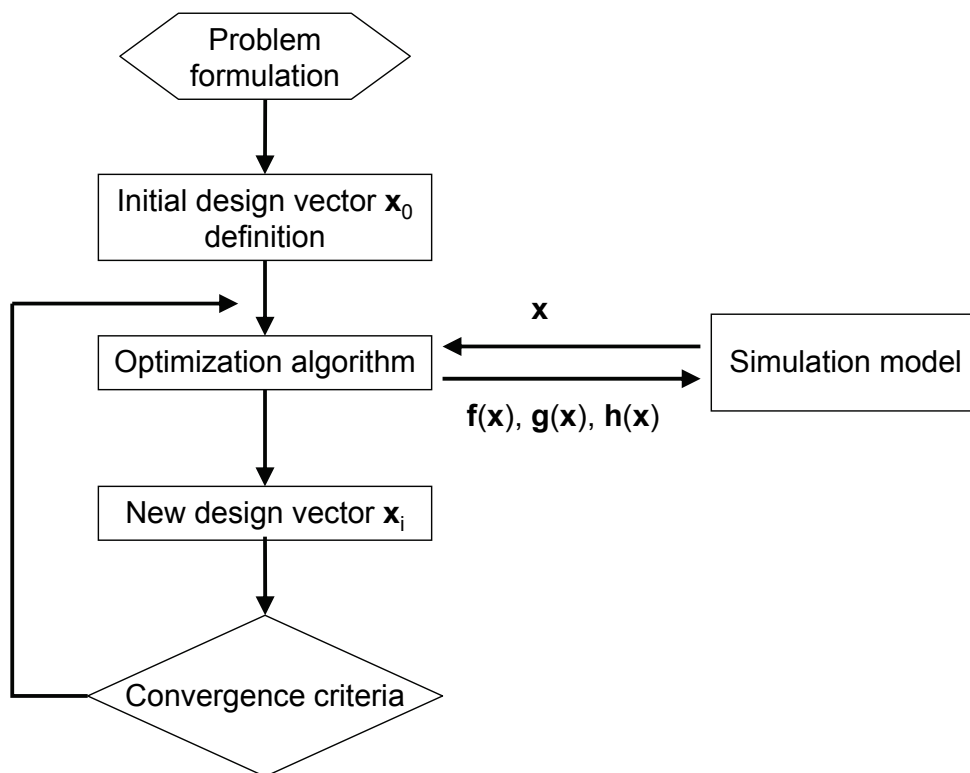
Figure 6.4: Basic flow chart for an automated, iterative optimization method

6.3   Approximation methods

Numerical noise   The term noise is usually referred to fluctuations in the output of an experiment, which are unrelated to the inputs. In physical experiments, noise leads to random variation in the response even if the input is always the same, as many factor are not under the direct control of the experimenter.

A computer simulation can be seen as a computational experiment, in which input data are given to a model that returns an output. In this context, the process is deterministic, i.e. given the same input, the model will return always the same output. There is likely to be a computational error in the result, but this error is repeatable. However, a slight variation in the input values given to the simulation may result in rather big variation of the output due to the fluctuations in the error itself. This may happen when performing a fast FEM simulation by means of a coarse mesh. Such variation from the expected smooth response is the numerical noise.

In multidisciplinary optimization, numerical noise is often a problem. In particular, gradient based optimization algorithms do not always converge in presence of noise.

6.3.1   Metamodels replacing computer simulations

In the presence of numerical noise, one way to improve the performance of gradient-based optimization algorithms is to use response surface models (RSMs, also known as surrogate, meta, or approximation models) [84, 85]. Instead of calling directly the computer code, an optimization routine can take values from a surrogate model of the computer code. The output of a computer simulation affected by noise and the respective approximation response surface are shown in figure 6.5.

Response Surface Models   Response surface models are polynomial regression models that establish an explicit functional relation (response surface) between input variables v and output values y. This can be done by fitting the parameters β of a *regression function* $\eta(\mathbf{v}, \boldsymbol{\beta})$ to the response values. Therefore:

$$\mathbf{y} = \eta(\mathbf{v}, \boldsymbol{\beta}) + \boldsymbol{\varepsilon} \tag{6.3}$$

with $\boldsymbol{\varepsilon}$ representing the inaccuracy.

Typically the regression function η is linear with respect to the *regression coefficients* β:

$$\eta(\mathbf{v}, \boldsymbol{\beta}) = \beta_0 + \sum_{j=1}^{n_\beta} \beta_j \eta_j(\mathbf{v}) = \beta^T \eta(\mathbf{v}) \tag{6.4}$$
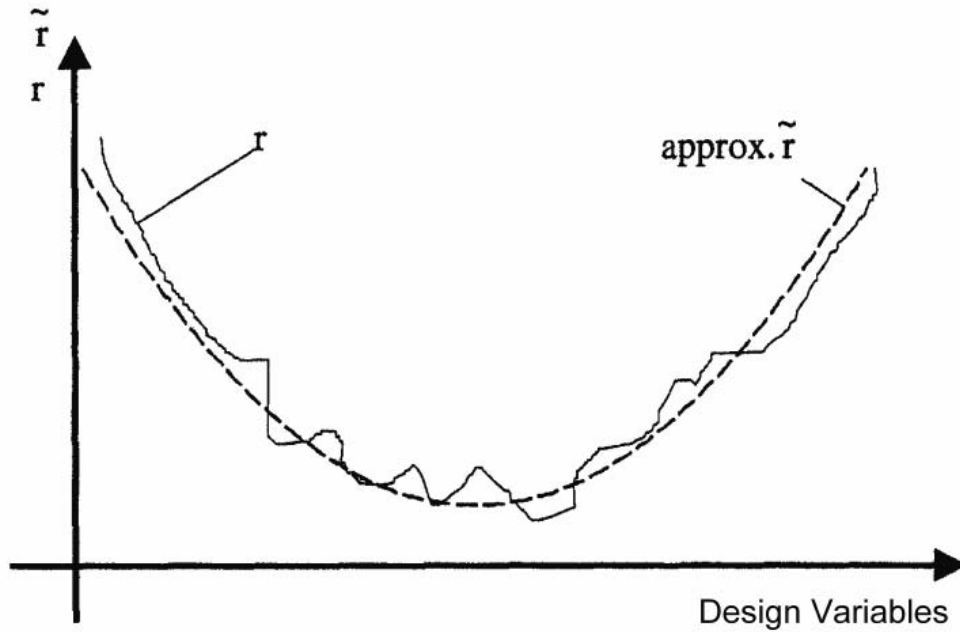
Figure 6.5: Response surface approximation $\tilde{r}$ of the response r

The function $\eta(\mathbf{v}, \boldsymbol{\beta})$ is the sum over a n_β linearly independent functions $\eta_j(\mathbf{v})$ called *regressors*. Each regressor is multiplied by a scalar β_j. The individual regressors are terms of the vector $\eta(\mathbf{v})$:

$$\eta(\mathbf{v}) = \left[\eta_1(\mathbf{v}),\ \eta_2(\mathbf{v}),\ \ldots,\ \eta_{n_\beta}(\mathbf{v})\right]^T$$

The vector $\mathbf{y}$ of size $m \times 1$ contains the response values of the code as interpolation points v^l (with $l = 1 \ldots m$). From equation 6.3 and 6.4 follows:

$$\mathbf{y} = \mathbf{F}\boldsymbol{\beta} + \boldsymbol{\varepsilon}$$

with:

$$\mathbf{F} = \begin{bmatrix} \eta_1(\mathbf{v}^1) & \eta_2(\mathbf{v}^1) & \ldots & \eta_{n_\beta}(\mathbf{v}^1) \\ \eta_1(\mathbf{v}^2) & \eta_2(\mathbf{v}^1) & \ldots & \eta_{n_\beta}(\mathbf{v}^2) \\ \vdots & \vdots & \ddots & \vdots \\ \eta_1(\mathbf{v}^m) & \eta_2(\mathbf{v}^m) & \ldots & \eta_{n_\beta}(\mathbf{v}^m) \end{bmatrix}, \boldsymbol{\beta} = \begin{bmatrix} \beta_0 \\ \beta_1 \\ \vdots \\ \beta_{n_\beta} \end{bmatrix}$$

$$\mathbf{y} = \begin{bmatrix} y1 \\ y2 \\ \vdots \\ y_m \end{bmatrix}, \; \boldsymbol{\varepsilon} = \begin{bmatrix} \varepsilon_1 \\ \varepsilon_2 \\ \vdots \\ \varepsilon_m \end{bmatrix}$$

The vector $\boldsymbol{\varepsilon}$ of size $m \times 1$ contains the *residuals*, i.e. the differences between the predicted response value $\eta(\mathbf{v}^1, \boldsymbol{\beta})$ and the original observation $\mathbf{y}_1$. A least square approach can be applied to calculate an estimation for the regression coefficients minimizing the residual error $\mathbf{e}$. This method is called *linear regression analysis* and is discussed in many statistical texts [86].

It can be demonstrated that the least square approach identifies the regression parameters β by solving a linear system of equations:

$$\beta = \left(\mathbf{F}^T \mathbf{F}\right)^{-1} \mathbf{F}^T \mathbf{y} \tag{6.5}$$

Where $\mathbf{F}^T\mathbf{F}$ is called *information matrix*.

Polynomials of first or second order are used (with or without interaction terms) for RSM approximations. A linear response surface reads:

$$\eta(\mathbf{v}, \boldsymbol{\beta}) \;\; = \;\; \beta_0 + \sum_{i=1}^{n} \beta_i v_i$$

While a quadratic response surface can be expressed as:

$$\eta(\mathbf{v}, \boldsymbol{\beta}) = \beta_0 + \sum_{i=1}^{n} \beta_i v_i + \sum_{i=1}^{n} \sum_{\substack{j=1 \\ j>1}}^{n} \beta_{ij} v_i v_j + \sum_{i=1}^{n} \beta_{ii} v_i^2$$

6.3.2 Design of experiments (DoE)

To determine an approximated response surface, the *interpolation points* must be found. The technique that addresses how to choose the coordinates for the interpolation points is called *design of experiments (DoE)* [87].

While it is important to minimize the number of interpolation points to reduce computational time, it is also important to gather enough information for the response surface to represent adequately the system under investigation.

DoE techniques were actually developed for the analysis of physics experiments, but can also be applied to computational experiment where errors are deterministic.

An *experimental design* consists in a set of m experiments dependent on n input variable v_i, called *factors*. An experimental design is written in matrix form
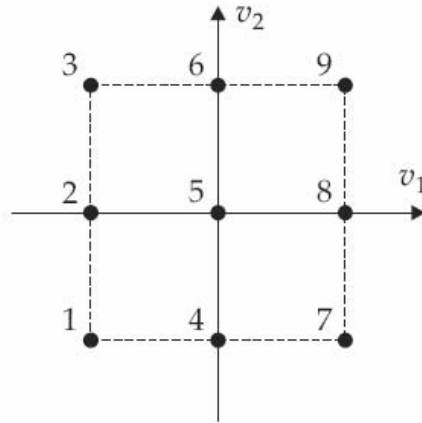
Figure 6.6: Full factorial design 3^2 - two factors varied on three levels

Table 6.1: Design set of a full factorial design 3^2

Point N.	v_1	v_2
1	-1	-1
2	-1	0
3	-1	1
4	0	-1
5	0	0
6	0	1
7	1	-1
8	1	0
9	1	1

$X\,(m \times n)$, where the rows correspond to the individual design points and the columns refer to the factors v_i.

There are many DoE methods and the proper choice of a particular method depends on the type of problem to be analyzed, the intended utilization of the results and additional restrictions, like the maximum acceptable number of interpolation points. Common methods are:

Full factorial design   With this method, the n factors governing the system are varied in a number of predefined l levels, i.e. for every n design variable l levels are sampled. The number of interpolation points is therefore: $N_{IP} = l^n$, e.g. given $n = 2$, $l = 3$, then $N_{IP} = 3^2 = 9$. In this case, if the design space is normalized to the range $[-1,\ 1]$ the design space is sampled as shown in figure 6.6 and table 6.1. An increasing number of factors increases the experimental effort exponentially.

Fractional factorial design   To reduce the number of interpolation points, it is possible to consider a subspace l^{n-p} of the Full Factorial design, with p an non-negative integer number . This method reduces the number of interpolation points, although it is possible that important informations on the system under investigation are lost.

Central composite design   A popular method for fitting polynomials is a combination of a two-level full factorial design (or a fractional factorial design), one *center point*, and a set of so-called *star points*. This method is often used in order to get information for nonlinear relationships between the design variables and the system response for the case that $l = 2$. Fewer interpolation points are needed than with the full factorial design. For $n = 3$, $N_{IP} = l^n + 2 \cdot n + 1 = 15$ interpolation points are needed.

D-optimal   The standard experimental designs discussed before are generally very efficient, but they are not suitable for irregular regions of interest, i.e. that are not a hypercube or a hypersphere.

In the context of this thesis, a method capable to sample an irregular region of interest, due to the presence of several constraints, is required.

In this cases particular optimality criteria, based on the maximization of the information matrix $\mathbf{F}^T\mathbf{F}$ in equation 6.5 have to be used to construct the experimental design. An experimental design is called *D-optimal* if the determinant of the matrix $\mathbf{F}^T\mathbf{F}$ is maximized.

Usually this methods operate by improving a starting design by making incremental changes to its elements. In the coordinate exchange algorithm *cordexch*, implemented in MATLAB [88], the increments are the individual elements of the design matrix.

The design found with this procedure is in general not optimal in a global sense. Yet, it represents the best design that only relies on the selected set.

6.4   Summary

In this chapter the basics of multidisciplinary and multiobjective methods have been introduced. They provide powerful numerical tools to determine the optimum design in complex simulations environments as presented in the extraction system of ELISE. The case of bi-objective optimization has been introduced as it has been used for the optimization of the plasma grid design in this work, described in detail in Chapter 7. The Pareto optimality concept is necessary when the multiobjective optimization method is applied to a problem with conflicting design requirements.

Multidisciplinary optimization allows to incorporate all the relevant disciplines simultaneously. The coupling of all the necessary simulation environments aiming to achieve a better design is further discussed in chapter 7.

Chapter 7

MDO applied to the plasma grid

7.1 Introduction

The iterative approach is the most common in engineering and has been valuable in the design phase of ELISE for its relative simplicity and flexibility. However, not all the possible geometry modifications of the grids could be compared using all the available FE models because of the limited time and the need to operate manually each iteration and each design change. As the amount of variables increases, the iteration number increases as well. Investigating the hundreds of design possibilities becomes very time-intensive because the search for the best result requires a long sequence of design comparisons.

As described in chapter 4, several aspect of the design of the plasma grid of ELISE have been studied with the use of FE models to simulate electrical and magnetic fields as well as evaluate the mechanical stresses. The mechanical analyses have shown presence of stress concentrations and further modifications of the PG geometry have been necessary. In addition a review of the electro-magnetic analysis was necessary to evaluate the new FF resulting from the last geometry modifications. This iterative optimization work has been repeated a few time, until the PG design was considered satisfactory, as reported in chapter 4.

An automated approach can be adopted for the optimization of the PG of ELISE. Indeed, the task of optimizing the plasma grid owns the characteristic of being both a multidisciplinary and multi-objective problem. An automated method has advantages with regard to velocity of execution and "objective" search for the optimum solution, that is independent from the engineer judgment. Nevertheless, to implement an automated approach, the problem has to be defined formally and the results must be evaluated accordingly.

Not only a vast number of design variables and disciplines can simultaneously be considered within a reasonably short amount of time in the design process,

the flexibility and rationality of the designers should also be employed to ensure practicality of the design solution.

The models needed for the analyses of the PG have been adapted to this approach and several aspects have been taken into account, e.g. reduced computational time, numerical accuracy, correct evaluation of results.

In the next sections the optimization routine, the plasma grid FE models and the results will be discussed in detail.

7.2 The optimization problem

The goal of the design task is to find the Pareto set that defines the optimum design solutions aiming at minimizing both the filter field inhomogeneity and the mechanical stresses in the plasma grid simultaneously. The behavior of the plasma grid is simulated by means of a series of ANSYS models and the various design solutions have been compared using the MATLAB suite as described later in section 7.2.1. The plasma grid shape is represented by a simplified model described in section 7.2.2 and is subject to geometrical constraints. The electro-magnetic and mechanical models are subject to loads and boundary conditions defined in sections 7.2.3, 7.2.4 and 7.2.5.

7.2.1 The ANSYS-MATLAB routine

The automated optimization has been performed using the commercial Finite Element Analysis software ANSYS [69] and the numerical computing environment MATLAB [89].

Modeling and simulation of the PG has been conducted in ANSYS using parametric models. A "bottom-up" modeling technique has been adopted to provide a robust tool for the systematic modifications of the geometry required by the shape optimization. During each function evaluation ANSYS is executed in batch-mode to determine the values of the performance measures based on the input design variables.

Each model consists of three parts:

- Preprocessing phase, consisting of geometry creation, meshing, definition of loads and boundary conditions

- Solving

- Post-processing.

The ANSYS analysis is structured in two branches:
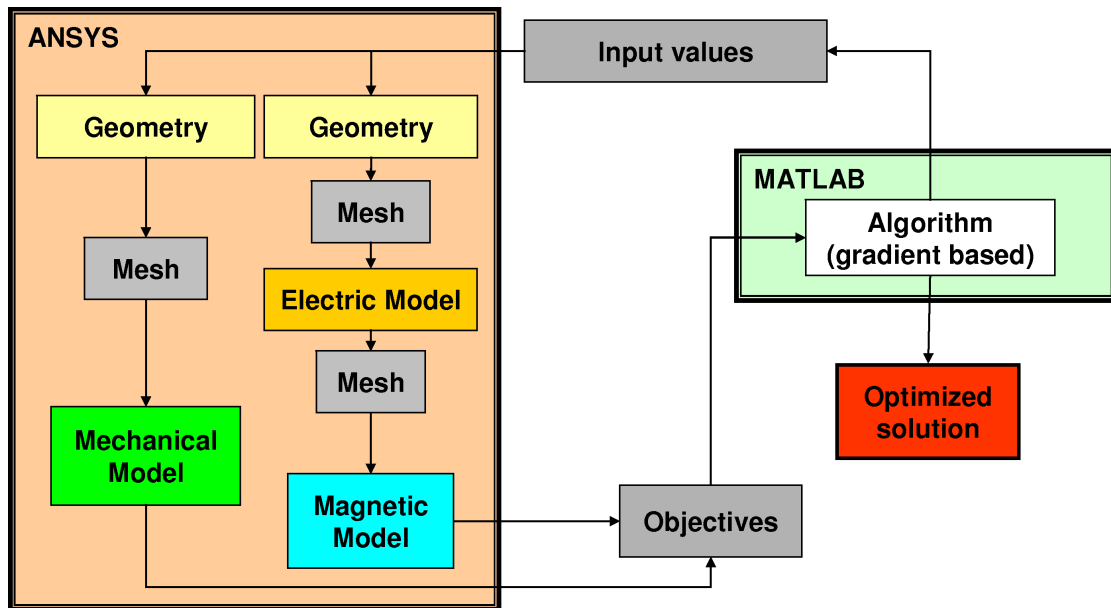
Figure 7.1: Diagram of the routine used for the optimization of the plasma grid of ELISE

Electromagnetic analysis: consists of a *load transfer* coupled physics analysis where electric current and magnetic fields are calculated sequentially. The *electric model* is used to calculate the electric current distribution that is provided as input for the *magnetic model*. Each model has its own geometry and mesh.

Mechanical analysis: consists of a single model where mechanical stresses are determined.

These models are described more in detail in the following sections.

The results from the ANSYS models are returned to MATLAB and evaluated by an algorithm. For computational efficiency a gradient-based search technique is employed using the *fmincon* function from MATLAB [83]. Firstly an estimate, or start value, of the design variables is passed to the ANSYS models. ANSYS then returns the results, representing the objective functions to MATLAB. The algorithm iterates the calculations with slightly different values of the design variables to explore the design space and determine the local gradient of the objective function. Then a "step" in one direction in the design space is made and a new evaluation is performed. The iterations stop when the convergence criteria, based on residuals of the objective function, are met.

A weighted sum method is applied to this research as described in chapter 6.2 to obtain the curve of optimum designs by generating a Pareto frontier with several

optimum design points. Figure 7.1 shows a diagram of the routine implemented.

The number of iterations needed to find a Pareto point is in the order of 100. It is crucial to assure a fast solution time, in the order of one minute, for each solving iteration, so that a sufficient amount of points of the Pareto Frontier, say 10, can be found in a reasonable amount of time. Solving time can be reduced with an appropriate simplification of the model. In the following section the model of the grid geometry is described in detail.

7.2.2   Plasma grid geometry

A low computational time, in the order of 1 minute per iteration, is crucial for an automated optimization because hundreds of iterations are needed to obtain the solution. The aspects that affect significantly the solving time is the number of nodes and elements used for the discretization of the model. The amount of elements depends on the model geometry and the mesh density. Small features like a fillet or a short edge require a higher mesh density to accurately solve the model. In general geometries with a larger ratio between model dimension and smallest edge length require a higher number of nodes and elements.

The PG geometry resulting from the study reported in chapter 4 has been used as a starting geometry for this optimization. Therefore the design comprises also the pockets introduced to improve the FF homogeneity.

For this study the grid geometry has been reduced to the smallest possible section of the plasma grid taking advantage of symmetry planes. In this way a very small section of the PG, dimensions 80 mm $\times$ 10 mm $\times$ 9 mm, could be isolated. This model, shown in figure 7.2 still contains all the relevant geometrical features for this study like water manifolds, cooling channels, extraction apertures and pockets.

A set of 10 geometrical variables have been defined as shown in figure 7.2. These variables are related to shape and position of water manifolds and the pocket. Shape and dimension of extraction apertures are not considered as design variables as their modification would have a more complex effect on the negative ion source performance. In fact aperture geometry influences negative ion production, extraction, ion optics, co-extraction of electrons and it is currently not possible to take into account these effects. Taking this into account would make the model too complex.

To reduce computational time it is also important to reduce mesh density and a compromise has to be found with the numerical accuracy. This is discussed in the next three sections together with the most relevant characteristics of the FE models.
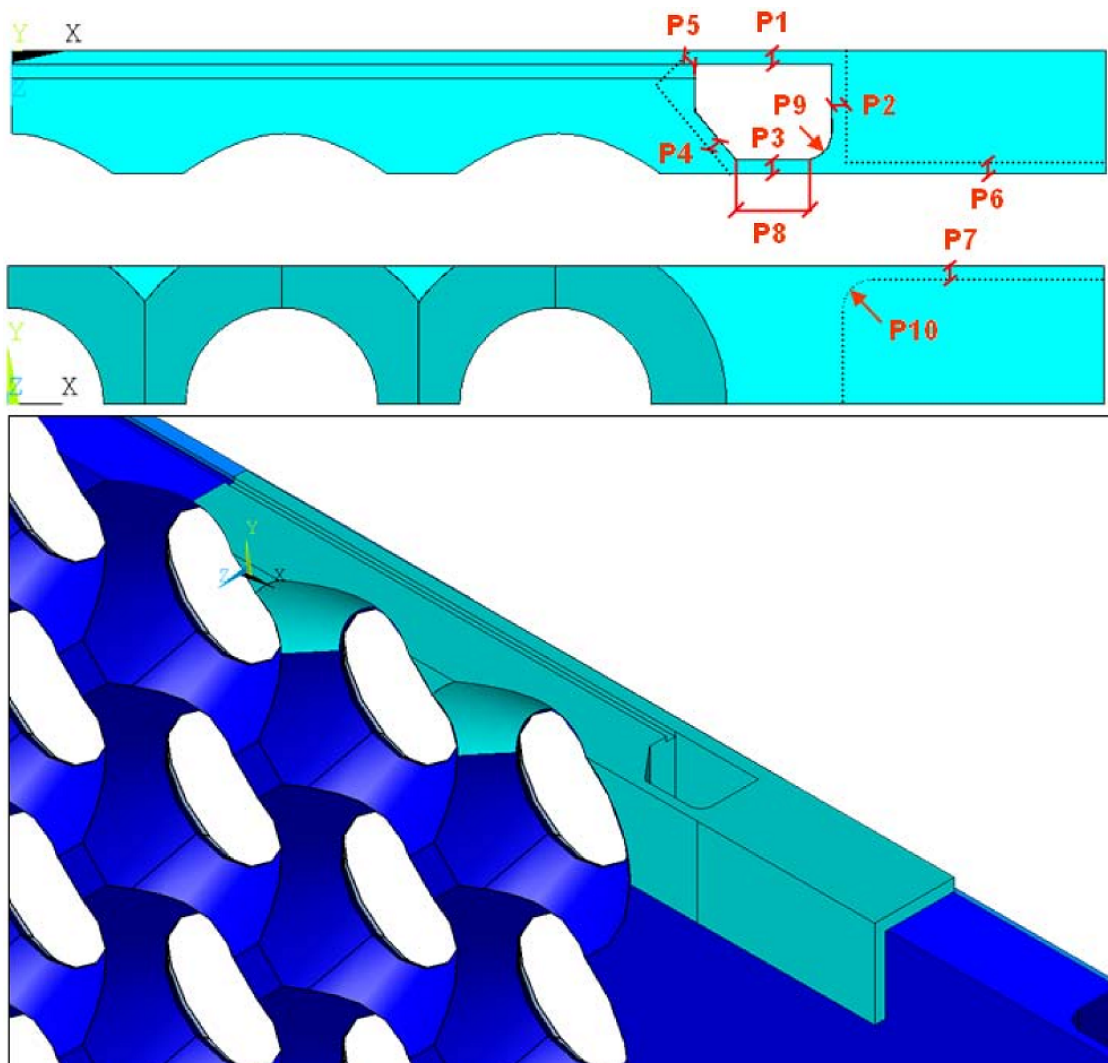
Figure 7.2: Geometry for the optimization of the plasma grid of ELISE

7.2.3 Thermal-electric model

Using the geometry described in section 7.2.2 a thermal-electric model of the PG has been created. The geometry has been meshed with a 5000 nodes model with linear elements to allow a solving time of approximately 10 s. Electric and thermal properties of OFHC[1] and galvanic copper have been defined.

The following boundary conditions and loads have been defined:

- Electric boundary conditions:

    - The Voltage value of the nodes in the lower part of the model (at $y = 0$ mm) has been set to 0.

    - The Voltage value of the nodes in the upper part of the model (at $y = 0.01$ mm) has been coupled.

- Electric loads

    - A current of 100 A has been fed to the upper side of the model, representing 8 kA for the whole PG width.

- Thermal boundary conditions:

    - Heat transfer coefficient on the inside surface of the cooling channels (cf. chapter 5): where the Nusselt number Nu is calculated with the Sieder-Tate correlation (without viscous factors):

$$\mathrm{Nu} = 0.027 \, \mathrm{Re}_D^{4/5} \, \mathrm{Pr}^{1/3}$$

    where Re and Pr are the Reynolds and the Prandtl number respectively.

- Thermal loads:

    - Heat load of $20 \, \mathrm{kW/m^2}$ on the plasma side of the PG to take into account the heat caused by the plasma, experimentally determined [90].
    - Joule heating caused by the strong PG current.

No definition of symmetry conditions, e.g. on the lateral sides of the PG model, is necessary for both thermal and electric models. No definition of boundary conditions corresponds to adiabatic surfaces (for the thermal model) or zero current perpendicular to the surface (for the electric current model), thus fulfilling the requirements for symmetry.

---

[1]OFHC: Oxygen Free High Conductivity copper
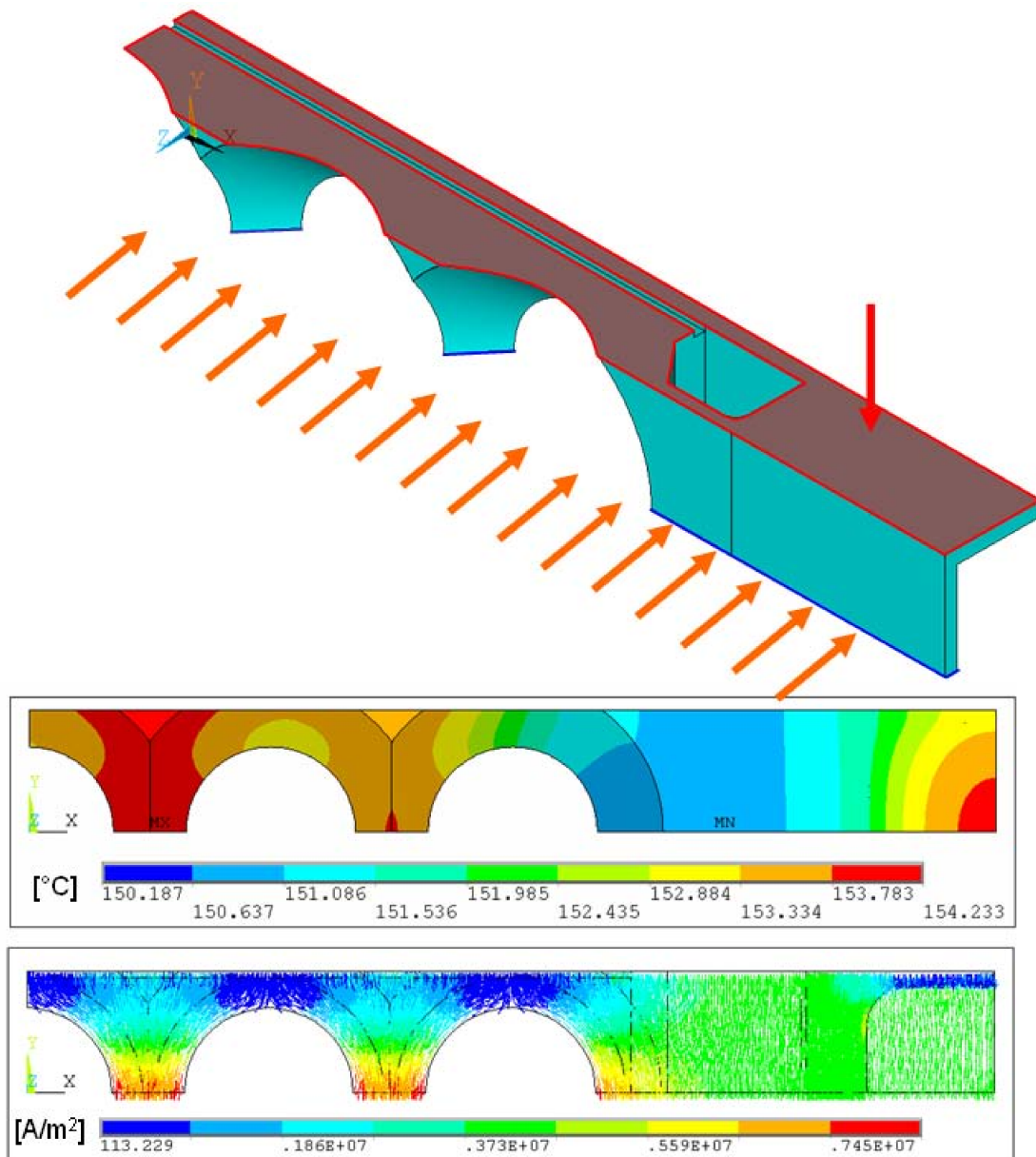
Figure 7.3: Thermal-electric model for the optimization of the plasma grid of ELISE. Top: boundary conditions, middle: temperature distribution, bottom: current density distribution

Preliminary results, illustrated in figure 7.3, show that the temperature distribution in the PG model is quite uniform, with a $\Delta T < 5\,°C$, indicating that the electric resistivity of the material is relatively uniform. For this reason and to simplify the ANSYS modeling for the optimization routine, the thermal analysis is not performed during the optimization process. The electric current distribution is calculated considering a uniform temperature distribution of 150°C in the PG model. The current distribution is then saved for the next step, the magnetic model, in order to complete the analysis of the FF uniformity.

7.2.4   Magnetic model

The geometry described in section 7.2.2 is expanded to allow the analysis of the magnetic field generated by the PG current. In particular the spaces inside and around the PG on the plasma side and on the beam side have been modeled.

The geometry has been meshed with 30000 nodes with linear elements. The resulting solving time is approximately 40 s. Magnetic properties of OFHC and galvanic copper have been defined.

The following boundary conditions have been defined:

- Magnetic model, boundary conditions:

    - Symmetry conditions:

        * Parallel magnetic field on the upper and lower horizontal surface of model (shown in green in figure 7.4).
        * Orthogonal magnetic field on the lateral sides of the model (shown in light blue in figure 7.4).

    - Infinite conditions in the front and back sides of the model. This condition is used to simulate the decrease to zero of the magnetic field at an infinite distance, but still using a FE model of finite dimension.

- Magnetic model, loads:

    - The only load is represented by the electric current distribution calculated as calculated in section 7.2.3. The results from the electric model have been interpolated and applied to the mesh of the magnetic model.

This model provides the first performance measure for the multiobjective optimization: the FF uniformity. To quantify the FF uniformity the B_x component (which is the horizontal component) of the magnetic field has been evaluated in a surface parallel to the PG, at 20 mm distance from the grid, as shown in figure 7.4, in direction of the plasma. In this surface the standard deviation of the B_x
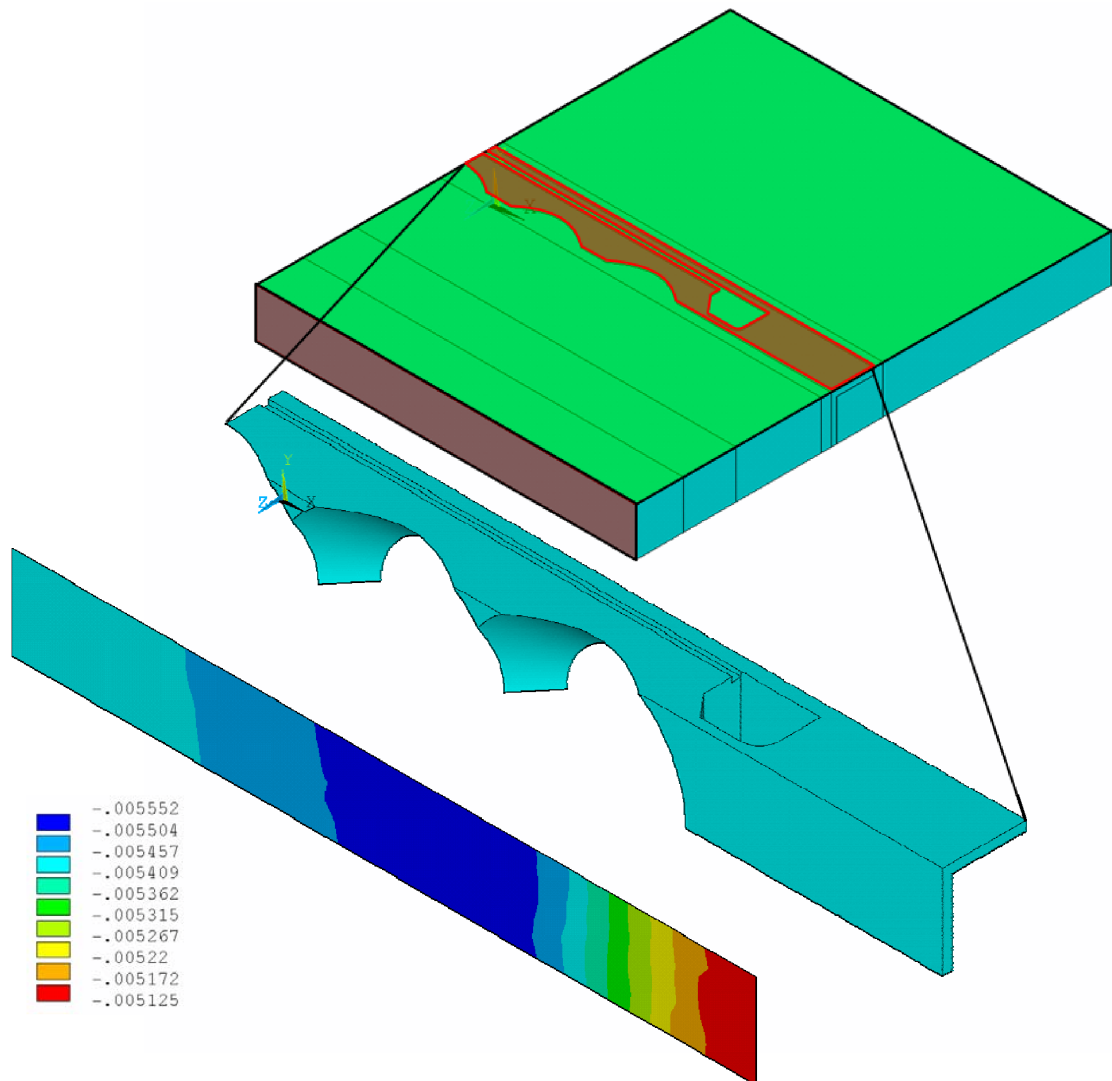
Figure 7.4: Magnetic model for the optimization of the plasma grid of ELISE. Top: Boundary conditions. Bottom: The magnetic field component B_x [T] is plotted in the surface at 20 mm from the plasma grid

component has been calculated and used as the performance measure for the FF uniformity:

$$\mathrm{J}_1 = \sigma_{B_x} = \sqrt{\iint \left[B_x(x,y) - \langle B_x \rangle\right]^2 dxdy}$$

7.2.5   Mechanical model

Finally a the geometry described in section 7.2.2 has been used for the analysis of the structural behavior of the PG model.

The geometry has been meshed with 40k nodes with linear elements. The resulting solve time is approximately 50 s. Mechanical properties of OFHC and galvanic copper have been defined as linear properties.

The following boundary conditions have been defined:

- Mechanical model, boundary conditions:

  - Symmetry and periodic conditions shown in figure 7.5:
    * Fixed x position of nodes in the right face of the model geometry (shown in blue on the right lateral face in figure).
    * Left side of the model face parallel to the right face. (shown as a blue line on the left side of the model).
    * Fixed y position of nodes in the bottom face of the model geometry (shown by the lower red arrow).
    * Top side of the model parallel to the bottom face of the model geometry (shown by the upper red arrow).

- Mechanical model, loads:

  - The water pressure of 30 bar has been applied on all the internal faces of the cooling channel and manifold section.

This model provides the second performance measure for the multiobjective optimization: the mechanical stresses.

The Von Mises stresses have been evaluated on the external surfaces of the PG, as shown in figure 7.4 and this represents the performance measure $\mathbf{J}_2$. From a preliminary calculation it can be seen that the most critical areas are concentrated around the water manifold.

The assessment of the mechanical stresses has been limited to the PG surface to simplify the evaluation of the results from the FEM analysis. Higher stresses can be expected on the inside faces of the water manifold due to the presence
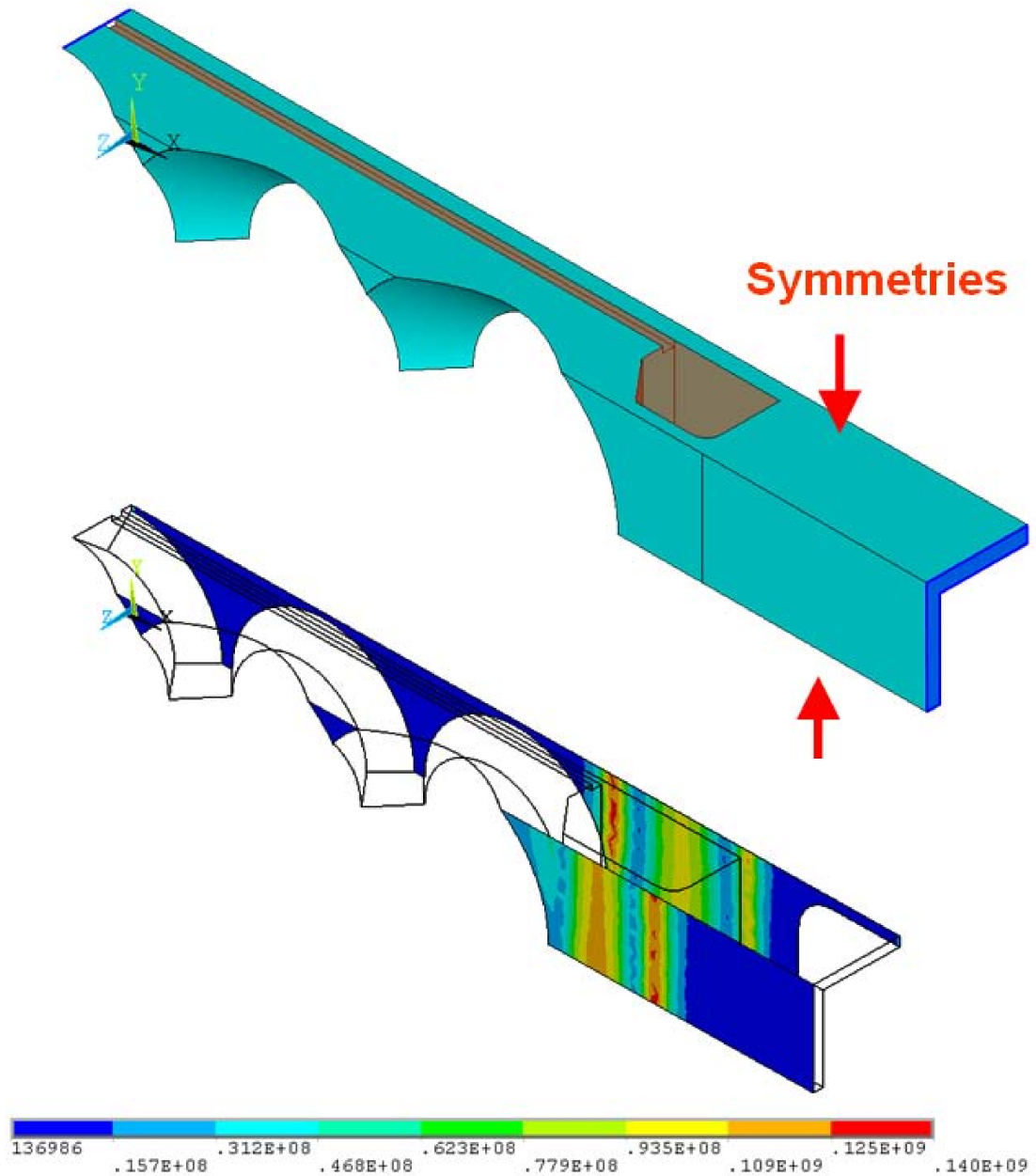
Figure 7.5: Mechanical model for the optimization of the plasma grid of ELISE. Top: boundary conditions. Bottom: surface stresses are evaluated on the Plasma side and on the downstream side.

of sharp corners. However the evaluation of mechanical stress in such corners is difficult with the FE method, because many times the numerical calculation of these corners results in mathematical singularities.

On the other hand the presence of sharp corners in a FE model does not correspond to the geometry of the real object. Ideally sharp edges or corners can never be achieved by machining and even the sharpest edges will always have a small but measurable radius. The same is valid for a corner.

It is therefore possible to model the corners on the inside of the water channel and manifold in the PG model using small radii in a way that closely resembles the real geometry of the grid. In doing so the singularities are also removed and the FE model can deliver a very accurate evaluation of the stress field.

Nevertheless this approach requires a very large mesh due to the resulting high ratio between larger and smaller edge dimension. This leads to a too large solving time (in the order of 10 min. for the mechanical model only) compared with the requirements of this multiobjective optimization as defined in section 7.2.1.

7.3   The optimization task

The optimization task reads as follows:

$$
\begin{aligned}
&min\ \mathbf{z}(\mathbf{x}) = [J_1(\mathbf{x}),\ J_2(\mathbf{x})]\\
&with : \mathbf{x} = [p_1,\ p_2,\ p_3, \ldots, p_{10}]\\
&subject\ to :\\
&g_1(\mathbf{x}) \;=\; -tan(\alpha) \cdot p_1 + p_2 - sin(\alpha) \cdot p_3 + \sqrt{2} \cdot tan(\alpha) \cdot p_4\\
&\qquad\qquad +11.4 \times 10^{-3} - 2.5 \times 10^{-3} \cdot tan(\alpha) \leq 0\\
&g_2(\mathbf{x}) \;=\; p_1 + p_3 - 6.9 \times 10^{-3} \leq 0\\
&g_3(\mathbf{x}) \;=\; p_7 - 6.9 \times 10^{-3} \leq 0\\
&g_4(\mathbf{x}) \;=\; p_2 - tan(\beta) \cdot p_3 + 1/cos(\beta) \cdot p_4 + p_8 + 130.9 \times 10^{-3} \leq 0\\
&g_5(\mathbf{x}) \;=\; -tan(\alpha) \cdot p_1 + p_3 - 1/cos(\alpha) \cdot p_4 + \sqrt{2} \cdot tan(\alpha) \cdot p_5\\
&\qquad\qquad -6.4 \times 10^{-3} - 2.5 \times 10^{-3} \cdot tan(\alpha) \leq 0\\
&g_6(\mathbf{x}) \;=\; (1 + tan(\alpha)) \cdot p_1 - 1/cos(\alpha) \cdot p_4 - \sqrt{2} \cdot tan(\alpha) \cdot p_5\\
&\qquad\qquad -1.4 \times 10^{-3} - 2.5 \times 10^{-3} \cdot tan(\alpha) \leq 0\\
&g_7(\mathbf{x}) \;=\; 45 \times 10^{-6} - cos(\alpha) \cdot 9 \times 10^{-3} \cdot p_4 + (sin(\alpha) \cdot cos(\alpha))/2 \cdot p_4^2\\
&\qquad\qquad -9 \times 10^{-3} \cdot p_8 - 9 \times 10^{-3} \cdot p_9 + (1 - \tfrac{\pi}{4}) \cdot p_9^2 + p_8 \cdot p_1 + p_9 \cdot p_1\\
&\qquad\qquad +p_4 \cdot cos(\alpha) \cdot p_1 + p_8 \cdot p_3 + p_9 \cdot p_3 + p_4 \cdot cos(\alpha) \cdot p_3 \leq 0
\end{aligned}
$$

$$(7.1)$$

and :
$$1 \times 10^{-3} \text{ m} \leq p_1 \leq 2 \times 10^{-3} \text{ m}$$
$$1 \times 10^{-3} \text{ m} \leq p_2 \leq 10 \times 10^{-3} \text{ m}$$
$$1 \times 10^{-3} \text{ m} \leq p_3 \leq 5 \times 10^{-3} \text{ m}$$
$$1 \times 10^{-3} \text{ m} \leq p_4 \leq 2 \times 10^{-3} \text{ m}$$
$$1 \times 10^{-3} \text{ m} \leq p_5 \leq 2 \times 10^{-3} \text{ m}$$
$$1 \times 10^{-3} \text{ m} \leq p_6 \leq 8 \times 10^{-3} \text{ m}$$
$$1 \times 10^{-3} \text{ m} \leq p_7 \leq 8 \times 10^{-3} \text{ m} \quad (7.2)$$
$$1 \times 10^{-3} \text{ m} \leq p_8 \leq 10 \times 10^{-3} \text{ m}$$
$$1 \times 10^{-3} \text{ m} \leq p_9 \leq 2 \times 10^{-3} \text{ m}$$
$$1 \times 10^{-3} \text{ m} \leq p_{10} \leq 2 \times 10^{-3} \text{ m}$$
with :
$$\alpha = 50°$$
$$\beta = 40°$$

The linear constraints represented by equations g_1, g_2, ... to g_6 and the lower and upper bounds of each variable in equations 7.2 limit the design space to plasma grid shapes with same topology. In this way the variables can be changed continuously, as required by the gradient-based algorithm. The non-linear constraint g_7 represents the minimum value for the area of the water manifold cross section.

Reference design The reference design for the optimization problem consists of values of the design variables defined after the study described in chapter 4. These values constitute the starting inputs for the optimization procedure:

$$
\begin{aligned}
p_1 &= 1.5 \times 10^{-3} \text{ m} \\
p_2 &= 1.54 \times 10^{-3} \text{ m} \\
p_3 &= 1.2 \times 10^{-3} \text{ m} \\
p_4 &= 1.24 \times 10^{-3} \text{ m} \\
p_5 &= 1.21 \times 10^{-3} \text{ m} \\
p_6 &= 1.1 \times 10^{-3} \text{ m} \quad (7.3) \\
p_7 &= 2.5 \times 10^{-3} \text{ m} \\
p_8 &= 4.8 \times 10^{-3} \text{ m} \\
p_9 &= 2 \times 10^{-3} \text{ m} \\
p_{10} &= 2 \times 10^{-3} \text{ m}
\end{aligned}
$$
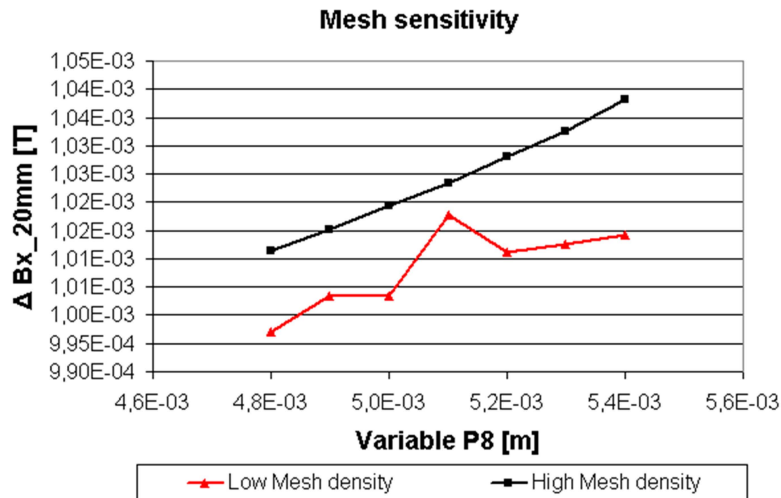
Figure 7.6: Sensitivity of the performance measure J_2 (filter field non-homogeneity) for two mesh densities.

7.4 Results

Preliminary results of the Pareto front evaluation have shown how the numerical noise produced by the FE models leads to convergence issues of the gradient based algorithm. This is due to a non-smooth response of the computer experiments cause by the relatively coarse mesh. The RSM method has therefore been applied to the analyzed system with D-optimality criteria for the determination of the interpolation points.

7.4.1 Numerical Accuracy

The gradient based algorithm implemented in MATLAB searches for the optimum value of a function assuming that the objective function is a smooth function.

For a low mesh density it can happen that a performance evaluation does not behave monotonically with respect to a variable change. This is the case for the output of the ANSYS Models used for the multidisciplinary optimization described in this chapter, as it is exemplified in figure 7.6. The output of the FF performance measure is plotted against one of the design variables for two mesh densities. The coarse mesh produces an output affected by numerical noise that generates a false local minimum, that in turn can mislead the gradient based optimization algorithm. The finer mesh produces a smoother output.

The numerical noise caused by the coarse mesh can be therefore reduced by increasing the mesh density. In the example shown in figure 7.6 the number of nodes has been increased by a factor 10. The required computational time increases

more than proportionally with the number of nodes. This is impractical for an automated optimization, due to the required fast execution time of each iteration step. The problems due to numerical noise can be removed using a surrogate model.

7.4.2 Response surface model

The RSM technique described in section 6.3 has been applied to the case study discussed in this chapter to solve the problems related to numerical noise and to keep the computational time reasonably short.

To reduce the computational effort the number of design variables has been reduced to 8, fixing the value of the radii represented by the two variables P8 and P9, shown in figure 7.2, to 2 mm. The design space has been evaluated using 3000 interpolation points distributed according to the D-optimal design technique (cf. section 6.3.2). Each evaluation lasts approximately 60 s. The response surface has then been generated interpolation the outputs for the two performance measures (FF homogeneity and mechanical stresses), calculated at the interpolation points, with a polynomial function with quadratic, interaction and linear terms. This function has then been used to generate the Pareto front with the gradient based algorithm *fmincon*.

7.4.3 Pareto front

The Pareto front resulting from the RSM study is shown in figure 7.7. It can be seen that relatively to the start geometry a considerable improvement can be obtained in terms of FF uniformity or mechanical stresses in the PG. In particular 50% lower maximum Von Mises stress value can be achieved for equivalent FF uniformity. Otherwise 50% lower FF inhomogeneity can be achieved for equivalent maximum Von Mises stresses. The shape of the Pareto front confirms that the the two objective functions represent contrasting requirements.

Pareto Front
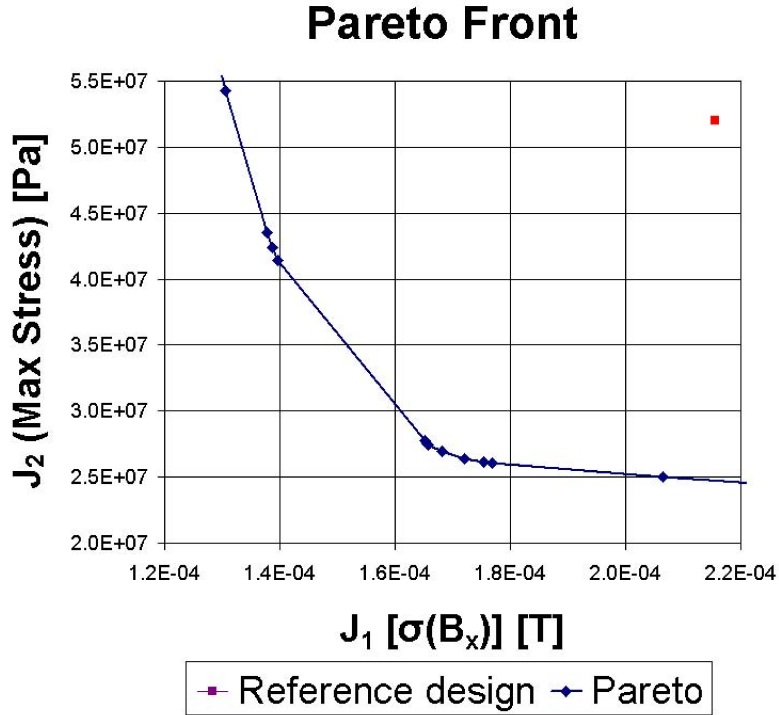
Figure 7.7: Result of Pareto study for the optimization of the PG of ELISE. The blue line corresponds to the Pareto Set. The red point represents the start geometry for the automated optimization, output of the study discussed in Chapter 4.

The design variable vector for the solution with minimum J_1 (FF non-uniformity) is:

$$
\begin{aligned}
p_1 &= 1.00 \times 10^{-3}\,\text{m} \\
p_2 &= 1.00 \times 10^{-3}\,\text{m} \\
p_3 &= 1.00 \times 10^{-3}\,\text{m} \\
p_4 &= 2.00 \times 10^{-3}\,\text{m} \\
p_5 &= 1.00 \times 10^{-3}\,\text{m} \\
p_6 &= 1.00 \times 10^{-3}\,\text{m} \\
p_7 &= 1.00 \times 10^{-3}\,\text{m} \\
p_8 &= 3.41 \times 10^{-3}\,\text{m}.
\end{aligned}
\tag{7.4}
$$

As it could be expected intuitively, the results show that a low FF non-uniformity requires reduced wall thickness to limit the electric current in the grid material around the apertures.

The design variable vector for the solution with minimum J_2 (mechanical stresses) is

$$\begin{aligned}
p_1 &= 1.52 \times 10^{-3} \text{ m} \\
p_2 &= 6.41 \times 10^{-3} \text{ m} \\
p_3 &= 1.70 \times 10^{-3} \text{ m} \\
p_4 &= 1.00 \times 10^{-3} \text{ m} \\
p_5 &= 2.00 \times 10^{-3} \text{ m} \\
p_6 &= 1.00 \times 10^{-3} \text{ m} \\
p_7 &= 6.90 \times 10^{-3} \text{ m} \\
p_8 &= 5.34 \times 10^{-3} \text{ m.}
\end{aligned} \tag{7.5}$$

As expected, the results show that for minimum mechanical stresses wall thicknesses must be increased.

Apart from the two extreme cases, a number of other solution can be found by means of intermediate priority settings. These solutions represent compromises between the two conflicting requirements.

The optimized plasma grid geometries for the extremes of the Pareto solutions, for maximum FF homogeneity and minimum mechanical stresses, are shown in figure 7.8a and 7.8b respectively. An intermediate solution is shown in 7.8c.

7.5   Summary

Multidisciplinary bi-objective optimization of the plasma grid design for the ELISE source has been implemented using a small model of the grid. Electrical, magnetic and mechanical models have been generated using appropriate loads and boundary conditions, and using meshes with a small amount of nodes and elements in order to limit computational time, while keeping enough numerical accuracy. The Pareto front obtained from the optimization consists of a set of design solutions that considerably decrease the two performance measures with respect to the start design, that consists of the design obtained from the analyses described in chapter 4. At the extremes of the Pareto front, it is possible either to reduce FF inhomogeneity by 50% or mechanical stresses by 50%. The automated optimization process has therefore delivered a substantial improvement of the plasma grid design.
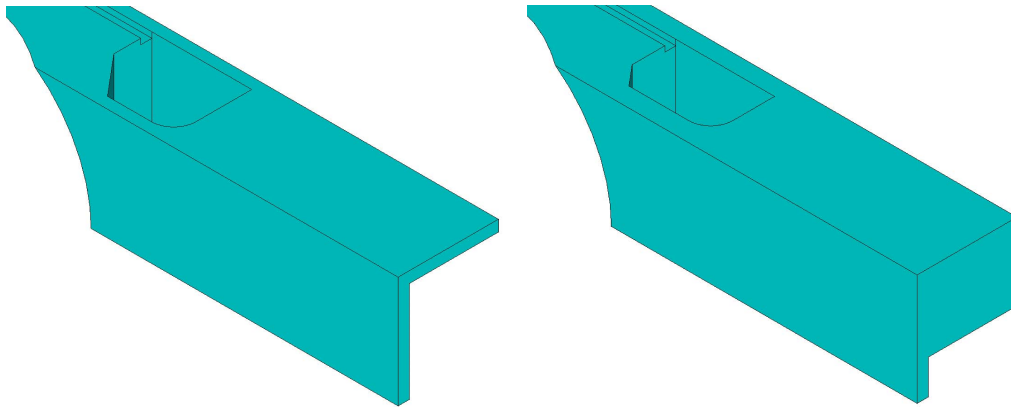
(a) PG shape for maximum FF uniformity

(b) PG shape for minimum mechanical stresses
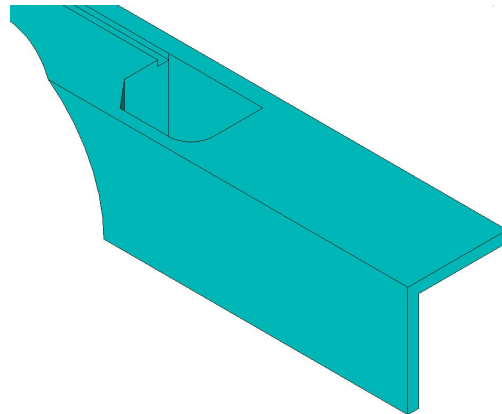
(c) PG shape for maximum FF uniformity and minimum mechanical stresses

Figure 7.8: Optimized plasma grid shapes for the extremes of the Pareto Set (a and b) and for an intermediate solution (c).

Chapter 8

Conclusions

This thesis describes the optimization processes for the complex engineering problem represented by the extraction system for ELISE applying several computational techniques. The new large negative-ion source of the ELISE testbed is a complex environment with interacting magnetic fields, ion beams, electron trajectories, mechanical structures. The analysis of specific issues of the extraction system of ELISE, like filter field homogeneity, heat loads on the extraction grid, and mechanical stresses on both plasma and extraction grid, required the use of several modeling techniques. Ray-Tracing codes to determine ion and electron trajectories, as well as CFD and FEM codes, have been applied. A set of optimization works has been performed, both manual and automated, to improve the design of the plasma grid and the extraction grid of ELISE. Several design solutions have been compared. The results of the various topics of the work are listed below:

Plasma grid

- The cooling circuit has been optimized to reduce pressure losses and increase temperature uniformity on the surface of the grid. The cooling circuit design with vertical manifolds between the beamlet groups was proven beneficial for the plasma grid temperature distribution.

- The introduction of pockets in the grid in the areas in between the beamlet groups has further reduced the PG current flow in that area, with the effect to generate a more uniform FF in front of the plasma grid. In addition, the PG current flowing in the beamlet groups, in the grid material around the extraction apertures, has increased the FF in front of the grid by 50%. A residual ripple in the filter field remains in front of the plasma grid caused by the presence of the extraction apertures. This is inevitable if the filter field is produced by the PG current.

- The influence of the EDF on the magnetic field at 2 mm from the grid surface has been analyzed. Two configurations of FF and EDF, orthogonal and parallel have been compared. The orthogonal configuration has been found to be more favorable because it does not produce any zero-field region in front of the extraction apertures.

- Mechanical analyses of the most critical areas of the plasma grid have been conducted and the design has been verified, using criteria derived by dedicated galvanic copper tests. In a few cases, the design had to be modified, for example, by increasing the wall thickness of the grid, without a significant change in the resulting FF.

Extraction grid

- To determine the power load deposition on the extraction grid surface caused by co-extracted electrons, the ion beam and the electron trajectories extracted from an aperture of the extraction system of ELISE have been simulated. The calculations have been performed by R. Gutser using the codes KOBRA3 and Etron [70].

- A 2 Dimensional local model of the extraction grid has been created to compare various cooling channel geometries with the ITER reference design. Considering design and manufacturing constraints an optimal 3-channel geometry has been identified.

- The 3-channels geometry has been adapted to the real geometry of the extraction grid and several solutions have been applied to cool down most of the area of the grid, to reduce pressure losses and to assure a uniform water flow in the many cooling channels.

- CFD simulations have been performed to evaluate heat transfer coefficients and flow uniformity in the extraction grid cooling circuit. Conjugate heat transfer has been used to evaluate the efficiency of the cooling channels with respect to the heat removal.

- Thermo-mechanical calculations have been performed on the basis of the temperature field resulting from the conjugate heat transfer analyses. Mechanical stresses and deformations have been calculated by means of FEM models representing a portion of the grid.

- The ELISE design has been compared to the ITER-SINGAP reference design. In addition, the two configurations of EDF with respect to FF, orthogonal and parallel, have been compared. Consistent performance improvements have been achieved with the ELISE design in all relevant parameter

with respect to maximum grid temperature increase, maximum cooling channel temperature increase, maximum mechanical stresses and deformation for both magnetic field configurations:

- For the orthogonal configuration of EDF and FF, the ELISE design of the EG cooling circuit provides 29% and 14% lower maximum grid temperature and maximum cooling channel temperature, respectively, compared to the ITER-SINGAP reference design. The grid bowing is reduced by 71% and the mechanical stresses by 50%.

- For the parallel configuration, the figures are 16% and 13% reduction of maximum grid temperature and maximum cooling channel temperature, while the grid bowing and mechanical stresses are reduced by 4% and 17%, respectively.

Multidisciplinary optimization of plasma grid

- A MATLAB routine, coupled with several ANSYS models, has been set up to apply the multidisciplinary optimization method to the plasma grid design. A simplified geometrical model of the grid and a set of electric, thermal, magnetic and mechanical FEM models have been defined taking into account the relevant aspects of the PG design.

- In the optimization routine 10 geometrical variables have been identified and two performance measures (the objective functions) have been defined. The two objective functions are the FF uniformity and mechanical stability of the grid. They represent conflicting requirements. Therefore, a unique optimum solution does not exist. The bi-objective optimization leads to the determination of a Pareto front, representing the set of optimum solutions.

- The response surface method was used to solve the problem of numerical noise present in the FE models of the plasma grid.

- The Pareto front obtained from the multidisciplinary bi-objective optimization resulted in a set of design solutions that considerably improve the start design. This consisted of the design obtained from the analyses described in chapter 4. It is possible to reduce either FF inhomogeneity by 50%, at same mechanical stress level, or mechanical stresses by 50%, with the same FF homogeneity.

The plasma and extraction grids for ELISE are currently being manufactured based on the design defined in chapters 4 and 5. The improvement resulting from the MDO analysis described in chapter 7 could not be applied, because the

manufacturing phase of the PG for ELISE was already started. Having said that, the results of the multidisciplinary optimization can be used for a future set of plasma grid segments for ELISE.

Outlook   How the electric and magnetic fields interact with the generation and extraction of negative ions and influence electron co-extraction is currently subject of an intense research activity at IPP. Although remarkable results have been achieved recently [91], 2D and 3D plasma modeling is at the moment limited by the large amount of computational resources required by PIC codes.

As CPU speeds and memory capacities increase for equal costs and optimization algorithms are refined and increase their performances, it will be possible to include PIC codes and ion beam optics in the optimization process. The number of variables that the optimization routine will have to manage will increase and MDO techniques will be a fundamental tool to incorporate all the disciplines simultaneously.

Bibliography

[1] H. Craig, "Standard for reporting concentrations of deuterium and oxygen-18 in natural water," *Science*, vol. 133, pp. 1833–1834, 1961.

[2] C. L. Smith and D. Ward, "The path to fusion power," *Philosophical Transactions of the Royal Society A: Mathematical, Physical and Engineering Sciences*, vol. 365, no. 1853, pp. 945–956, 2007.

[3] J. Ongena and G. Van Oost, "Energy for future centuries: will fusion be an inexhaustible, safe, and clean energy source?," *Fus. Sci. and Tech.*, vol. 45, no. 2T, pp. 3–14, 2004.

[4] "JET - europe's largest fusion device." `http://www.jet.efda.org`.

[5] "ASDEX Upgrade." `http://www.ipp.mpg.de/ippcms/eng/for/projekte/asdex/index.html`.

[6] "ITER - the way to new energy." `http://www.iter.org`.

[7] R. Hemsworth, H. Decamps, J. Graceffa, B. Schunke, M. Tanaka, M. Dremel, A. Tanga, H. de Esch, F. Geli, J. Milnes, T. Inoue, D. Marcuzzi, P. Sonato, and P. Zaccaria, "Status of the ITER heating neutral beam system," *Nucl. Fusion*, vol. 49, p. 15 pp, 2009.

[8] Y. Okumura, M. Fujiwara, and M. Kashiwagi, "Negative hydrogen ion source for TOKAMAK neutral beam injector," *Rev. Sci. Instrum.*, vol. 71, p. 1219, 2000.

[9] H. de Esch, "Electrons in singap." Private communication.

[10] J. Wesson, *Tokamaks*. Oxford University Press, 2004.

[11] E. Speth, "Neutral beam heating of fusion plasmas," *Reports on Progress in Physics*, vol. 52, p. 57, 1989.

[12] N. Duesing, H. Altmann, H. Falter, A. Goede, R. Haange, R. Hemsworth, P. Kupschus, D. Stork, and E. Thompson, "Neutral beam injection system," *Fusion Technology*, vol. 11, pp. 163–202, 1987.

[13] J. D. Lawson, "Some criteria for a power producing thermonuclear reactor," *Proceedings of the Physical Society. Section B*, vol. 70, p. 6, 1957.

[14] J. Wesson, "The science of JET," *Abingdon, Oxon, UK*, 2000.

[15] M. Shimada, D. Campbell, V. Mukhovatov, and et al., "Progress in the iter physics basis: Chapter 1: Overview and summary," *Nucl. Fusion*, vol. 47, no. 6, p. S1, 2007.

[16] N. Holtkamp, "The status of the ITER design," *Fusion Engineering and Design*, vol. 84, no. 2-6, pp. 98–105, 2009.

[17] I. Cook, N. Taylor, and D. Ward, "The role of DEMO in a Fast-Track development of fusion power," in *First Generation of Fusion Power Plants: Design and Technology*, IAEA, 2006.

[18] "IFMIF home page." `http://www.frascati.enea.it/ifmif/`.

[19] A. Staebler, P. Franzen, J. Hobirk, A. Peeters, A. C. C. Sips, and A. U. Team, "The role of neutral beam injection geometry in advanced discharge scenarios on ASDEX upgrade," in *Europhys. Conf. Abstr*, vol. 26, 2002.

[20] B. Streibl, P. T. Lang, F. Leuterer, J. M. Noterdaeme, and A. Stäbler, "Chapter 2: Machine design, fueling, and heating in asdex upgrade," *Fus. Sci. and Tech.*, vol. 44, no. 3, pp. 578–592, 2003.

[21] E. Speth, M. Ciric, J. H. Feist, P. Frank, B. Heinemann, W. Kraus, F. Probst, R. Riedl, R. Trainham, O. Vollmer, *et al.*, "Rf ion sources for fusion applications: design, development and performance," *Fusion Engineering and Design*, vol. 46, no. 2–4, pp. 383–388, 1999.

[22] D. Ciric, D. P. D. Brown, C. D. Challis, B. Chuilon, S. J. Cox, B. Crowley, I. E. Day, D. C. Edwards, G. Evison, L. J. Hackett, *et al.*, "Overview of the JET neutral beam enhancement project," *Fusion Engineering and Design*, vol. 82, no. 5–14, pp. 610–618, 2007.

[23] B. Crowley, E. Surrey, S. J. Cox, D. Ciric, and A. R. Ellingboe, "Experimental studies of the JET NBI neutraliser plasma," *Fusion Engineering and Design*, vol. 66, pp. 591–596, 2003.

[24] P. Franzen, J. Sielanko, H. de Esch, E. Speth, B. Heinemann, and R. Riedl, "In-line magnetic residual ion dump for the ITER neutral beam system," *Fusion Engineering and Design*, vol. 66, pp. 585–590, 2003.

[25] E. Surrey, A. Holmes, R. McAdams, and D. King, "Operation of the ITER electrostatic residual ion dump with a perturbed field," *Journal of Fusion Energy*, vol. 29, no. 5, pp. 486–498, 2010.

[26] IAEA, "ITER Technical Basis 2002 ITER EDA Documentation Series No.24 (Plant Description Document, Sec. 2.5.1)," tech. rep., International Atomic Energy Agency (AIEA), 2002.

[27] K. H. Berkner, R. Pyle, and J. Stearns, "Intense, mixed-energy hydrogen beams for ctr injection," *Nucl. Fus.*, vol. 15, no. 2, p. 249, 1975.

[28] J. Pamela, A. Bécoulet, D. Borba, J. L. Boutard, L. Horton, and D. Maisonnier, "Efficiency and availability driven R&D issues for DEMO," *Fusion Engineering and Design*, vol. 84, no. 2–6, pp. 194–204, 2009.

[29] ITER Technical Basis, "Neutral Beam Heating & Current Drive (NBH&CD) System ITER Design Description Document DDD 5.3," tech. rep., International Atomic Energy Agency, 2001.

[30] J. Pamela, "The physics of production, acceleration and neutralization of large negative ion beams," *Plasma Physics and Controlled Fusion*, vol. 37, p. A325, 1995.

[31] M. Bacal, E. Nicolopoulou, and H. Douset, "Studies of surface-plasma negative ion sources at novosibirsk," *Proc. Int. Symp. Production and Neutralization of negative ions and Beams*, vol. 26, 1977. New York.

[32] Y. I. Belchenko, G. E. Derevyankin, G. I. Dimov, and V. G. Dudnikov, "Studies of surface-plasma negative ion sources at novosibirsk," *Journal of Applied Mechanics and Technical Physics*, vol. 28, no. 4, pp. 568–576, 1987.

[33] K. N. Leung, G. J. DeVries, W. F. DiVergilio, R. W. Hamm, C. A. Hauck, W. B. Kunkel, D. S. McDonald, and M. D. Williams, "RF driven multicusp H^- ion source," *Review of Scientific Instruments*, vol. 62, no. 1, pp. 100–104, 1990.

[34] G. Rouleau, E. Geros, J. Stelzer, E. Chacon-Golcher, R. Keller, O. Tarvainen, and M. Borden, "Tungsten filament material and cesium dynamic equilibrium effects on a surface converter ion source," *Review of Scientific Instruments*, vol. 79, no. 2, p. 02A514, 2008.

[35] J. Peters, "The HERA RF-Driven multicusp h- ion source," in *11 th International Symposium on the Production and Neutralization of Negative Ions and Beams(AIP Conference Proceedings Volume 925)*, vol. 925, pp. 79–86, 2007.

[36] C. E. Hill, D. Küchler, C. Mastrostefano, M. Neil, R. Scrivens, and T. Steiner, "H^- source developments at CERN," *Review of Scientific Instruments*, vol. 77, no. 3, p. 03A521, 2006.

[37] M. Bacal, "Physics aspects of negative ion sources," *Nuclear Fusion*, vol. 46, p. S250, 2006.

[38] M. Allan and S. F. Wong, "Effect of vibrational and rotational excitation on dissociative attachment in hydrogen," *Phys. Rev. Lett.*, vol. 41, pp. 1791–1794, 1978.

[39] J. V. Laar and J. Schear *Philips Res. Rep.*, vol. 15, p. 1, 1960.

[40] B. J. Hopkins and J. C. Riviere, "The work function of polycrystalline tungsten foil," *Proceedings of the Physical Society*, vol. 81, p. 590, 1963.

[41] R. G. Wilson, "Electron and ion emission from polycrystalline surfaces of be, ti, cr, ni, cu, pt, and type-304 stainless steel in cesium vapor," *Journal of Applied Physics*, vol. 37, no. 8, pp. 3161–3169, 1966.

[42] R. G. Wilson, "Electron and ion emission from polycrystalline surfaces of nb, mo, ta, w, re, os, and ir in cesium vapor," *Journal of Applied Physics*, vol. 37, no. 11, 1966.

[43] L. W. Swanson and R. W. Strayer, "Field-Electron-Microscopy studies of cesium layers on various refractory metals: Work function change," *The Journal of Chemical Physics*, vol. 48, no. 6, pp. 2421–2442, 1968.

[44] D. E. Eastman, "Photoelectric work functions of transition, Rare-Earth, and noble metals," *Physical Review B*, vol. 2, no. 1, 1970.

[45] T. Inoue and et al., "Development of a Multi-Ampere H^- Ion Source at JAERI," in *Proceedings of the 6th International Symposium on Production and Neutralization of Negative Ions and Beams (Upton, New York)*, vol. 287, p. 316, 1992.

[46] E. Speth, H. D. Falter, P. Franzen, U. Fantz, M. Bandyopadhyay, S. Christ, A. Encheva, M. Fröschle, D. Holtum, B. Heinemann, *et al.*, "Overview of the RF source development programme at IPP garching," *Nuclear Fusion*, vol. 46, p. S220, 2006.

[47] R. Trainham and et al., "Long pulse operation of the kamaboko negative ion source on the mantis test bed," in *Production and Neutralization of Negative Ions and Beams, AIP, New York*, pp. 105–112, C. Jacquot ed., 1998.

[48] Y. Ohara, "Development of high power ion sources for fusion (invited)," *Review of Scientific Instruments*, vol. 69, p. 908, 1998.

[49] Y. Takeiri, O. Kaneko, K. Tsumori, Y. Oka, M. Osakabe, K. Ikeda, E. Asano, T. Kawamoto, and R. Akiyama, "Negative hydrogen ion source development for large helical device neutral beam injector (invited)," *Review of Scientific Instruments*, vol. 71, p. 1225, 2000.

[50] M. Kawai, L. Grisham, T. Itoh, M. Kazawa, M. Kuriyama, K. Mogaki, Y. Okumura, and K. Watanabe, "Study of plasma uniformity on JT-60U negative ion source," *Review of Scientific Instruments*, vol. 71, p. 755, 2000.

[51] P. McNeely, S. Dudin, S. Christ-Koch, and U. Fantz, "A langmuir probe system for high power RF-driven negative ion sources on high potential," *Plasma Sources Science and Technology*, vol. 18, p. 014011, 2009.

[52] A. Tanga, M. Bandyopadhyay, and P. McNeely, "Measurement of ion flow in a negative ion source using a mach probe," *Applied Physics Letters*, vol. 84, no. 2, p. 182, 2004.

[53] U. Fantz, H. Falter, P. Franzen, D. Wünderlich, M. Berger, A. Lorenz, W. Kraus, P. McNeely, R. Riedl, and E. Speth, "Spectroscopy — a powerful diagnostic tool in source development," *Nuclear Fusion*, vol. 46, p. S297, 2006.

[54] P. Franzen, "To be published."

[55] P. Franzen, H. Falter, U. Fantz, W. Kraus, M. Berger, S. Christ-Koch, M. Fröschle, R. Gutser, B. Heinemann, S. Hilbert, *et al.*, "Progress of the development of the IPP RF negative ion source for the ITER neutral beam system," *Nuclear fusion*, vol. 47, p. 264, 2007.

[56] P. Spaedtke and S. Wipf, "KOBRA3 — a code for the calculation of space charge influenced trajectories in 3 dimensions," *GSI Report*, vol. 89-09, 1989.

[57] W. Kraus, H. Falter, U. Fantz, P. Franzen, B. Heinemann, P. McNeely, R. Riedl, and E. Speth, "Long pulse large area beam extraction with a RF driven H^-/D^- source," *Review of Scientific Instruments*, vol. 79, no. 2, p. 02C108, 2008.

[58] P. Franzen, H. Falter, B. Heinemann, C. Martens, U. Fantz, M. Berger, S. Christ-Koch, M. Fröschle, D. Holtum, W. Kraus, *et al.*, "RADI an RF source size-scaling experiment towards the ITER neutral beam negative ion source," *Fusion Engineering and Design*, vol. 82, no. 4, pp. 407–423, 2007.

[59] R. S. Hemsworth, A. Tanga, and V. Antoni, "Status of the ITER neutral beam injection system (invited)," *Review of Scientific Instruments*, vol. 79, no. 2, p. 02C109, 2008.

[60] D. Marcuzzi, P. Agostinetti, M. Dalla Palma, F. Degli Agostini, M. Pavei, A. Rizzolo, M. Tollin, and L. Trevisan, "Detail design of the beam source for the SPIDER experiment," *Fusion Engineering and Design*, 2010.

[61] P.Sonato, T. Bonicelli, and R. S. Hemsworth, "The neutral beam test facility in padova: The necessary step to develop the neutral beam injectors for iter," *To be published*, 2010.

[62] M. Taniguchi, T. Inoue, M. Kashiwagi, K. Watanabe, M. Hanada, T. Seki, M. Dairaku, and K. Sakamoto, "Acceleration of MeV-class energy, high-current-density H^--ion beams for ITER neutral beam system," *Review of Scientific Instruments*, vol. 77, no. 3, p. 03A514, 2006.

[63] ITER Technical Basis, "DDD5.3," tech. rep., International Atomic Energy Agency, 2001.

[64] R. Gutser, "Rechnungen zur extraktion negativer wasserstoffionen aus einem HF-plasma," Master's thesis, Universität Augsburg, 2006.

[65] A. Staebler, U. Fantz, P. Franzen, M. Berger, S. Christ-Koch, H. D. Falter, M. Froeschle, R. Gutser, B. Heinemann, D. Holtum, *et al.*, "Development of a RF-driven ion source for the ITER NBI system," *Fusion Engineering and Design*, vol. 84, no. 2–6, pp. 265–268, 2009.

[66] U. Fantz, "Physical performance analysis and progress of the development of the negative ion rf source for the ITER NBI system," *Nucl. Fusion*, vol. 49, p. 125007 (9pp), 2009.

[67] R. Nocentini, R. Gutser, B. Heinemann, M. Froeschle, and R. Riedl, "Plasma grid design for optimized filter field configuration for the NBI test facility ELISE," *Fusion Engineering and Design*, vol. 84, no. 12, pp. 2131–2135, 2009.

[68] B. Heinemann, H. Falter, U. Fantz, P. Franzen, M. Fröschle, R. Gutser, W. Kraus, R. Nocentini, R. Riedl, E. Speth, A. Stäbler, D. Wünderlich, P. Agostinetti, and T. Jiang, "Design of the "half-size" ITER neutral beam

source for the test facility ELISE," *Fusion Eng. Des.*, vol. 84, pp. 915–922, 2009.

[69] *ANSYS Manual, ANSYS Ltd.*, 2009.

[70] R. Gutser. Private communication.

[71] R. Kreutz, "Auslegung von wassergekühlten kalorimeterplatten für neutralinjektion mit langen pulsen," *DATF/KTG Jahrestagung Kerntechnik*, vol. 84, pp. 769–776, 1985.

[72] M. Wadel, "Comparison of high aspect ratio cooling channel designs for a rocket combustion chamber with development of an optimized design," tech. rep., NASA/TM-1998-206313, 1998.

[73] *ANSYS CFX Manual, ANSYS Ltd.*, 2006.

[74] *ANSYS CFX-Solver Theory Guide, ANSYS Ltd.*, 2006.

[75] F. Gunther, "Photographic study of surface boiling heat transfer to water with forced convection," *Trans. Am. Soc. Mech. Eng.*, vol. 73, pp. 115–123, 1951.

[76] L. Leifsson, A. Ko, A. Schetz, W. Mason, , B. Grossman, and R. Haftka, "Multidisciplinary design optimization of a blended-wing-body transport aircraft with distributed propulsion," *AIAA 3rd Annual Aviation Technology, Integration, and Operations (ATIO) Technical Forum, Denver, CO*, 2003.

[77] N. Cristello and I. Y. Kim, "Design optimization of an automotive universal joint considering manufacturing cost," in *Proceedings of the 17th IASTED international conference on Modelling and simulation*, p. 499–504, 2006.

[78] Y. Yang, C. Park, K. Lee, and J. Suh, "A study on the preliminary ship design method using deterministic approach and probabilistic approach including hull form," *Structural and Multidisciplinary Optimization*, vol. 33, no. 6, pp. 529–539, 2006.

[79] M. Huber, O. Petersson, and H. Baier, "Lecture manuscript of multidisciplinary design optimization." University Lecture, 2007.

[80] P. Y. Papalambros and D. J. Wilde, *Principles of Optimal Design: Modeling and Computation.* Cambridge, UK: Cambridge University Press, 2000.

[81] O. C. Zienkiewicz and R. L. Taylor, *The Finite Element Method.* Butterworth-Heinemann, London, UK, 2005.

[82] V. Pareto, *Manuale di Economia Politica*. Societa Editrice Libraria, Milano, Italy, 1906. Empirical Model Building and Response Surfaces.

[83] *MATLAB Optimization Toolbox 2007, The Mathworks, Natick, MA, USA*.

[84] R. H. Myers and D. C. Montgomery, *Response Surface Methodology: Process and Product Optimization Using Designed Experiments*. JohnWiley & Sons, New York, NY, USA, 2nd edition ed., 2002.

[85] G. E. P. Box and N. R. Draper, *Empirical Model Building and Response Surfaces*. JohnWiley & Sons, New York, NY, USA, 1987.

[86] D. C. Montgomery, E. A. Peck, and G. G. Vining, *Introduction to Linear Regression Analysis*. JohnWiley & Sons, New York, NY, USA, 3rd edition ed., 2001.

[87] T. J. Santner, B. J. Williams, and W. I. Notz, *The Design and Analysis of Computer Experiments*. Springer Series in Statistics. Springer-Verlag, New York, NY, USA, 2003.

[88] MATLAB, *Statistics Toolbox 2007*. The Mathworks, Natick, MA, USA, 2007.

[89] *MATLAB user guide 2007, The Mathworks, Natick, MA, USA*.

[90] H.-D. Falter. Private communication.

[91] D. Wünderlich, R. Gutser, and U. Fantz, "Pic code for the plasma sheath in large caesiated negative hydrogen ion sources," *Plasma Sources Science and Technology*, vol. 18, p. 045031, 2009.

[92] P. Agostinetti, S. Dal Bello, M. Dalla Palma, B. Heinemann, R. Nocentini, C. Zauner, H. Langer, and J. Klammer, "Investigation of the thermo-mechanical properties of electro-deposited copper for iter," *Journal of Nuclear Materials*, vol. 417, pp. 924–927, 2011.

[93] *KOBRA3-INP User Manual*.

Appendix A

Material tests on Copper

The properties of electro-deposited pure copper are considered as a crucial aspect for the design of the grids for negative-ion sources like ELISE. These devices feature components subjected to cyclic heat loads with high power densities (in the range of 30 MW/m^2) and operation at high temperature with high pressure inside mater manifold embedded in the grids. Reliable thermo-mechanical properties of galvanic copper are required, in order to carry out precise mechanical simulations during the design phase. Data obtained during a comprehensive test campaign [92], planned and carried out by KRP-Mechatec in collaboration with IPP Garching, Consorzio RFX, Padua, and Galvano-T electroforming plating GmbH, have been used for the FE calculations. During the campaign the main mechanical properties (Young modulus, yield strength, ultimate strength, elongation, reduction of area and fatigue life) and the main thermal properties (specific heat, thermal conductivity and thermal expansion) have been evaluated. The dependence of the most important parameters with respect to temperature have been determined, as shown in figure A.1 and A.1.

Mechanical properties of electro-deposited copper are sensibly better than the ones of pure annealed copper. These advantages could be due to the very small grain size obtained with the electro-deposition.
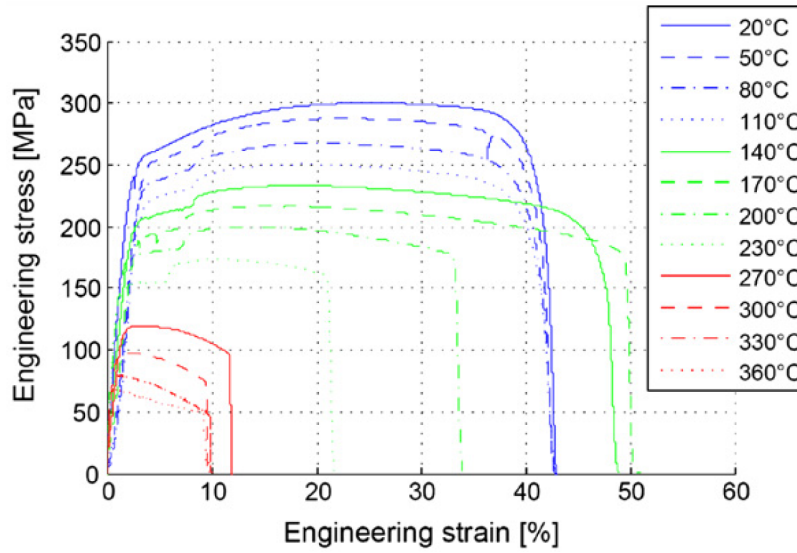
Figure A.1: Tensile test results: engineering stress-strain curves.
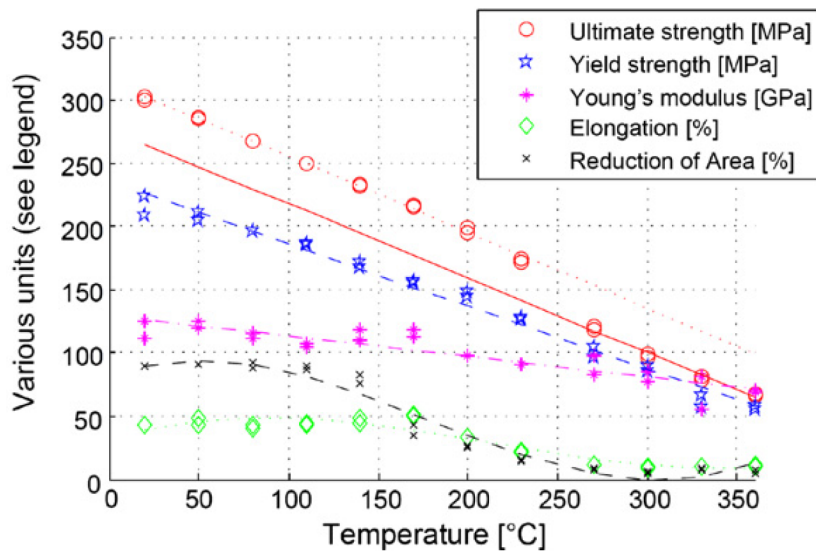
Figure A.2: Tensile test results: tensile properties in function of test temperature.

Appendix B

Magnetic materials

To model the permanent magnets the B-H curve of Vacomax 225 HR, shown in figure B.1 and B.2 has been used as input for the ANSYS code.
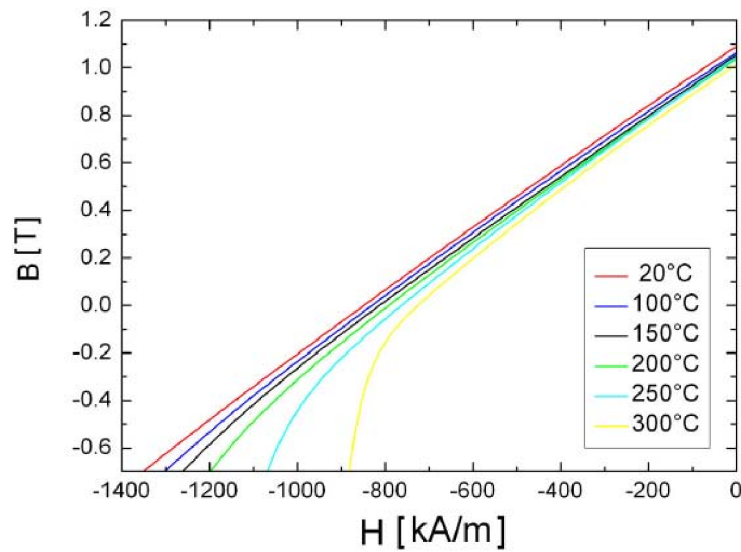
Figure B.1: Dependence of Magnetic flux density B on the applied field strength H at several temperatures for permanent magnets Vacomax HR.
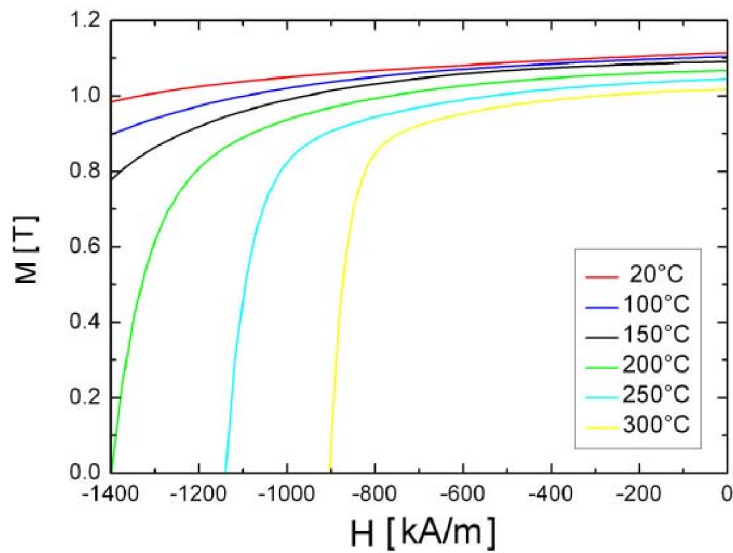
Figure B.2: Dependence of magnetization on the applied field strength H at several temperatures for permanent magnets Vacomax HR.

Appendix C

Ion and electron beam calculations

To determine the power load on the EG surface it is necessary to calculate the electron trajectories, for a given extracted electron and ion current. The electron trajectories are influenced by the magnetic field generated by permanent magnets, electric field between the electrodes and space charge distribution represented by the extracted negative ion beam. FEM codes capable to model the complex 3 dimensional geometry of electrodes and magnetic fields are adopted. Self-consistent particle simulations, which consider the interaction between many particles through an iterative process, are used for the ion and electron trajectories.

Particle simulation codes The simplest class of particle simulations is the **Single Particle Description**. In this codes particles are considered as individual electrons or ions moving in imposed (rather than self-consistent, see below) electric and magnetic fields. The motion of each particle is described by the Lorentz Force Law, without considering the interaction between many particles. Collision process as well as chemical reactions can be considered by means of empirical parameters.

To consider the interaction between many particles more complex codes are necessary. In particular for the calculation of the Lorentz Force considering the particle-particle interaction, it is necessary to know the instantaneous position of all the particles. In this case, a **Particle-in-Cell** (PIC) algorithm is used. In this case for every time-step a new calculation of the particle positions, and of the resulting electric field, is carried out. PIC codes have a very general applicability and allow also time-dependent analyzes, but require large amounts of memory and computing time.

The most commonly used method for the calculation of ion optics is the **Ray Tracing** (RT). This represents a simplification of the PIC code in case of stationary phenomena. While in PIC codes an iteration step contains the calculation of the movement of each particle and the computation of the resulting new electric field, in the RT method the complete trajectory of all the particles are calculated. The

calculation of the electric field is carried out after all the complete trajectories are determined for one iteration step. The space charge distribution is calculated on the basis of the positions and velocity of the particles. The interaction between the particles determined by the space charge distribution is considered because in every iteration step the particle trajectories are calculated on the basis of the space charge distribution from the previous iteration step. When the change in space charge distribution between two successive steps is smaller than a convergence criteria the solution is defined self-consistent.

Ray Tracing Code KOBRA3 Within the context of this work the KOBRA3 code [93] is used. This code is characterized by the fact that is entirely 3-dimensional. In addition a module for the self-consistent computation of the plasma boundary layer, adjusted to consider extraction of negative ions, is included in the program.

ETRON The ETRON code is a ray tracing code to determine the heat load caused by fast electrons which solves the ordinary differential equation from the relativistic Lorentz equation using the extrapolation method. While the magnetic field maps are given by any FEM magnetic field solver such as ANSYS, the electric field and the corresponding space charge distribution from a beam code such as KOBRA3 or SLAC is used. A Monte Carlo algorithm with normal distributed spatial coordination is used to sample the distribution of the particle coordinates on an arbitrary surface deducing the power distribution of the heat load.

Appendix D

Nomenclature

Symbols

Symbol	Description	Unit
A	Attainable set	
A	Atomic mass	amu
B	Magnetic flux density	T
E	Energy	J
H	Hydrogen	
D, D	Deuterium, design space	
D_f	Feasible design space	
T	Tritium	
f, $\mathbf{f}$	Objective function, objective function vector	
g, $\mathbf{g}$	Inequality constraint function, inequality constraint function vector	
h, $\mathbf{h}$	Equality constraint function, equality constraint function vector	
j	Current density	A/m^2
$\mathbf{lb}$, $\mathbf{ub}$	Vectors with lower and upper bounds for the design variables	

Symbol	Description	Unit
m	Mass	kg
n	Density	m^{-3}
n	Neutron	
p	Proton	
p	Pressure	Pa
P	Power	W
Q	Gain factor	
r	Radius	m
T	Temperature	K, °C, eV
U	Voltage	V
v	Velocity	m/s
z, $\mathbf{z}$	Objective function value, objective function value vector	
α	Alpha particles, helium nuclei	
β, $\boldsymbol{\beta}$	Regression coefficient, regression coefficient vector	
ε	Error term	
λ	Mean free path	m
$\nu"$	Vibrational excitation	
σ	Cross section, normal stress, standard deviation (see context)	m^2, Pa
τ	Time, shear stress (see context)	s, Pa
ω	Frequency	Hz

Constants

Symbol	Description	Value	Unit
c	velocity of light	$2.998 \cdot 10^8$	m/s
e	elementary charge	$1.602 \cdot 10^{-19}$	A·s
π		3.141593	

Indexes

Symbol	Description
x	scalar value
$\mathbf{x}$	vector
$\mathbf{X}$	matrix
$()^T$	matrix transpose
$\langle \rangle$	mean value
e	electron

Abbreviations

Acronym	Description
CFD	Computational Fluid Dynamics
DOE	Design Of Experiments
EDF	Electron Deflection Field
ESM	Electron Suppression Magnets
EG	Extraction Grid
FE	Finite Elements
FEM	Finite Element Method

Acronym	Description
FEA	Finite Element Analysis
FF	Filter Field
GG	Grounded Grid
HTC	Heat Transfer Coefficient
IPP	Max-Planck Institut für Plasmaphysik
N-NBI	Negative ion Neutral Beam Injection
PG	Plasma Grid
RF-driven	Radio Frequency driven
RSA	Response Surface Approximation
RSM	Response Surface Model
SST	Shear Stress Transport

Acknowledgments

I would like to express my gratitude to my supervisor, Univ.-Prof. Dr.-Ing. Horst Baier, whose guidance and support made this work possible. I also would like to thank Prof. Dr.-Ing., Dr. Eng. (Japan) Hans-Harald Bolt for his interest in my work and for accepting to be the second supervisor.

I especially thank Bernd Heinemann, whose expertise, encouragement, and patience, supported me during my PhD and not only.

I am very grateful to everybody who has contributed to my PhD:

- Rudolf Riedl and Markus Fröschle for the long conversations on the various topics of this work and for their valuable suggestions.

- Dr. Raphael Gutser for his collaboration and support and for performing the KOBRA3 and Etron calculations.

- Ögmundur Petersson, Dr. Christoph Zauner and Dr. Harald Langer for their assistance in ANSYS, MATLAB and MDO related questions.

- Prof. Dr.-Ing. Ursel Fantz, Dr. Peter Franzen, Dr. Christian Hopf and Dr. Dirk Wünderlich for their advice and support on the physics of negative-ion sources and nuclear fusion.

- The complete NNBI-Team for the support and the pleasant working atmosphere.

Most of all, I would like to thank my girlfriend Tika who supported me everyday in the last three years to complete my PhD.

Munich, March 2011   Riccardo Nocentini